Ice discharge estimation of the Jakobshavn glacier (Greenland) from 2010 until 2016 using satellite altimetry and satellite gravimetry in combination with RACMO

L. Keuris

Master thesis

TU Delft: Geoscience & Remote Sensing
TU Delft: Applied Geophysics (IDEA League)

TU Delft

Ice discharge estimation of the Jakobshavn glacier (Greenland) from 2010 until 2016 using satellite altimetry and satellite gravimetry in combination with RACMO

by

L. Keuris

to obtain the degree of Master of Science
at the Delft University of Technology,
to be defended publicly on Wednesday November 28, 2018 at 15:45.

Student number:	4212924	
Project duration:	December, 2017 – November, 2018	
Thesis committee:	Dr. ir. C. Slobbe,	Delft University of Technology, supervisor, chair
	Dr. ir. B. Wouters,	Delft University of Technology, Utrecht University, supervisor
	Dr. P. Ditmar,	Delft University of Technology, supervisor
	Dr. ir. G. Drijkoningen,	Delft University of Technology

This thesis is public.

An electronic version of this thesis is available at `https://repository.tudelft.nl/`.

TU Delft

Cover image: ESA, *Artist's impression of CryoSat in orbit*;

https://www.esa.int/spaceinimages/Images/2005/07/CryoSat12

Header image chapter 1: NASA Goddard Space Flight Center, *Jakobshavn Calving Front*;

https://www.flickr.com/photos/gsfc/7166014512/

Header image chapter 2: ESA/AOES, *CryoSat, Artist's impression of CryoSat in orbit*;

http://blogs.esa.int/cryosat-ice-blog/cryosat/

Header image chapter 3: NASA/JPL-Caltech, *Artist's concept of Gravity Recovery and Climate Experiment*;

https://www.nasa.gov/mission_pages/Grace/multimedia/pia04236.html#.W707Zmj7SUl

Header image chapter 4: Utrecht University (IMAU), *Institute for Marine and Atmospheric Research (IMAU) Ice and Climate header image*;

https://www.projects.science.uu.nl/iceclimate/publications/publications.php

Abstract

The Jakobshavn glacier was responsible for approximately 1 mm eustatic sea level rise in the period of 2000 to 2010 [Howat et al., 2011]. As such, the Jakobshavn glacier became one of the largest outlet glaciers in Greenland [Joughin et al., 2004]. Ice flow velocities within the same period reached over 10 km/yr with strong seasonal variation [Howat et al., 2011, Joughin et al., 2012]. More recently from 2011 until 2013, even higher ice flow velocities of at least 15 km/yr were observed [Lemos et al., 2018]. Due to the relatively high ice flow velocities, the ice discharge plays the largest role in the mass balance (MB) of the Jakobshavn glacier. Quantification of the ice discharge from ice flow velocities is however, not a common procedure. Yet the evolution of the ice discharge of single glaciers not only improves understanding of the climate-cryosphere system, but also aids quantification of sea level contribution on a drainage basin scale. To that end, this study embodies an indirect ice discharge estimation of the Jakobshavn glacier over the period of November 2010 until March 2016 using altimetry (CryoSat-2 Level 1b (L1b)) and gravimetry (GRACE Level 2 (L2)) data in combination with a regional climate model (RACMO 2.3p2). By subtraction of the altimetric and gravimetric mass balance estimates from the atmospheric component (i.e. the surface mass balance (SMB)), two ice discharge estimates are obtained. This approach does not suffer from the drawbacks involved when estimating ice discharge from velocity fields directly, which are based on offset tracking. Data gaps for long polar nights and clouds in the visible spectrum and decorrelation in general, when the duration between subsequent images over the same location is long, are thus avoided. This is because offset tracking algorithms require recognisable characteristics in subsequent satellite recordings to determine the velocity, i.e. satellite recordings need to be sufficiently correlated. To derive the mass balance from altimetry data, adequate spatial sampling is desired. To that end, this study applies swath processing to CryoSat-2 L1b data with an adapted waveform sample selection criterion to obtain an unprecedented spatial sampling with about 2 order of magnitude more height observations compared to conventional retracking techniques. As a consequence, elevation changes can be derived at a relatively high spatial resolution (250 m). The elevations are converted to elevation changes, volume change and mass change using weighted least squares estimations (WLSE), hypsometric averaging and density models, respectively. The GRACE-based mass change estimate is acquired using a point-mass assumption at the location of the Jakobshavn glacier. The known, simulated point mass is then scaled to the observed mass by GRACE. In addition, data weighting of GRACE Stokes' coefficients is attempted using the full noise covariance matrix. Subsequently, a LSE is used to infer the mass balance from the two time series (with and without weighting of the Stokes' coefficients).

Samenvatting

De Jakobshavn gletsjer was verantwoordelijk voor ongeveer 1 mm wereldwijde zeeniveaustijging gedurende de periode van 2000 tot en met 2010 [Howat et al., 2011] en werd daarmee één van de grootste afvoergletsjers van Groenland [Joughin et al., 2004]. IJsstroomsnelheden tijdens diezelfde periode bereikte minstens 10 km/jaar met sterke seizoensvariaties [Howat et al., 2011, Joughin et al., 2012]. Na deze periode, tussen 2011 en 2013, werden nog hogere ijsstroomsnelheden (>15 km/jaar) waargenomen [Lemos et al., 2018]. Door de relatief hoge ijsstroomsnelheden speelt de ijsafvoer de grootste rol in de massabalans van het Jakobshavn stroomgebied. Desondanks wordt de ijsafvoer vaak niet gequantificeerd. Het onderzoek naar ijsafvoer van gletsjers is echter van belang voor het beter begrijpen van zowel de wisselwerking tussen het klimaat en de poolkappen als de uiteindelijke invloed op zeeniveaustijging op gletsjerschaal. Deze studie is daarom gericht op het indirect schatten van de ijsafvoer van de Jakobshavn gletsjer vanaf november 2010 tot en met maart 2016. Dit wordt gedaan met behulp van altimetrie- (CryoSat-2 Level 1b (L1b)) en gravimetriedata (GRACE Level (L2)) in combinatie met een regionaal klimaatmodel (RACMO 2.3p2). Door de totale massabalans af te halen van de atmosferische component (SMB) wordt de ijsafvoer bepaald. Hiertoe worden twee massabalansen berekend, één met altimetrieobservaties en één met gravimetrieobservaties. Deze aanpak ondervindt niet de nadelen die voorkomen bij het bepalen van de ijsafvoer aan de hand van ijsstroomsnelheden. IJsstroomsnelheden worden namelijk voornamelijk berekend met offset tracking. Een nadeel van deze methode is de ontbrekende data door wolken en het lang ontbreken van zonlicht in de winter bij de toepassing in het zichtbare spectrum. Daarnaast verhindert ook decorrelatie, wanneer de duur tussen twee satellietobservaties over hetzelfde gebied lang is, de schatting van ijsstroomsnelheden. Offset tracking algoritmes moeten namelijk karakteristieken elementen kunnen herkennen in opeenvolgende sattelietopnames om de snelheid te kunnen bepalen (oftewel de opnames moeten voldoende gecorreleerd zijn). Om de massabalans te bepalen aan de hand van altimetrieobservaties is adequate spatiële dekking van observaties een belangrijk element. In deze studie wordt swath processing toegepast op CryoSat-2 L1b data. Samen met een aangepast criterium voor het selecteren van punten binnen een golfvorm kan met swath processing tot 3 ordes meer hoogtemetingen worden gedaan in vergelijking tot conventionele selectietechnieken. Als gevolg daarvan kunnen ook hoogteveranderingen op relatief hoge resolutie (250 m) worden bepaald. De hoogtemetingen worden omgezet naar hoogteveranderingen, volumeverandering en massaverandering met behulp van, respectievelijk, een gewogen kleinste kwadratenmethode (WLSE), hypsometrisch middelen en verschillende dichtheidsmodellen. De massaveranderingsschatting gebaseerd op GRACE L2 observaties wordt verkregen door een puntmassa aan te nemen op de locatie van de Jakobshavn gletsjer. De bekende, gesimuleerde puntmassa wordt dan geschaald naar de door GRACE geobserveerde massa. Daarbij wordt ook een schatting gemaakt mèt weging van de GRACE Stokes' coefficiënten met de variantie-covariantiematrix. Vervolgens kan de kleinste kwadratenmethode worden toegepast op de twee tijdsreeksen (met en zonder weging van de GRACE Stokes' coefficienten) om de massabalans te bepalen.

Acknowledgements

This thesis marks the end of my MSc. tracks in Applied Geophysics and in Geoscience and Remote Sensing. Throughout my time at the ETH Zürich and TU Delft, I have had the chance to study the ins and outs of the Earth, literally. The scientific understanding of the Earth's system has grown enormously in the past century. Especially since the dawn of continuous satellite observations, we have become more and more aware of the chain of coupled processes that affect today's Earth. Our contribution to the Earth's system appears ever-growing, which is why studies within this field are crucial.
In the past year I have primarily dedicated my time to prepare this final report. During that time, I received distinguished guidance from Pavel Ditmar, Cornelis Slobbe and Bert Wouters. Therefore, I wish to express my gratitude towards each of them for sharing their valuable time and knowledge with me. This has allowed me to substantially improve my understanding on the matters that are discussed throughout this thesis and as such, to improve this thesis significantly. Furthermore, I wish to thank Guy Drijkoningen for helping me realise the combination of these master tracks. Also, I express my gratitude towards Torsten Mayer-Gürr of the Institute of Geodesy from TU Graz for providing GRACE L2 monthly solutions and normal matrices as well as Brice Noël of the Institute for Marine and Atmospheric Research (IMAU) from Utrecht University for sharing RACMO 2.3p2. Last but not least, I wish to thank Michalea King of the Ohio State University for providing the ice discharge time series of the Jakobshavn glacier for validation.

List of Acronyms

Abbreviation	
ATM	Airborne Topographic Mapper
DEM	Digital Elevation Model
DLR	Deutsches Zentrum für Luft- und Raumfahrt (German Aerospace Center)
DoN	Distance off Nadir
DORIS	Doppler Orbitography and Radiopositioning Integrated by Satellite
ELA	Equilibrium Line Altitude
ESA	European Space Agency
EWH	Equivalent Water Height
FDM	Firn Densification Model
GIA	Glacial Isostatic Adjustment
GIMP	Greenland Ice sheet Mapping Project
GRACE	Gravity Recovery and Climate Experiment
GrIS	Greenland Ice Sheet
ICESat	Ice, Cloud, and land Elevation Satellite
IMAU	Institute for Marine and Atmospheric Research Utrecht
IRA	Interferometric Radar Altimeter
KNMI	Koninklijk Nederlands Meteorologisch Instituut (Dutch Royal Meteorological Institute)
Laser	Light Amplification by Stimulated Emission of Radiation
LEO	Low-Earth Orbit
LiDAR	Light Detection and Ranging
LRM	Low Resolution Mode
L1/L1b/L2	Processing levels 1, 1b and 2
MB	Mass Balance
NASA	National Aeronautics and Space Administration
NSIDC	National Snow and Ice Data Center
OIB	Operation IceBridge
RACMO	Regional Atmospheric Climate Model
Radar	Radio Detection and Ranging
(R)CM	(Regional) Climate Model
SAR	Synthetic Aperture Radar
SIN(m)	Synthetic Aperture Radar Interferometric (mode)
SIRAL	SAR/Interferometric Radar Altimeter
SMB	Surface Mass Balance
SNR	Signal to Noise Ratio
WGS84	World Geodetic System 1984
(W)LSE	(Weighted) Least Squares Estimation

Contents

List of Figures

List of Tables

1 Introduction

1.1. Background

This research focuses on the Jakobshavn glacier at the West coast of Greenland (69.2°, -49.7°). The Jakobshavn glacier drains ice, snow and water from the vast Greenland ice sheet (GrIS). The area from which the Jakobshavn glacier drains is referred to as the Jakobshavn drainage basin, which is outlined in red in figure 1.1.

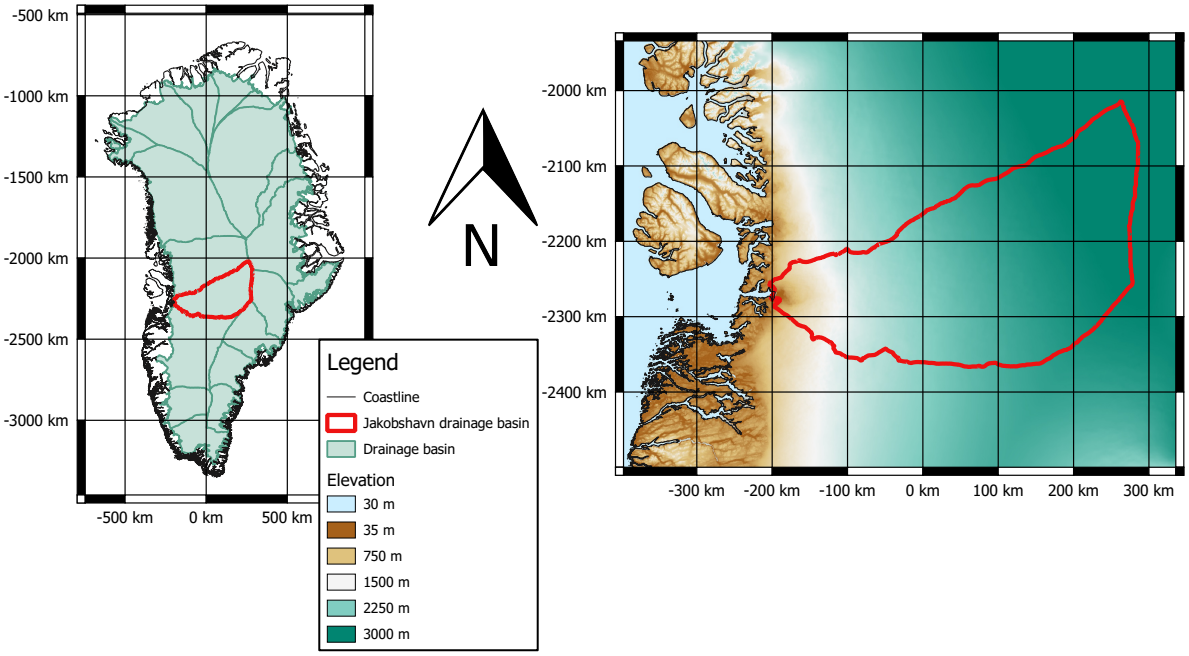

Figure 1.1: Greenland and its division by drainage basins on the left. The Jakobshavn drainage basin on the right with an underlying digital elevation model (DEM). Elevation is with respect to the reference ellipsoid (WGS84). *Drainage basin division is taken from Zwally et al. [2012]. DEM is taken from Howat et al. [2017].*

The Jakobshavn glacier itself acquired a lot of interest from the scientific community in the past decade. Although the glacier width is relatively small (approx. 5 km) compared to e.g. Zachariae Isstrøm (approx. 26 km), the Jakobshavn glacier is considered Greenlands largest outlet glacier [Joughin et al., 2004]. It discharges about 6.5% of Greenlands total ice discharge [Joughin et al., 2004].
The Jakobshavn glacier has not always drained such a large amount ice, snow and water. The Jakobshavn glacier is considered to have been relatively stable between 1964 and 1989 [Pelto et al., 1989]. A period of thickening followed, after which rapid thinning was observed when the ice floating tongue started to disintegrate in the late 1990's [Joughin et al., 2004]. This was likely caused by the retreat of the calving front and thinning of the shelf [Muresan et al., 2016]. Ice flow velocities dropped from 6.7 km/yr in 1985 to 5.7 km/yr in 1992, accelerating in 1999 to 9.4 km/yr in 2000 and 12.6 km/yr in 2003 [Joughin et al., 2004]. The mass loss of the Jakobshavn glacier was 8 Gt/yr in 2000, increasing up to about 25 Gt/yr by the end of 2002 [Howat et al., 2011]. With the loss of the glacier tongue in late 2003 [Muresan et al., 2016], the glacier's flow velocity and terminus advancement shows stronger seasonal variation [Howat et al., 2011, Joughin et al., 2012]. Mass loss accelerated in 2006, rising up to 33 Gt/yr by 2007 [Howat et al., 2011]. Until the end of 2010, the loss fluctuated between between 25 and 33 Gt/yr [Howat et al., 2011]. Strong ice flow acceleration was observed again in the period of 2011 to 2013, reaching flow velocities over 15 km/yr [Lemos et al., 2018]. The calving front retreat has been visualised in figure 1.2 using images from Terra and LandSat.

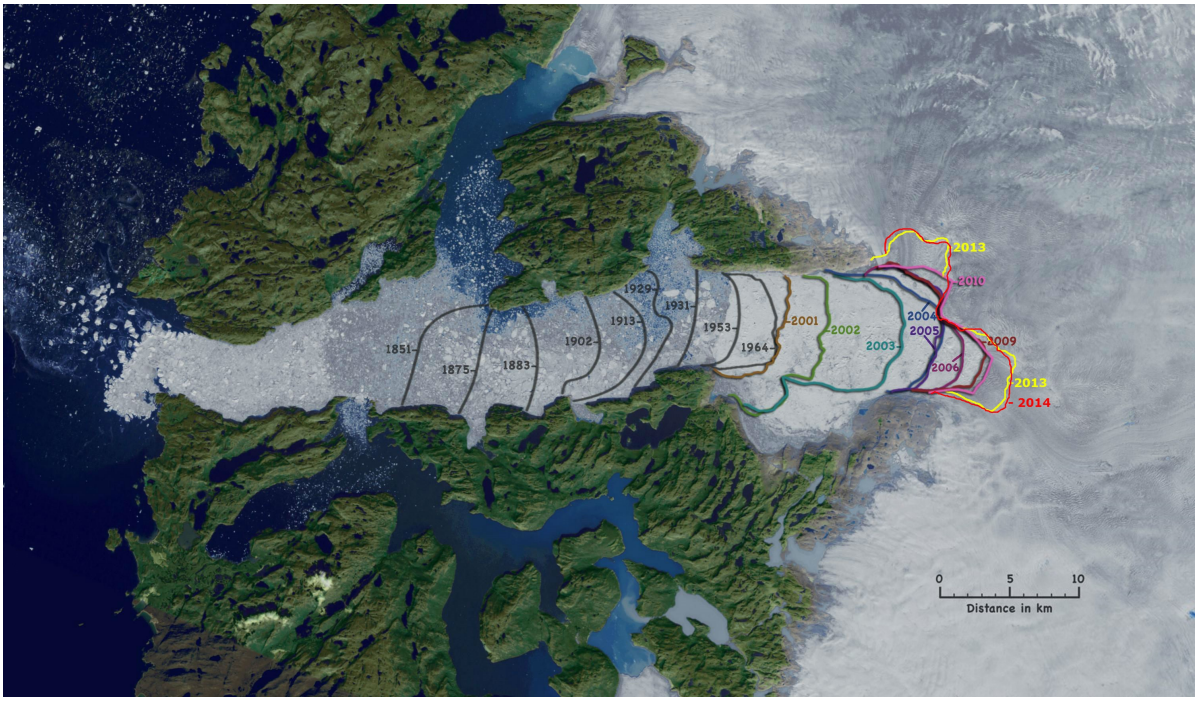

Figure 1.2: Calving front of the Jakobshavn glacier with dated demarcations. *Taken from:* `https://svs.gsfc.nasa.gov/3806`. *Updated for the years 2013 and 2014 by E. Olsen.*

Simultaneously, since 1997, the ice shelf is thinning [Hurkmans et al., 2012]. A thinner ice shelf, along with melt water seepage through cracks and between the bedrock and the ice sheet (friction reduction), leads to higher ice flow velocities. As a consequence, the Jakobshavn glacier is considered a significant contributor to sea level rise from the Arctic cryosphere. Concretely, the contribution to eustatic sea level rise from the Jakobshavn glacier from 2000 to 2011 was nearly 1 mm [Howat et al., 2011]. That loss resembles a basin-wide thinning of 3.5 m [Howat et al., 2011]. For a detailed historical study on the glacier terminus and surface elevations of the Jakobshavn glacier in the 20^{th} century, we refer to Csatho et al. [2008].
The Jakobshavn mass loss that has taken place throughout this century is driven by two components:

$$MB = SMB - ID, \tag{1.1}$$

where MB represents the (total) mass balance, the SMB is the surface mass balance, i.e. the atmospheric component and ID the ice discharge, i.e. the dynamic component. A negative or positive MB indicate ablation or accumulation, respectively. A MB for a glacier is commonly given on a yearly basis in Gt/yr. Concretely,

approximately 332 Gt of ice loss exhibits 1 mm eustatic sea level rise.
MB estimations can be obtained using observations from various remote sensing techniques. *Spaceborne* gravimetry (e.g. GRACE twin satellites), a remote sensing technique can provide such observations. Likewise for LiDAR (e.g. ICESat) and radar (e.g. CryoSat-2), which are both active spaceborne remote sensing techniques. *Airborne* remote sensing techniques also exist, but generally lack the combination of adequate temporal and spatial sampling.
With gravimetry, mass change or rather redistribution can be observed. LiDAR and radar observe elevation, which can be related to volume change. In the latter case conversion to mass is required.
The Regional Atmospheric Climate Model (RACMO) has been designed to model the SMB of polar regions, i.e. Antarctica and Greenland [IMAU]. The SMB represents the net sum of accumulation from snow and rain and ablation by run-off and sublimation.
The ice discharge can be obtained by integrating flow velocities over the *flux gate* assuming the density of ice. The flux gate is a plane perpendicular to the flow direction near the terminus (upstream the grounding line). Flow velocities are generally derived from radar or visible satellite imagery with tracking algorithms [Joughin et al., 2004, Lemos et al., 2018, Strozzi et al., 2002].

1.2. Previous work

The sensitivity of ice dynamics (discharge) to climate change is not fully understood [Howat et al., 2007]. As a consequence, the description corresponding physical processes that are included in ice-sheet models are inadequate [Howat et al., 2007]. The ice discharge of the Jakobshavn glacier has been studied by Howat et al. [2011] in the period of 2000 until 2010 (see section 1.1). Velocity fields are good indicators of ice dynamics. Velocity fields of the Jakobshavn glacier have been made by Joughin et al. [2010], Moon et al. [2014], Pelto et al. [1989]. Quantification of the ice discharge from ice flow velocities is however, not a common procedure. More often, the ice flow velocities are used to improve understanding of glacier physics [Moon et al., 2014]. In some cases research only focused on thinning rates [Foresta et al., 2018, Nilsson et al., 2016, Wang and Holland, 2018]. In others, volume estimates are obtained [Hurkmans et al., 2012, Motyka et al., 2010, Nielsen et al., 2013], omitting conversion of volumes to mass. The scales of observation area among these studies varies widely, i.e. from a few 1000 km^2 near the Jakobshavn terminus up to entire Greenland. The ice discharge of the Jakobshavn glacier can be attributed to a demarcated basin described by Zwally et al. [2012]. This demarcation is also used in this study (see figure 1.1). Most recently, King et al. [2018] (in review) integrated for each outlet glacier, its thickness, flow velocity and ice density across the flux gate from 2000 until 2016. The average ice discharge of the time series of the Jakobshavn glacier over the period of November 2010 until March 2016 (observation period of this study) was estimated at 50.8±2.2 Gt/yr.

1.3. Motivation

The goal is to infer the ice discharge of the Jakobshavn glacier. As indicated in section 1.1, the ice discharge of the Jakobshavn glacier contributes to a relatively large amount of the total ice discharge of Greenland. In the context of sea level rise, ice discharge of glaciers is of importance. The Jakobshavn glacier alone connects roughly 95380 km^2 of ice sheet surface area to the ocean. The ice discharge is the greater net mass change component compared to the SMB. The evolution of the ice discharge of single glaciers not only improves understanding of the climate-cryosphere system, but also aids quantification of sea level contribution on a drainage basin scale. To that end, this project embodies an ice discharge estimation of the Jakobshavn glacier over the period of November 2010 until March 2016 using altimetry and gravimetry data in combination with a regional climate model. By subtraction of the altimetric and gravimetric mass balance estimates from the SMB, two ice discharge estimates are obtained. This approach does not suffer from the drawbacks involved when estimating ice discharge from velocity fields directly, which are based on offset tracking. Data gaps for long polar nights and clouds in the visible spectrum and decorrelation in general, when the duration between subsequent images over the same location is long, are thus avoided. This is because offset tracking algorithms require recognisable characteristics in subsequent satellite recordings to determine the velocity, i.e. satellite recordings need to be sufficiently correlated.
The altimetry data will be *swath processed*. This means that the full waveform is exploited, which provides an unprecedented spatial sampling and resolution. Conventional altimetry processing retrieves only one height estimation per recorded waveform. In contrast to CryoSat-2's two-antenna system which overcomes this limitation and retracks the entire waveform. After conversion to mass change, this is compared to mass change inferred from GRACE monthly solutions.

1.4. Research objective

This study is conducted to quantify the ice discharge of the Jakobshavn glacier. Three main data sources are used for the estimation of the annual ice discharge. The first main data source is CryoSat-2, providing satellite altimetry data. CryoSat-2 elevation estimates have a relatively high (approximately 1.6×0.4 km^2) spatial resolution. Second main source are the GRACE twin satellites, administered by NASA and DLR. With GRACE, mass anomalies can be inferred at a relatively low spatial resolution (roughly 150×150 km^2). The third main data source is RACMO, a regional climate model maintained by IMAU (Utrecht University) and Dutch Royal Meteorological Institute (KNMI). RACMO provides the SMB over the study area at 1×1 km^2. The temporal resolution of each of these three methods is monthly. However, the CryoSat-2 swaths overlap earlier orbits, such that surface locations are often revisited more than once per month.
This leads to the following research objective:

Derive the ice discharge and its corresponding error budget from swath processed CryoSat-2 volume data, GRACE mass anomalies, and RACMO modelling results over the Jakobshavn drainage basin in Greenland in the period of November 2010 until March 2016.

Three specific research questions will be addressed.

Q. 1 *What are the key parameters in the implementation of the CryoSat-2 swath processing scheme for elevation change estimation?*

Swath processing is a method for transferring CryoSat-2 observations from level 1b to 2. During this processing step, a manual choice of several parameters is required. The question is therefore: which choice of parameters lead to the most accurate and precise elevation estimates with an adequate increase in spatial coverage?

Q. 2 *How can the GRACE mass anomalies, the CryoSat-2 elevation estimates obtained through swath processing and the RACMO modelled SMB be combined consistently to reveal the ice discharge in Jakobshavn in Greenland?*

CryoSat-2 carries an altimeter, by which surface elevations are estimated. GRACE, a gravimetry mission, infers mass anomalies directly. RACMO is a RCM simulating the SMB. Apart from the different physical quantity, each is also retrieved at a different temporal and spatial scale.

Q. 3 *What limitations emerge from the RACMO data inclusion, the GRACE and CryoSat-2 data acquisition and chosen processing methods and how do these jointly affect the ice discharge estimates?*

Following up on Q. 2, the different methods and scales introduce different bottlenecks. These bottlenecks are identified.

1.5. Outline

This introductory chapter forms the basis of the forthcoming chapters. The remainder of this report is structured as such that the research questions can be answered in the written order. Thus, in chapter 2, a CryoSat-2 data derived MB is inferred first. Consecutively in chapter 3, an estimation of the MB with GRACE monthly solutions is derived. Subsequently in chapter 4, RACMO modelling data is used for the retrieval of the ice discharge from the MB. Lastly, an endeavour is made to concisely answer the research questions with corresponding discussion in light of the obtained ice discharge estimates of Jakobshavn drainage basin.

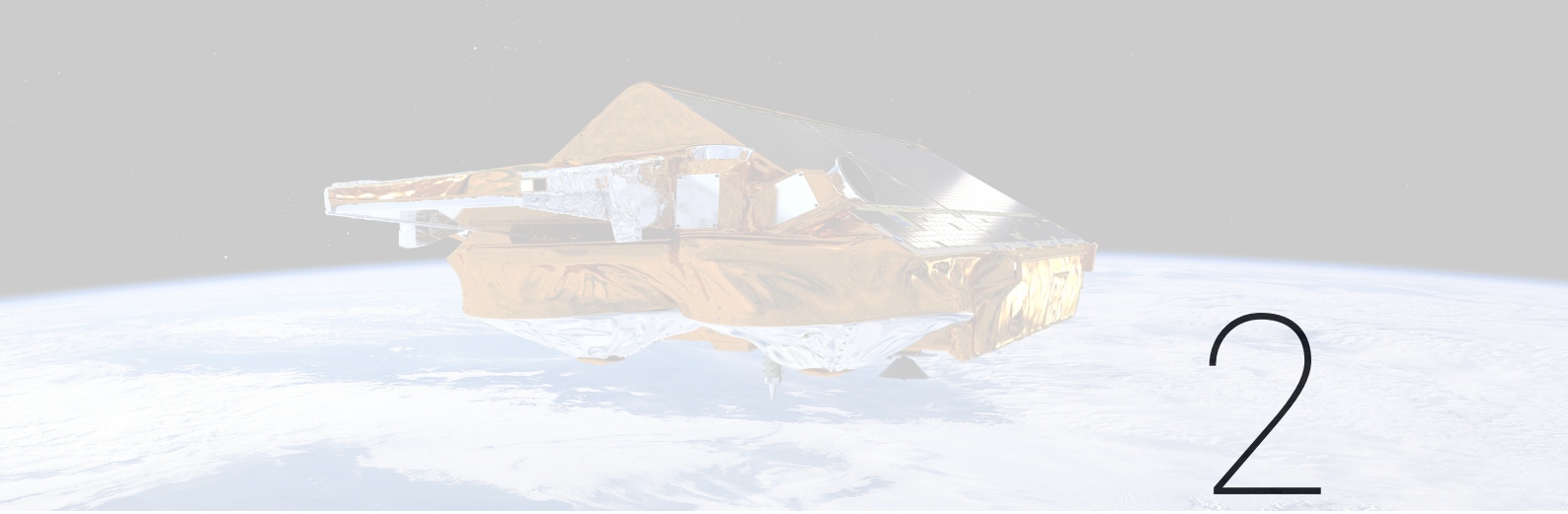

2

Mass change through altimetry

This chapter presents the reader with a brief introduction on the CryoSat-2 mission and its altimeter. This is followed by the applied methodology to infer mass change estimates from a CryoSat-2 L1b data product. Finally, the mass change results and several intermediary products are presented and discussed.

2.1. Introduction: The CryoSat-2 mission

ESA's CryoSat-2 was designed under the *Living-planet* program, which concerns itself with the understanding of Earth's system and its processes to determine the variation of the major ice masses on Earth [ESA, 2017]. CryoSat-2 is equipped with a dual antenna, normal-incidence, radar altimeter, exploiting synthetic aperture radar (SAR) and interferometric processing. With this set-up, CryoSat-2 is ultimately capable of determining surface elevations and surface elevation change [Ratier et al., 2005].
CryoSat-2 began its journey at the Baikonur Cosmodrome, Kazakhstan, on the 8^{th} of April 2010, from where it was launched into space to an altitude of about 720 km. It orbits at a 92° inclination for coverage up to 88° latitude in a non-Sun-synchronous low Earth orbit (LEO) at a speed of roughly 7 km/s [Ratier et al., 2005]. Together with a 369-day orbit repeat and 30-day sub-cycle, it can provide a relatively high temporal and spatial resolution over the Arctics. As a consequence, ground track distance between two consecutive orbits is larger around the equator (approximately 7.5 km) than at higher latitudes (approximately 1.6 km at 70° latitude) [Gourmelen et al., 2017]. Technical details of SIRAL can be found in table 2.1.

Table 2.1: CryoSat-2 altimeter (SIRAL) payload characteristics.
*The transmitted bandwidth is slightly higher (350 MHz), but is only 320 MHz after processing due to a band-pass filter [Galin et al., 2012]. **Initial number of samples per echo was 512, but was increased by factor 2 to alleviate aliasing [Makhoul-Varona et al., 2017].

Parameter	**LRM**	**SAR**	**SIN**
Centre frequency	13.575 GHz (K_u-band)		
Bandwidth	320 MHz*		
Transmit power	25 W		
Noise figure	1.9 dB at duplexer output		
Antenna gain	42 dB		
Antenna 3 dB beam-width (along-track)	1.06° [Scagliola, 2013]		
Antenna 3 dB beam-width (across-track)	1.1992° [Scagliola, 2013]		
Bandwidth	350 MHz		
Compressed pulse length	3.125 ns		
Sample interval	0.47 m		
Samples per echo	128	128	1024**
PRF	1970 Hz	17.8 kHz	17.8 kHz
Burst length	-	3.6 ms	3.6 ms
Burst repetition interval	-	11.7 ms	46.7 ms
Pulses per burst	-	60	60
Azimuth looks	91	240	60

CryoSat-2's altimeter, Synthetic Aperture Radar Interferometric Altimeter (SIRAL), operates in three different modes, each activated over different parts of the world (figure 2.1).

- Low Resolution Mode (LRM) is active above simple topographies (e.g. oceans) and has a footprint size of approximately 1.64 km along and across-track. This mode resembles the conventional radar altimetry with additional pulse compression.
- Synthetic Aperture Radar (SAR) mode is active above moderately coarse topographies (e.g. sea ice) and has a with footprint size of approximately 400 m along-track and 1.64 km across-track.
- Synthetic Aperture Radar Interferometric (SIN) mode is active above complex topographies (e.g. ice cap margins) and has a footprint size of approximately 400 m along-track and 1.64 km across-track. Additionally, it records with two antennas, enabling users to position across-track scatterers.

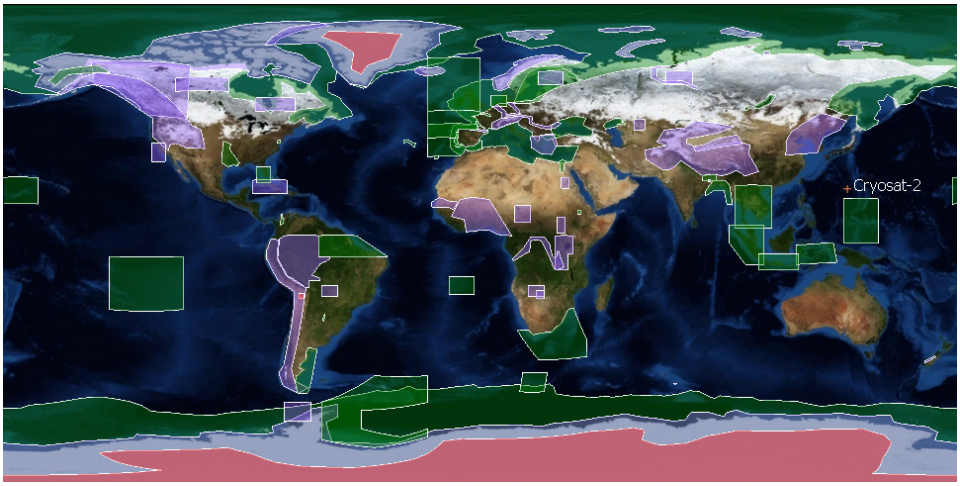

Figure 2.1: Geographical mode mask of the SIRAL instrument on board CryoSat-2. SAR mode in green, SIN mode in purple and LRM in red as well as the remaining transparent parts. In the study area, Greenland, only LRM and SIN mode data is acquired. *Taken from: https://earth.esa.int/web/guest/-/geographical-mode-mask-7107 (version 3.8).*

2.2. Theory

2.2.1. Altimetry

An altimeter is an active remote sensing system, capable of measuring range by recording the time taken between transmission and arrival of a pulse. The arrival time of a pulse is determined based on the incoming power over time (waveform). A strong increase in reflected power indicates strong surface scattering. The time delay corresponding to the strong increase in received power marks the travel time from the satellite to the ground and back, i.e. two-way travel time (equation 2.1):

$$R_0 = \frac{ct}{2}, \tag{2.1}$$

where R is the range in m, c the speed of light in m/s and t the travel time in s. The travel time of the pulse is affected by different error sources, e.g. geophysical and instrumental. The corrected range (R) is therefore described as:

$$R = R_0 + r_{corr}, \tag{2.2}$$

where r_{corr} is the sum of the range corrections. The elevation of the scatterer (H) is then derived by subtracting the corrected range from the known satellite altitude (H_{sat}):

$$H = H_{sat} - R. \tag{2.3}$$

The satellite altitude is continuously estimated using Doppler Orbitography and Radio-positioning Integrated by Satellite (DORIS) and International Laser Ranging Service (ILRS) [Ratier et al., 2005]. H can only directly be inferred using equation 2.3 if estimated from a point directly below the satellite, i.e. at nadir. If the

scatterer is not at nadir the range will appear to be longer such that the elevation is underestimated as well as incorrectly located. The scatterer is commonly not at nadir as the earth's topography is inhomogeneous. Elevation, range and satellite altitude over land are visualised in figure 2.2.

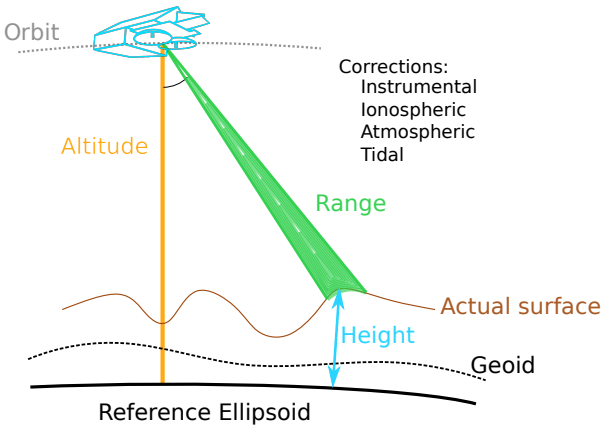

Figure 2.2: Schematic visualisation of involved parameters for elevation determination from range measurements. The altitude and height are perpendicular to the reference ellipsoid. Over Greenland, the geoid is above the reference ellipsoid. *Adapted from Bouzinac [2012].*

Altimeters record the incoming power over time. This recording is called the waveform and is basically a power profile of a fixed number of samples. The recording of the waveform starts not directly after transmission, but a wait time is built in to save resources. The recording starts just before the expected arrival of the surface returns. The recording time is referred to as *window*. The onset of this window is controlled by a separate instrument that tracks ground topography. The time between transmission and recording is called the *window delay*. When orbiting over steep ridges or deep valleys, the recording may start too late or too early. In that case, the waveform contains mostly noise.
Single recordings are generally very noisy. To improve the signal-to-noise ratio (SNR), waveforms are averaged for the reduction of speckle noise. Naturally, this will only improve the SNR if the window is properly timed.
The shape of the waveform is a function of the physical properties and shape of the surface scattering region. For laser altimetry, the waveform shape is strongly dependent on the atmosphere and weakly on the physical properties of the scatterer. For radar this is exactly opposite, due to its longer wavelength. Radar altimeters have been widely used to map the ocean heights. Above oceans, radar waves experience strong surface scattering and very little volume scattering (i.e. returns from scatters below the surface). Strong surface scattering is characterised by a typical steep rise in received power. This steep rise is called the *leading edge*. The time delay corresponding to the leading edge is the desired quantity, which can be used in equation 2.1 to estimate the range. To automatically find the leading edge for millions of waveforms, a *retracker* (an algorithm) is used which fits the waveform and retrieve the time delay of the leading edge. Several approaches and adaptations of retrackers for different surface types can be found in Davis [1993, 1997], Deng and Featherstone [2006], Giles et al. [2007], Gray et al. [2015], Helm et al. [2014], Martin et al. [1983], Nilsson et al. [2016], Wingham et al. [1986], Wingham et al. [2006] and Nanda [2015] for a comparison study. In this project, waveforms scattered from ice, snow and sometimes water are primarily encountered.
For accurate elevation estimates using altimetry, surface scattering is desired, as it ensures the correct elevation estimate. Radar frequencies (CryoSat-2 uses Ku-band, 2.3 cm) can penetrate snow and ice packs up to a few metres [Davis, 1993], causing a significant amount of volume scattering. This alters the waveform and thus also the elevation estimate, because retrackers may incorrectly estimate the range [Lacroix et al., 2008, Ridley and Partington, 1988]. This implies that when ice or snow melts, the scattering regime for radar waves shifts directly and so does the observed elevation. The penetration depth depends on the physical properties of the snow-pack, e.g. snow wetness, grain size and density [Davis, 1997]. Moreover, more surface interaction takes place for radar altimetry than for laser altimetry, because radar altimetry produces larger footprints [Nilsson, 2015].
The penetration depth of the radar frequencies primarily depends on the snow-pack density. Since the near subsurface density in Arctic regions is a function of both time and space, the penetration depth, and thus the offset is also a function of time and space.

Range correction
The corrections in figure 2.2 adjust the range by approximately -2 to -3 metres over land (ice). The involved geophysical and instrumental corrections and magnitudes for CryoSat-2 are taken from Bouzinac [2012] and are briefly described below.

Table 2.2: Geophysical and instrumental range corrections. The sum of these corrections equals r_{corr} and is required to compute the corrected range (equation 2.2). The USO drift factor corrects the window delay. The USO drift factor is equal to USO drift plus one. *Adapted from Bouzinac [2012].*
*Over Arctic regions.

Parameter	Magnitude
Dry tropospheric correction	-1.7 to -2.5 m
Wet tropospheric correction	< 1 mm* [Rees and Rees, 2012]
Ionospheric correction	-6 to -12 cm
Ocean loading tide	-2 to 2 cm
Solid earth tide	-30 to 30 cm
Geocentric polar tide	-2 to 2 cm
Range bias	17 ± 35 mm [Scagliola, 2017]
USO drift	$\approx 10^{-9}$

The geophysical corrections (1-6) are, of course, satellite independent. Over oceans extra corrections are required.

2.2.2. CryoSat-2 altimeter
Compared to conventional (LRM) altimeters , CryoSat-2's system improves on spatial resolution with:

- SAR processing;
- Interferometric processing.

SAR processing improves the along-track resolution by exploiting the frequency spectrum of incoming pulses (using Fast Fourier Transforms (FFT)). This is only useful if there is a pulse-to-pulse coherence [Raney, 1998]. This is realised with the transmission of rapid bursts of 64 pulses each, unlike LRM, where a dedicated pause takes place after every transmitted pulse.

The along-track footprint size is governed by equation 2.4 and results in:

$$\Delta x = \frac{h\lambda}{2V_{s/c}T_{PRF}N_B}, \tag{2.4}$$

where Δx is the along-track resolution in m, h the altimeter height in m, λ the pulse wavelength in m, $V_{s/c}$ the satellite orbital velocity, T_{PRF} the pulse period in s and N_B the number of pulses per burst. For a SAR setup for CryoSat-2 this results in a resolution of 336 m (along-track) by 1.64 km (across-track) The actual resolution is slightly lower, about 400 m, because of the application of a (Hamming) window before applying FFT. Compared to a LRM resolution of 1.64 × 1.64 km^2, SAR improves the along-track resolution by roughly 4 times. We refer to Raney [1998, 2012] for more detailed information on SAR processing.

As mentioned in section 2.2.1, the leading edge is generally not from the satellite's nadir and thus equation 2.3 does not result in the correct elevation. This first arrival is from the *point of closest approach* (POCA) to the satellite receiver, which could differ significantly from the nadir position in sloping terrains [Brenner et al., 1983]. A *digital elevation model* (DEM) can be used to locate the POCA to derive the correct range and echolocation [Bamber, 1994]. However, in some cases (valleys) the result is ambiguous. Also, the footprint expands over sloping terrains, leading to elevation estimations of sub-optimal qualities. This effect is illustrated in figure 2.3.

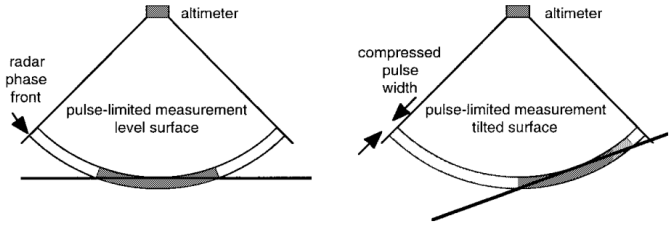

Figure 2.3: Slope induced error effects on pulse-limited altimeters. *Adapted from Jensen [1999].*

A SAR interferometric (SIN) system determines the echolocation without an external DEM. SIN utilises two antennas, separated by a small distance, perpendicular to the flight direction. A single signal return is thus recorded twice, but slightly later by one antenna or the other if the echolocation is either left or right from nadir. This delay manifests itself in a phase difference with respect to the other antenna, which is illustrated in figure 2.4.

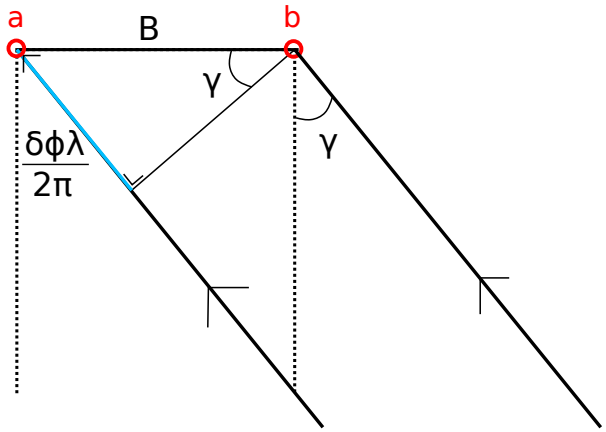

Figure 2.4: A schematic across-track cross-section of CryoSat-2's SIRAL antennas (red circles, *a* and *b*), with the dashed line indicating nadir. For SIN, the primary receiving chain is SIRAL A (SIRAL B is back-up) for which the left-hand (facing flight direction) antenna is used for transmission [Galin et al., 2012]. The antennas are separated by baseline B, perpendicular to the flight direction. The angle γ is the across-track angle. The delay of an incoming signal at antenna a with respect to b is indicated in blue.

The incoming angle of the signal can be calculated with the baseline, i.e. the distance between the two antennas and the path length difference (see equation 2.5) [Wingham et al., 2006]. This allows CryoSat-2 to track the footprint location. The incoming angle is referred to as *look angle*. In short, SIN uses on top of SAR processing to improve the along-track resolution, across-track angle measurements to allow across-track positioning.

$$\gamma = \arcsin\left(\frac{\delta\phi \cdot \lambda}{2\pi \cdot B}\right) - \beta, \tag{2.5}$$

where γ is the look angle in rad, $\delta\phi$ the phase difference in rad, λ the wavelength in m, B the baseline in m and β the satellite roll. The sine argument is called *phase departure* [Galin et al., 2012].
The phase can only be measured from -π up to π for each waveform sample, without knowing the possible additional number of cycles. This is called the *phase ambiguity*. In practice this means that a phase difference of 1.2 π wraps around the π limit and is measured as -0.8 π. Phase wrapping occurs for look angles greater than approximately 0.54°. The integer number of times of 2π ambiguity cannot be resolved from the phase itself, i.e. each waveform sample can be $2\pi \cdot N$ shifted with respect to its neighbouring samples. Moreover, the entire waveform can be wrapped as well. A more illustrative explanation of phase ambiguities is given in paragraph A.4.
The look angle is directly affected by the satellite roll. For CryoSat-2, the satellite roll is nominally slightly above -0.1°. Failing to implement this leads to a elevation difference of approximately 8 metres and well over a kilometre horizontal offset. The attitude information is provided by three star trackers [Ratier et al., 2005].

2.3. Methodology

The next 4 sections are dedicated to the processing steps required to obtain the mass change as well as the intermediary products (see figure 2.5).

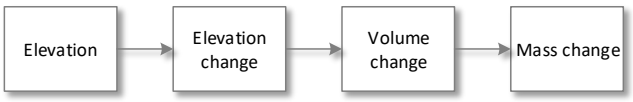

Figure 2.5: Intermediate data products in this chapter. Swath processing results in elevation estimates and is addressed below first. The remaining 3 steps are simply referred to as elevation to elevation change, elevation change to volume change and volume change to mass change.

CryoSat-2 L1B, baseline C, SIN mode altimetry data from November 2010 until March 2016 in Greenland is used. A data file usually contains a few thousand waveforms, each waveform with 1024 waveform samples, along with quality flags, correction data, attitude data, and more [Bouzinac, 2012].

2.3.1. Swath processing

A proof of concept of an interferometric radar altimeter (IRA) was first given by Hawley et al. [2009], continuing on earlier works by Jensen [1999] and Lentz et al. [2002]. Although the proof of concept was an airborne set-up and not spaceborne, it was shown that many more points could be retracked from the waveform with a dual antenna system at the cost of overall accuracy [Gourmelen et al., 2017].
Retracking all waveform samples is in essence possible. However, the waveform does not have uniform quality and information content, as is exemplified below.

- The recording aims to start always a bit before the first scatterer is recorded, meaning that the first X number of bins only noise is measured.
- Waveform subsets where the phase difference wraps many times are indicating steep or complex topography, which are prone to large positioning errors.
- The coherence is a quality measure of the stack (set of waveforms with the same Doppler characteristics). A low coherence indicates that the stack put together to form a sample are much different and vice versa for high coherence.
- Waveform samples at the end of the waveform are often from scatterers far away from nadir, i.e. with a relatively large look angle, which are prone to larger positioning errors.

The swath processing strategy is mostly adopted from Foresta et al. [2018]. The final product of this step is a set of elevation estimates.

Waveform selection

Based on the available flags (quality indicators) within the dataset, waveforms are discarded. Among these are flags that indicate, for instance, an orbit propagation error, window delay inconsistency or datation error. For reference, the SS bit codes of the flags used for waveform selection are 0, 1, 2, 3, 6, 7, 8, 9, 10, 11, 16, 17, 18, 19 and 27 in the *Measurement Confidence Data table* of Bouzinac [2012]. On average, less than 10 waveforms are discarded per file. Secondly, power values are normalised per waveform. Then for each waveform the total energy received is then approximated (by applying trapezoidal rule). Waveforms with an exceedingly high or low energy content are discarded. This selection removes on average less than 10 waveforms as well.

Waveform sample selection

This step makes a selection of waveform samples suitable for retracking. Common method here is selection of waveform samples based on a threshold on coherence, e.g. see Gourmelen et al. [2017], Gray et al. [2013, 2015], Hawley et al. [2009], Helm et al. [2014]. All waveform samples ≥0.8 coherence are e.g. selected and the rest is discarded. A power threshold is sometimes also applied, but is less common. Weissgerber and Gourmelen [2017] pointed out two reasons not to use the coherence and power in the waveform sample selection step.

- Coherence consists of a variable number of looks, which is not a constant within the waveform, nor among waveforms.
- Power is topography dependent. A fixed threshold cannot be used in areas with different topographies.

Although the deviation mentioned in the first point is often relatively small (on average #<5), literature also shows variability in the choice for coherence. Additionally, during this research it was found that higher coherence does not always result in more accurate elevation estimates (see chapter 2.4.1.2). For clarity, samples with power= 0 or coherence ≥ 1 are discarded in any case.
Instead, a sample selection method is used that essentially selects the smooth parts of the phase difference measurements within each waveform. An instructive interpretation of the procedure described by Weissgerber and Gourmelen [2017] and Foresta et al. [2018] is given in section A.2. The applied methodology is given below and slightly differs from what is described in section A.2. The phase difference measurements are referred to as $\Delta\phi$.

1. Create 32 overlapping windows of 64 subsequent waveform samples where each window represents 32 waveform samples. To illustrate, the first window contains sample 1 up to 64, representing samples 1 up to 32. The second window contains sample 17 up to 80, representing samples 33 up to 64. The third window contains sample 49 up to 112, representing samples 65 up to 96, etcetera.
2. Restore the full signal with unit amplitude for each window via $s = e^{i\Delta\phi}$, where i equals $\sqrt{-1}$.
3. Apply FFT to s. The largest magnitude in the amplitude spectrum corresponds with the most dominant slope. Note that $f = \frac{d\Delta\phi}{dn}$. See section A.3 for more information.
4. Find the sign of the slope by taking the sign of the sum of the corresponding unwrapped differentiated phase differences in each window.
5. Create a new set of linear phase differences using the estimated slope and slope sign for each window.
6. Subtract the new linear phase differences from the observed phase differences in each window.
7. Restore the full signal with unit amplitude using the subtracted phase differences: $s_{new} = e^{i\Delta(\Delta\phi)}$, where $\Delta(\Delta\phi)$ is the subtracted phase.
8. Compute dispersion measure $R = \frac{1}{N}|\sum_{n=1}^{N} s_{new}|$, where R is the phase difference dispersion and n is the sample number.
9. Select all samples which are represented by R>0.95 and discard the rest.

The dispersion measure R was introduced by Weissgerber [2017]. When the phase values used to calculate R are distributed as a Dirac, the lengths of s_{new} adds up coherently and R is high. When the phase values used to calculate R are distributed uniformly, the lengths of s_{new} add up incoherently and R is low. The Dirac distribution can be obtained when the slope estimate resembles the slope of the phase values. Smooth phase observations are therefore characterised by an R that is close to 1, whereas strongly alternating phase observations are characterised by an R that is close to 0. In this set-up R has bounds [0,1], because of the unit amplitude of s_{new}. R is inversely proportional to the dispersion of the observed phase differences. R is also referred to as phase difference (PD) dispersion.
This approach differs from the description by Weissgerber and Gourmelen [2017] and Foresta et al. [2018] on the window set-up. Weissgerber and Gourmelen [2017] proposed to use overlapping windows such that each sample is represented by R twice. The highest estimate (i.e. the best fit) is then used. As seen above, our approach maintains overlap for slope estimation, but only estimates one R per sample.

Phase smoothing

The real and imaginary components are reconstructed via $s = e^{i\Delta\phi}$ to which a zero-phase low pass filter is applied [Gray et al., 2013]. This reduces the phase noise at the cost of spatial resolution [Gourmelen et al., 2017].

Phase unwrapping

Phase unwrapping of the observed phase differences is applied by adjusting each jump between two consecutive waveform samples larger than π by adding or subtracting 2π. Although the wraps may have been resolved amongst the waveform samples the entire waveform can be wrapped as well. The look angle γ_k is therefore computed as:

$$\gamma_k = \arcsin\left(\frac{(\delta\phi + 2\pi k)\cdot\lambda}{2\pi\cdot B}\right) - \beta, \tag{2.6}$$

where $\delta\phi$ is the phase difference, with integer k from -5 to 5. Evaluating γ_k results in 11 different look angles, i.e. *candidates*. Each of these look angles are used to geolocate the scatterer. Ultimately, the elevation estimate closest to the DEM is assumed to be the correct one.
In the baseline C product the satellite's internal roll is uncorrected for light aberrations in the star tracker measurements [Scagliola, 2018]. Therefore, an external dataset is included, published by ESA on the 2^{nd} of February 2018, that corrects for the satellite's roll inconsistencies for recordings since November 2010.

Range processing

For each sample the bin number is known and therefore the time delay. Together with the window delay, the range can be computed with equation 2.7:

$$R = \frac{c}{2}\left(\Delta t_{window} + n\cdot\Delta t - \frac{N\cdot\Delta t}{2}\right) + r_{corr}, \tag{2.7}$$

where Δt_{window} is the window delay in s, n the bin number, Δt the sample time per bin in s and N the total number of samples per waveform. r_{corr} represents the geophysical corrections and range correction that need to be applied and can be formulated as in equation 2.8 above continental ice [Bouzinac, 2012]:

$$\begin{aligned} r_{corr} = {} & r_{Ocean\,loading\,tide} + r_{Solid\,Earth\,tide} + r_{Geocentric\,polar\,tide} + \\ & r_{Dry\,tropospheric\,correction} + r_{Wet\,tropospheric\,correction} + r_{Ionospheric\,correction} + \\ & r_{range}. \end{aligned} \tag{2.8}$$

r_{corr} usually ranges from 1 to 3 metres.

Geolocation

The ellipsoidal heights of the scatterers (h_p) are computed with equation 2.9 (within the WGS84 reference system):

$$h_{p,k} = \sqrt{R^2 + (H_{sat} + N)^2 - 2R\cdot(H_{sat} + N)\cdot\cos\gamma_i} - N, \tag{2.9}$$

where N the radius of curvature and γ_k the look angle for k (see paragraph 2.3.1.4). The radius of curvature can be determined with the satellite latitude θ according to equation 2.10:

$$N = \frac{a}{\sqrt{1 - e^2\sin^2\theta}}, \tag{2.10}$$

where a is the semi-major axis of the Earths' ellipsoid and e the eccentricity (see section A.8 in the appendix for more details). An illustration of equation 2.9 is given in figure 2.6.

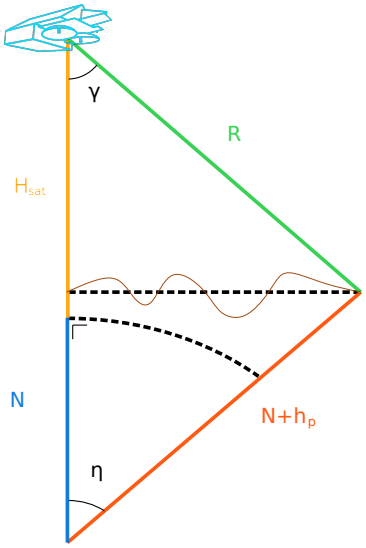

Figure 2.6: Geometry of geolocation problem at equal latitudes. η and γ are very small, <0.15° and <1.5° (typical), respectively, such that in reality the geometry is much more elongated. Typical values for H_{sat}, R, N are roughly 724 km, 723 km and 6397 km, respectively. Figure is not to scale.

The latitude and longitude can be calculated using MATLAB's `reckon();` function, which calculates new positions based on azimuth, arc length and initial latitude and longitude. This is also called the *direct geodesic problem*. MATLAB uses Vincenty's formulas [Vincenty, 1975] to solve the direct geodesic problem. The azimuth within the direct geodesic problem is 90° clockwise or anti-clockwise to the flight direction and the arc length L_{arc} can be derived using equation 2.11:

$$L_{arc} = \frac{N \cdot R \cdot \sin \eta}{H_{sat} + N}. \tag{2.11}$$

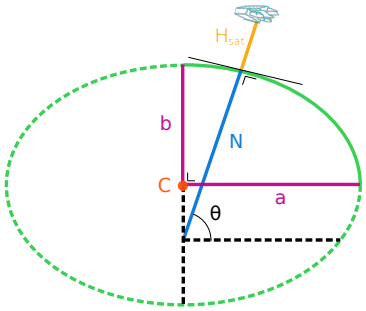

Figure 2.7: Schematic of the reference ellipsoid (not to scale), with centre C, radius of curvature N, latitude θ and satellite altitude above the reference ellipsoid H_{sat}. a and b are the semi-major and semi-minor axis of the WGS84 reference ellipsoid, respectively.

Elevation difference

The elevation difference is defined as the elevation estimate minus the DEM elevation (equation 2.12). The candidate whose elevation is closest to the DEM is selected for each scatterer. The DEM is taken from the GIMP and is based on World View stereo imagery from 1 January 2009 to 31 December 2015 [Howat et al., 2017] with a 90 m resolution.

The elevation difference is a sum of different components. 1) the true elevation difference between h_p and H_{DEM} (ΔH), 2) an elevation change due to ice mass loss or gain ($\frac{dh}{dt}$), 3) a resolution error (ε_{res}) and 4) the static DEM elevation error (ε_{DEM}), which is the accuracy of the DEM. In short:

$$\varepsilon_{elev} = h_p - H_{DEM} = \Delta H + \Delta t \frac{dh}{dt} + \varepsilon_{res} + \varepsilon_{DEM}, \tag{2.12}$$

where Δt is the time between creation of the DEM and observation. It is possible to retrieve a better description of the elevation difference when accounting for the last 3 components in equation 2.12. Foresta et al.

[2018] corrected for the elevation change due to ice mass loss or gain. When the drift is strong or time difference is large, such a correction may help phase unwrapping, preventing the selection of wrong candidates. However, the drift correction is spatially and temporally dependent, which complicates this procedure. Instead, to minimise the impact of the drift onto our results the most recent DEM [Howat et al., 2017] compiled from datasets from 2009 until 2015 is used. ε_{res} is approximated to the first order through bi-linear interpolation. Lastly, ε_{DEM} ranges is 1.6 or 2.7 m (1-σ) [Howat et al., 2017] (depending on data origin) in the Jakobshavn drainage basin.
On the basis of the aforementioned it is possible a sample is incorrectly unwrapped due to the fact that $\varepsilon_{elev} \neq \Delta H$. However, addition or subtraction of 2π results in an elevation change in the order 100 m [Gourmelen et al., 2017]. Exact prediction of the level of accuracy required is difficult due to inhomogeneous topography [Gourmelen et al., 2017]. Considering the magnitude of elevation change, the error sources of the DEM, and the proofs of concept by Foresta et al. [2016, 2018], Gourmelen et al. [2017], Weissgerber and Gourmelen [2017] the DEM is assumed adequate for global phase unwrapping.
Wang and Holland [2018] found that the strongest elevation change rates can be up to -20 m/yr in the Jakobshavn drainage basin. Based on the change rates and possible error in the DEM, points that are differing from the DEM by more than 100 m are discarded. Furthermore, results positioned on rocky terrain or water are mostly discarded as well using an ice mask [Howat, 2017] (appendix A.10.3.6) . Subsequently, the points outside the range window limit plus-minus 100 m are also discarded. Optionally, points can be discarded based on the DEM-derived slope. Positioning errors result in elevation differences, which may be larger on steep slopes than on gentle slopes [Gray et al., 2013]. This is addressed when applying parameter optimisation.

Validation of results

The observed elevation difference can also be computed with respect to Operation IceBridge (OIB) elevation data instead of a DEM. OIB is an airborne NASA mission that has been designed to bridge the data gap between ICESat and ICESat-2 (spaceborne laser altimetry missions) [DeWitt and Zell, 2010, Zell, 2017b]. OIB campaigns take place since 2009, but only for a few months each year. Figure 2.8 shows the campaign map of 2015.
The OIB laser altimeter, Airborne Topographic Mapper (ATM), [Zell, 2017a] operates at elevations of 500 to 750 metres above the ice surface [Martin et al., 2012], mainly from March until May. OIB precision and accuracy are (horz./vert.: 14 cm/3 cm) and (horz./vert.: 74 cm/6.6 cm), respectively. The footprint size is 1 m in diameter.

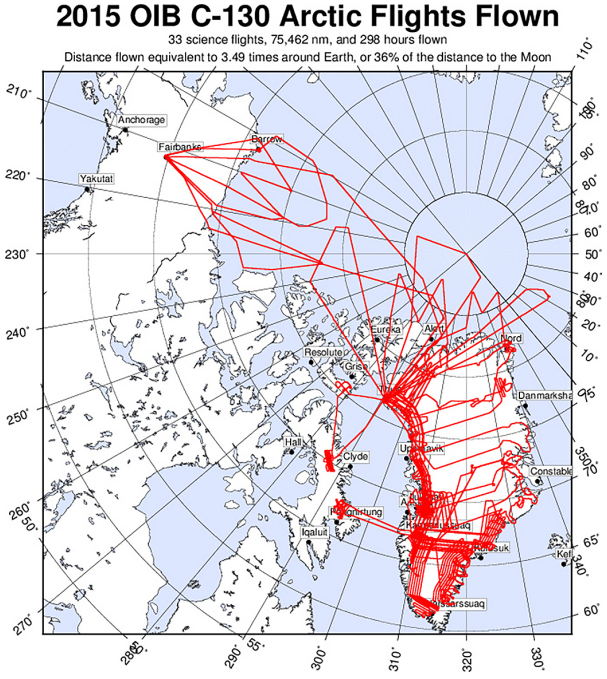

Figure 2.8: Flight paths during the OIB campaign in 2015 on the northern hemisphere. *Taken from Zell [2017c].*

Validation of the elevation estimates is done only for data recorded in April, because during that time of the year the surface height is relatively stable (minor melt and precipitation) [Gourmelen et al., 2017]. In the case of observations over melt ponds, the difference in scattering behaviour of radar and laser pulses are expected to be minimal (surface scattering). In case of snow or ice, volume scattering of the radar pulse is expected, introducing a bias that becomes visible when comparing to laser altimetry. In addition, following Gourmelen et al. [2017], comparisons between the CryoSat-2 elevation estimates and airborne elevations (from ATM, OIB) are made only if the distance between points is shorter than 50 metres in space within 10 days' time. The comparisons are realised using nearest neighbour interpolation.
Due to the specifications of OIB elevation data, OIB elevations are considered more accurate and precise than the proposed DEM elevations. However, the OIB is sparsely distributed in time and space such that the number comparisons is limited. The observed elevation differences from DEM and from OIB are therefore compared. Based on the correlation between the two, the use of the DEM can be approved or rejected.
The correlation between DEM elevation difference and OIB elevation difference is 0.82 (see figure 2.9a). The barycentre of the scatter plot lies near zero metre OIB elevation difference and between -35 and -5 m DEM elevation difference. Based on the strong correlation of DEM elevation difference with OIB elevation difference and apparent fixed offset between the two elevation differences, the DEM is assumed to be an adequate measure for computing the elevation difference of each scatterer.

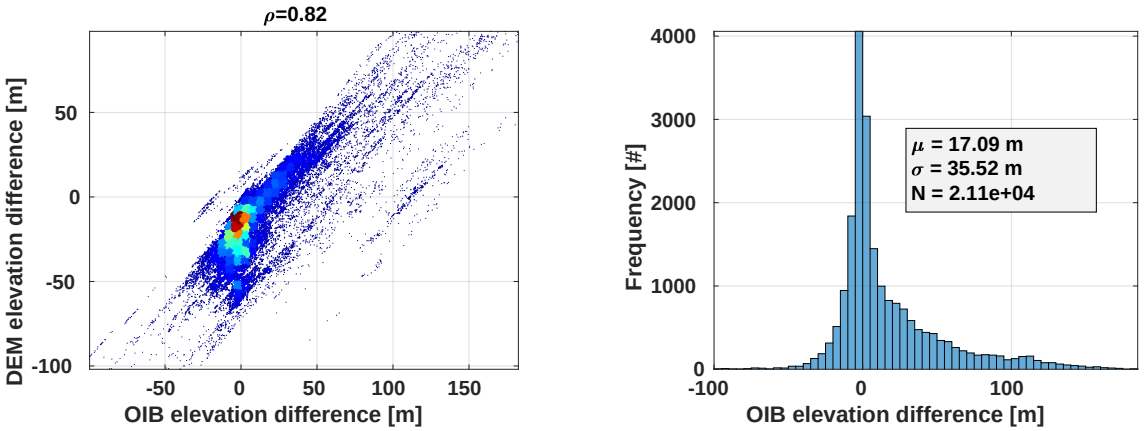

(a) Scatter plot of elevation difference of retracked points with marginal data editing. The warmer colours indicate higher point density.

(b) Histogram of the OIB elevation differences in figure 2.9a.

Figure 2.9: Comparison of elevation of retracked points without optimisation and OIB observations.

The mean OIB elevation difference is relatively high due to outliers over 300 m elevation difference. After the selection and application of appropriate parameters, these outliers will be discarded as much as possible. Outlier removal then also mitigates the standard deviation. At this stage, only 55% of the points are within 15 metres OIB elevation error.

2.3.2. Swath processing parameter selection

To obtain reasonably accurate and precise elevation estimates, processing settings must be set accordingly. Parameters are varied and the elevation result is compared against the DEM. The parameters considered are:

- Waveform energy
- Power
- Coherence
- Phase difference dispersion
- Look angle
- DEM slope

The goal is to maximise the number of retracked points, while minimising the dispersion of the elevation differences. The phase difference dispersion is considered as a possible replacement for the coherence (see section 2.3.1.2). The number of parameters pose a 6-dimensional optimisation problem. To accommodate the two requirements, the following optimisation criterion is proposed: $min(\frac{\sigma}{log_{10}(N)})$, where σ is the standard deviation of the elevation differences with the DEM and N is the total number of retracked points. For this analysis, all samples from all unflagged waveforms are selected. Then all elevation estimates with a maximum DEM elevation difference of 250 m are discarded to remove the most severe outliers. Thereafter, all elevation estimates differing more than 100 m from the basin mean elevation difference are discarded. Additionally, all samples with a power=0 or a coherence≥1 are discarded as well. This is done for 6 small drainage basins (see figure A.4b) in Greenland during April 2014 are used. No further thresholds for waveform energy, power, coherence, phase difference dispersion, look angle or DEM slope are applied to this dataset. The search for the optimum takes place by linearly varying a set of thresholds and regarding the parameters as independent.

2.3.3. Elevation to elevation change

The swath processing product consists of numerous ($\approx 10^6$ #/km^2 collected over nearly 6 years' time) elevation estimates scattered along the coast up to a few 100 km inland of the Jakobshavn drainage basin. This section describes how the elevation estimates are converted to elevation changes ($\frac{dh}{dt}$) per grid cell in the entire Jakobshavn drainage basin.

Weighted Least Squares Estimation

The elevation change rates are estimated using the scheme proposed by Wouters et al. [2015]. The functional model, adopted from Nilsson et al. [2016] and expanded, is:

$$h(x,y,t) = a_0 + a_1\Delta x + a_2\Delta y + a_3\Delta x\Delta y + a_4\Delta x^2 + a_5\Delta y^2 + a_6\Delta t + a_7\cos(2\pi\Delta t) + a_8\sin(2\pi\Delta t) + a_9\cos(4\pi\Delta t) + a_{10}\sin(4\pi\Delta t), \quad (2.13)$$

where $h(x,y,t)$ are elevation estimates, a_0 elevation offset, a_1 slope in x-direction, a_2 slope in y-direction, , a_3 cross-slope in $x-y$-direction, a_4 curvature in x-direction, a_5 curvature in y-direction, a_6 elevation change, a_7 and a_8 as well as a_9 and a_{10} are amplitude terms of the seasonal signal, i.e. $\sqrt{a_7^2 + a_8^2}$. The phase (ϕ) of the seasonal signal can also be assessed with $\phi = \arctan 2(\frac{a_8}{a_7})$, where $\arctan 2(...)$ is the four-quadrant inverse tangent. Δx and Δy are $(x_p - x_c)$ and $(y_p - y_c)$, i.e. the x and y-distance from data point to evaluation point, respectively. Δt is equal to $(t - t_0)$, i.e. the time passed the with respect to an arbitrary reference time t_0. The following restrictions on the LSE input (retracked points) are imposed [Wouters et al., 2015]:

- The retracked points should be ≤250 m away from the evaluation point;
- The number of retracked points should be ≥16;
- The used retracked points should be acquired during ≥4 overpasses;
- The used retracked points should span ≥2 years.

The weight assigned to each observation is computed by [Nilsson et al., 2016]:

$$w_i = \frac{1}{1 + \frac{d_i^2}{\rho^2}}, \quad (2.14)$$

where d_i is the distance from the estimation point to point i and ρ the correlation parameter set to half the search radius. w_i penalises points farther away from the estimation point. This weighting thus better preserves local surface details [Nilsson, 2015]. To reduce contamination of the estimated parameters by outliers, an iterative scheme is applied in which observations with residuals larger than two times the weighted standard deviation are discarded [Nilsson, 2015].

$$\mathbf{w}|\mathbf{r}| > 2\sigma_y = 2\sqrt{\frac{\mathbf{r}^T W \mathbf{r}}{n-p}}, \quad (2.15)$$

where **w** is a weight vector and W a diagonal matrix with weights from equation 2.14, σ_y the standard deviation of data noise (assuming noise is uncorrelated), **r** a residual vector, n the number of observations and p the number of estimated parameters (11). Forward propagation of the error then results in a scaled covariance matrix with squared standard errors of each parameter estimate on the diagonal [Nilsson, 2015] (see equation 2.16).

$$Q_{\hat{x}\hat{x}} = \sigma_y^2 (A^T W A)^{-1} \tag{2.16}$$

The WLSE is repeated until no more outliers are found or reaches 25 iterations. Elevation change estimates that do not include the evaluation point are discarded [Wouters et al., 2015]. Elevation change estimates outside the interval [-30,15] m/yr are discarded. Thickening or thinning rates outside that interval are not expected in the Jakobshavn drainage basin [Wang and Holland, 2018]. An iterative 2-σ filter (with maximum 25 iterations) is used to further reduce the number of outliers within each grid cell. The valid elevation change estimates are averaged for each grid cell (see figure 2.10). A standard deviation is computed from the elevation change estimates used for averaging, which signifies the uncertainty for the averaged elevation change estimate [Wouters et al., 2015].
Two extra steps were taken to reduce computational time, because the total number of points can be large (>10^6). Firstly, WGS84 (ellipsoidal) coordinates are projected to EPSG3413 (Cartesian) coordinates, a polar stereographic (north) projection with WGS84 elevations (see section A.8 in the appendix). Distortion in EPSG3413 for Greenland is minimal because the grid is tangent to 70°N. Distance calculations are less expensive in Cartesian coordinates than in ellipsoidal coordinates. Secondly, all elevation observations are assigned to a grid. Search for data points is then limited to only 9 grid cells using the approach illustrated in figure 2.10.

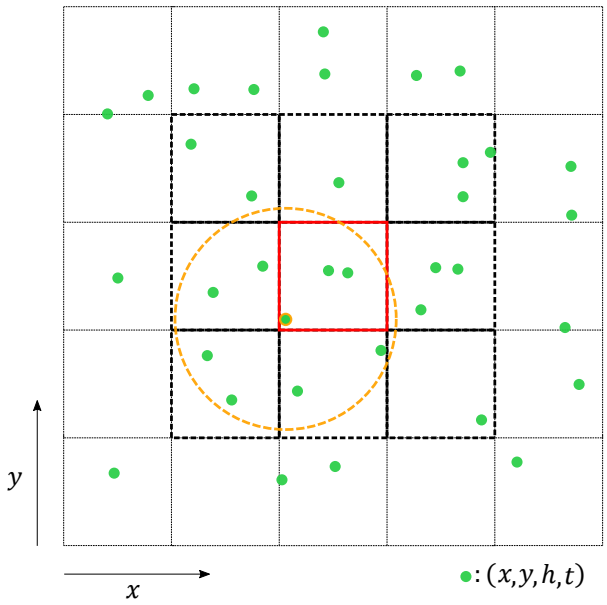

Figure 2.10: Schematic of the grid used for the elevation change estimation. The elevation change is estimated at all data points. For each data point, an elevation change estimate is made using WLSE with all data points within 250 m distance. A grid with cells of the same size as the search radius reduces the search for points meeting the distance criterion to 9 grid cells.

Elevation change estimates covering the entire Jakobshavn drainage basin

The area hat is eligible for swath processing, i.e. the area that CryoSat-2 observes in SIN mode, cover only coastal regions. A large part of the Jakobshavn drainage basin is observed in LRM (see figure 2.11). To that end, elevation change estimates are taken from Gourmelen et al. [2017]. This data is available at 1000 m resolution, with its elevation change estimates based on elevation estimates from 2011 until 2016.

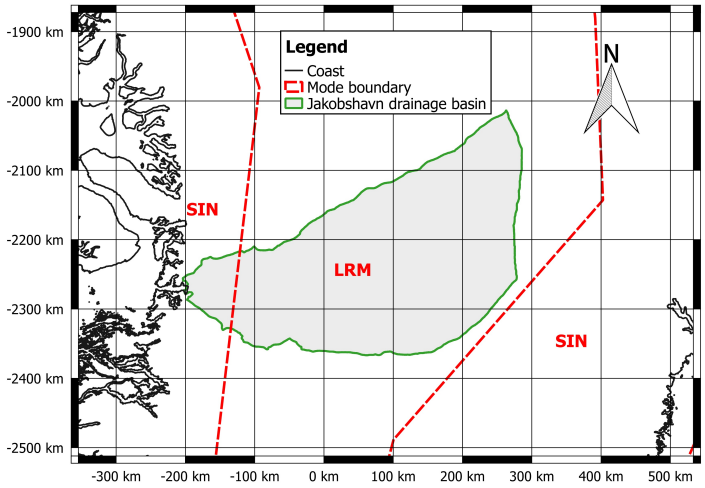

Figure 2.11: Visualisation of SIN and LRM mode coverage over the Jakobshavn drainage basin. The SIN mode covers only a small part of the Jakobshavn drainage basin. The elevation change estimates in the LRM mode area are taken from Gourmelen et al. [2017] (`https://cryotop-evolution.org/datasets/`, gridded dataset).

All elevation change estimates with an error >0.5 m/yr are discarded. Then the estimates from Gourmelen et al. [2017] are combined with ours. Subsequently, the ensemble of elevation change estimates are interpolated using natural neigbour interpolation [Amidror, 2002] to occupy 250 × 250 m^2 grid cells in the entire Jakobshavn drainage basin.

2.3.4. Elevation change to volume change

For a volume change estimate based on elevation change rate, the hypsometric method is used. Hypsometric averaging integrates the elevation change rates and accounts for missing rates [Foresta et al., 2016, 2018, Moholdt et al., 2010] .

The hypsometric method is well known in the field of hydrology. It is applied to rain gauge data to interpolate precipitation rates. Rain gauge data is commonly sparsely distributed and often missing in the higher elevated areas that generally experience more precipitation. Low order polynomials are then used to represent the relation between elevation and precipitation. [Dingman, 2015] In the context of this research, elevation is related to elevation change in two ways. First, the temperature is lower at higher elevations which inhibits melt. Secondly, the glacier outlet is located at low elevation, exhibiting thinning when the glacier is actively discharging ice. The polynomial fit then serves two purposes, 1) to make interpolate data gaps and 2) to integrate the elevation change rates for a volume estimate. Hypsometric averaging is performed using [Moholdt et al., 2010]:

$$\frac{dV}{dt} = \sum_{i=1}^{N} p(h_i) \cdot A_i, \tag{2.17}$$

where $\frac{dV}{dt}$ is the volume change, N the total number of elevation bins, $p(h_i)$ the polynomial function evaluated at centre bin height h_i and surface area A_i for bin i. A_i has been corrected for distortion using [Knowles, 1993]:

$$A_i = A_{i,uncorrected} \cdot \left(\frac{1+\sin\theta_0}{1+\sin\theta_i}\right)^2, \tag{2.18}$$

where A_i is the corrected surface area, $A_{i,uncorrected}$ the uncorrected surface area, θ_0 the normal degree latitude (70°N) and θ_i the centre latitude of surface area A_i. The elevation of an estimation point is derived from a DEM [Howat et al., 2017]. For $p(h_i)$, different functions were tested and compared based on the physical representation and root means square error (RMSE). Following Moholdt et al. [2010], a 2^{nd}, 3^{rd} and 4^{th} order polynomial and a mean and median were used. h_i is 25 m , 75 m, 125 m and so forth in case of a 50 m bin size. Hypsometric averaging uses the elevation change rates from the fitted function rather than the actual elevation change rates. This suppresses outliers further, assumed that the fit is representative. A DEM [Howat et al., 2017] is used to assess elevation of present and missing elevation change estimates. In this way, hypsometric averaging can account for data gaps. The corresponding standard error can be calculated using

[Moholdt et al., 2010]:

$$\hat{\varepsilon} = \frac{\sigma_{fit}}{\sqrt{n-p}}, \tag{2.19}$$

where $\hat{\varepsilon}$ is the standard error of the regional average elevation change of all grid cells, σ_{fit} the RMSE of $p(h_i)$ and n is the number of uncorrelated grid cells and p the number of parameters estimated when fitting. Grid cells are assumed to have fully decorrelated at 5 km distance, such that $n = A/(\pi \cdot 5^2)$, with area of interest A in km^2 [Wouters et al., 2015].
The standard volume error (E_V) integrated over the entire surface area can then be derived via [Moholdt et al., 2010]:

$$E_V = \sqrt{(\hat{\varepsilon} \cdot A)^2 + \left(0.1 \cdot \frac{dV}{dt}\right)^2}. \tag{2.20}$$

Using the root sum of squares, a basin outline uncertainty of 10% (method from Moholdt et al. [2010]) is included. The root sum of squares (RSS) is valid on the condition that the $\hat{\varepsilon}$ does not vary disproportionally in the potential area where there is the outline uncertainty (independent errors).
The basin outline uncertainty comes from the fact that the Jakobshavn glacier is retreating, changing the surface area and volume change (equation 2.17). The basin outline uncertainty is estimated at 10%. This estimate can be considered as conservative, because the Jakobshavn drainage basin only has one reasonably sized outlet glacier.

2.3.5. Volume change to mass change

The conversion of volume (change) to mass (change) requires density information of the accumulation or ablation signal. Space and time varying near-surface density data over the Jakobshavn drainage basin is unfortunately not available. Several methods exist to convert volumes to mass [Bader, 1954, McMillan et al., 2016, Moholdt et al., 2010, Nuth et al., 2010, Slobbe et al., 2009, Thomas et al., 2006, Wouters et al., 2015]. As described by McMillan et al. [2016], two methods for the conversion of volume-based estimates to mass-based estimates are well established. The first method consists of multiplication of the volumes with a density model. This density model describes the density of volume loss in each grid cell and in this way accounts for dynamic and SMB processes. The second method requires knowledge of the firn column thickness in space and time to separate dynamic and SMB processes. A firn densification model (FDM) is commonly used to acquire such knowledge as it describes the change of the thickness of the snow pack due to precipitation, compaction and melt of snow.
The mass change (ΔM) in each grid cell can be described as:

$$\Delta M = \Delta V \cdot \rho_{eff} = \Delta V_{ice} \cdot \rho_{ice} + \Delta V_{snow} \cdot \rho_{snow}, \tag{2.21}$$

where ΔV is the total volume change, ρ_{eff} the effective density, ΔV_{ice} ice volume change, ρ_{ice} density of ice, ΔV_{snow} snow volume change and ρ_{snow} the density of snow. According to CryTop data [Gourmelen et al., 2017], basin wide thinning can be expected. That means ΔV is also negative. According to the derivation in A.7 in the appendix, the effective density exceeds the density of ice when $\Delta V_{ice} < -\Delta V_{snow}$ and $\Delta V_{snow} > 0$ in case of volume loss. Near the terminus ΔV_{ice} contributes most to the volume loss as a consequence of ice melt and discharge. The absolute contribution of ΔV_{ice} is expected to gradually decrease inland where little ice dynamics is expected. The contribution of ΔV_{snow} to the total volume loss is expected to be marginal near the terminus. Above the Equilibrium Line Altitude (ELA), snow processes start to gradually play a more significant role. $\Delta V_{snow} > 0$ may occur, but $\Delta V_{ice} < -\Delta V_{snow}$ is unlikely, because the SMB variations are too large with respect to the ice dynamics that occur. Furthermore, the sign of the linear trend of a FDM is negative basin-wide. A negative trend in the FDM provides confidence that ΔV_{snow} is also negative. Therefore, it is expected that the effective density does not exceed the density of ice. Thereby, Huss [2013] found that densities of 850±60 kg/m^3 are often adequate under conditions that are or are likely met in this case, i.e. 1) long observation period (>3 yrs), 2) relatively large volume changes (Gt/yr) and 3) no strong changes in MB gradients.
How close the effective density is to that of ice and that of snow depends on the contribution of each volume component in equation 2.21.

Density model

In this study, a linear density model is used. In this linear density model three zones are assumed. An ice density is assumed (917 kg/m^3) from 0 to ELA, which is around 1500 m elevation. From 1500 up to around

2000 m a linearly decreasing density is assumed. The density decreases until to that of snow, which is also assumed for everything above 2000 m elevation. The ELA comes with an uncertainty as it covers a relatively wide transition band of altitudes at which the SMB crosses equilibrium (see figure 4.3 in chapter 4). The ELA is therefore only certain up to a few 100 m. The snow density also comes with a significant uncertainty, because no actual density information is available. Furthermore, compaction takes place in the Jakobshavn basin, which can be considered as volume losses with zero density. To that end, the ELA and the density of snow is varied to account for these uncertainties.
The ELA is varied from 1250 m up to 1750 m in steps of 50 m. Approximately 96% of the Jakobshavn drainage basin lies above 1250 m. The snow density is varied from 300 kg/m^3 up to 700 kg/m^3 in steps of 25 kg/m^3.
Additionally, an alternative density model based on flow velocity is applied. To that end, a flow velocity map is used [Nagler et al., 2015] (see figure A.19). This flow velocity map was derived from Sentinel-1 SAR data over the period 01-10-2015 to 31-10-2016. Volumes where the flow velocity is above e.g. 500 m/yr are considered dynamic and are multiplied with the density of ice. The rest is multiplied with the density of snow. The flow velocity boundary for separating ice and snow losses is varied from 50 m/yr up to 750 m/yr in steps of 25 m/yr. The snow density is varied over the same range as above.
The standard deviation of the ensemble of mass change estimates is taken as the conversion error σ_{conv}. The total error (E_M) is computed by applying the RSS to the converted volume error (E_V) and conversion error [Moholdt et al., 2010]:

$$E_M = \sqrt{(E_V \cdot \rho_{ice} \cdot 10^{-3})^2 + \sigma_{conv}^2}. \tag{2.22}$$

The volume error is converted to mass by assuming the density of ice. Conversion from km^3 to Gt using the density of ice (in kg/m^3) introduces a factor of 10^{-3}.

2.4. Results & Discussion

In this section, optimal parameters for swath processing are presented. This is followed by elevation change estimates which are converted to volume change using hypsometric averaging. Finally density models are applied to convert volume change to mass change

2.4.1. Swath processing parameter selection

First, the results of the parameter analysis are given. This is a multi-dimensional optimisation problem, which is solved step-wise, because the parameters are assumed independent. Furthermore, visualisation becomes possible through this approach. Only the figures for the Jakobshavn (7-1 in table 2.3) drainage basin are presented here (see section 2.3.2 for more details on the used dataset). The rest can be found in the appendix (A.10). Standard deviations may sometimes seem exceedingly high, because only one or two parameters are optimised at a time. Meaning that the other parameters are not set at all. Thus, the standard deviation visible in the plots and chosen as best are best towards that one or two variables. The location of the X in the figures marks the optimum of the proposed criterion. The standard deviation of elevation differences with the DEM is a function of observation period when the surface elevation is dynamic. The obtained standard deviation of the optimised ensemble of elevation differences is optimised assuming a static surface elevation. The final standard deviation of elevation differences with respect to a DEM can therefore only be considered as an upper bound. Instead, the quality of elevation estimates is given by comparing a subset of elevations estimates with OIB elevations.
The number of points involved in the analysis are given in table 2.3 below.

Table 2.3: Number of available points per drainage basin used for optimising threshold values. 7-1 is the Jakobshavn drainage basin. The location of the other basins can be found in figure A.4b.

Basin	Number of available points
1-2	16190035
1-4	6463637
4-2	6133439
4-3	3815556
7-1	957459
8-2	8211351
Total	41771477

Normalised waveform energy

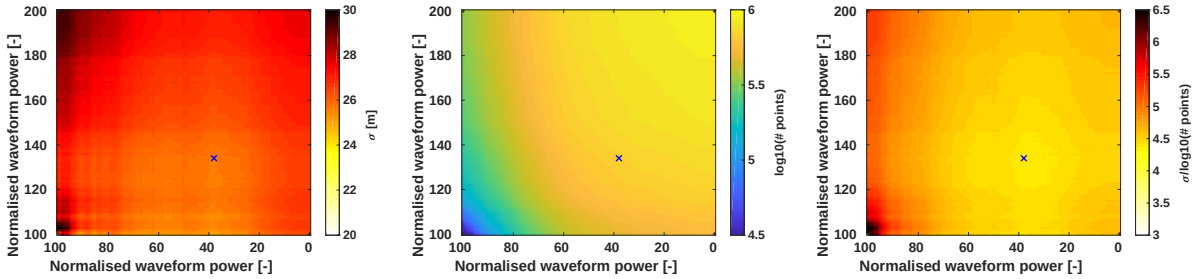

(a) Standard deviation of the elevation errors.

(b) Number of retracked points.

(c) Optimisation criterion.

Figure 2.12: Variation of upper and lower normalised waveform power threshold. The blue cross indicates the position that minimises the optimisation criterion best. The waveform energy has a lower and upper bound for rejection. Therefore, figure 2.12 has been plotted from 0 to 100 on the x-axis and from 100 to 200 on the y-axis for the lower and upper bound, respectively. The coordinates of the blue cross thus provides the best lower threshold (x-axis) and upper threshold (y-axis). Elevation estimates are from the Jakobshavn drainage basin in April 2014.

According to figure 2.12c, waveforms with an integrated power above 134 or below 38 degrade the criterion value, leading to sub-optimal results. Together with the results in 5 other drainage basins it can be concluded that the normalised waveform power desirably remains below 135 and above 35 (paragraph A.10.3.1). The reduction in standard deviation of elevation differences among the basins are 3% (basin 1-2), 1% (basin 1-4), 5% (basin 4-2), 9% (basin 4-3), 8% (basin 7-1) and 9% (basin 8-2).
Waveforms exceeding the upper limit are noisy waveforms. In Jakobshavn, such waveforms originate from the area near the terminus. The glacier is oriented along the latitudes, whereas the satellite orbit is along the longitudes. A longitudinal ground track over such a glacier is prone to high topographic fluctuations, because the topography resembles many consecutive steep valleys. This causes the recording window to start too early or too late, such that the returned signal is uninterpretable and mainly noise is recorded. Figure 2.13 shows an example of a 'normal' and a ill-timed waveform recording.

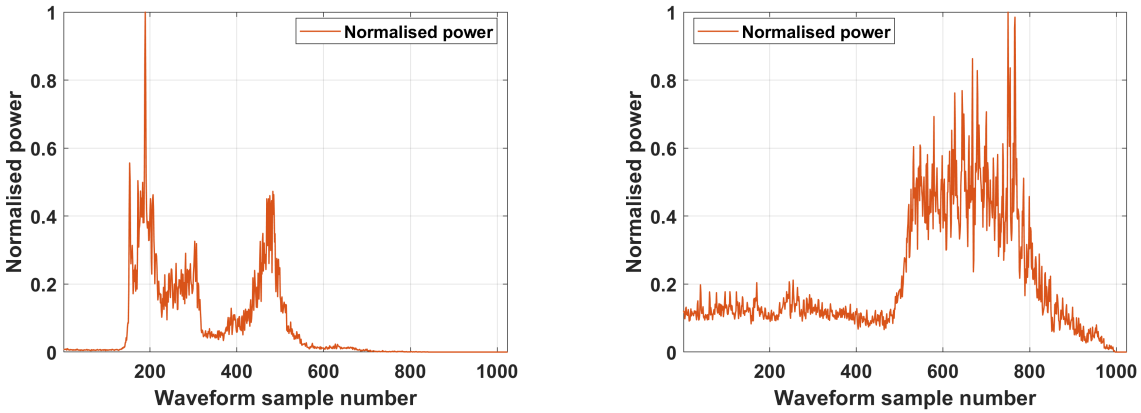

(a) Regular normalised power recording.

(b) Normalised power recording with poor window timing.

Figure 2.13: The waveform energy is the integrated area under the curve. Figure 2.13b shows, on average, samples with high waveform energy, even at early times. This can be used as an indicator for noisy waveforms (see e.g. Helm et al. [2014]).

Waveforms exceeding the lower limit are characterised by one strong spike with no significant trailing edge. Spikes generally indicate specular reflections. No trailing edge indicates limited surface area over which the footprint can expand adequately. After visual inspection it was found low waveform energy recordings primarily take place over bare rocky terrains at the coasts of Greenland. This agrees with the CryoSat-2 waveform signatures found over land by Göttle et al. [2016].

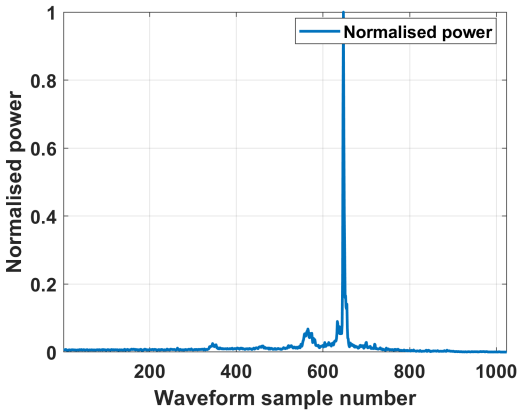

(a) Low normalised energy recording over uncovered, rocky terrain.

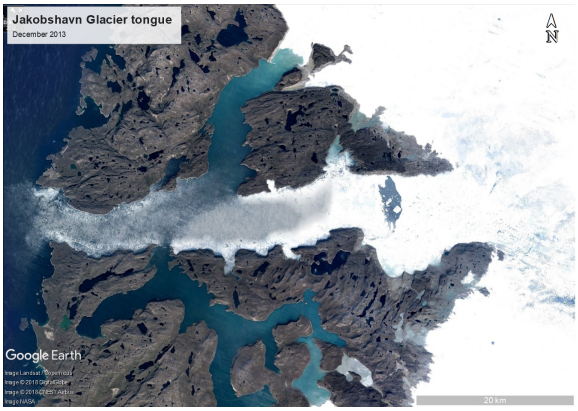

(b) True colour image of the Jakobshavn glacier (December 2013). *Taken from Google Earth, Landsat / Copernicus image.*

Figure 2.14: The exposed rocky terrain in b) causes waveforms as recorded in a).

Power, coherence, phase difference dispersion and look angle

First, scatter plots of the 4 parameters are made to inspect the effectivity of a threshold on each of the parameters. For the Jakobshavn drainage basin these are given in figure 2.15. The scatter plots of other regions can be found in the appendix (A.10.2). The correlation parameters are calculated using the absolute elevation difference.

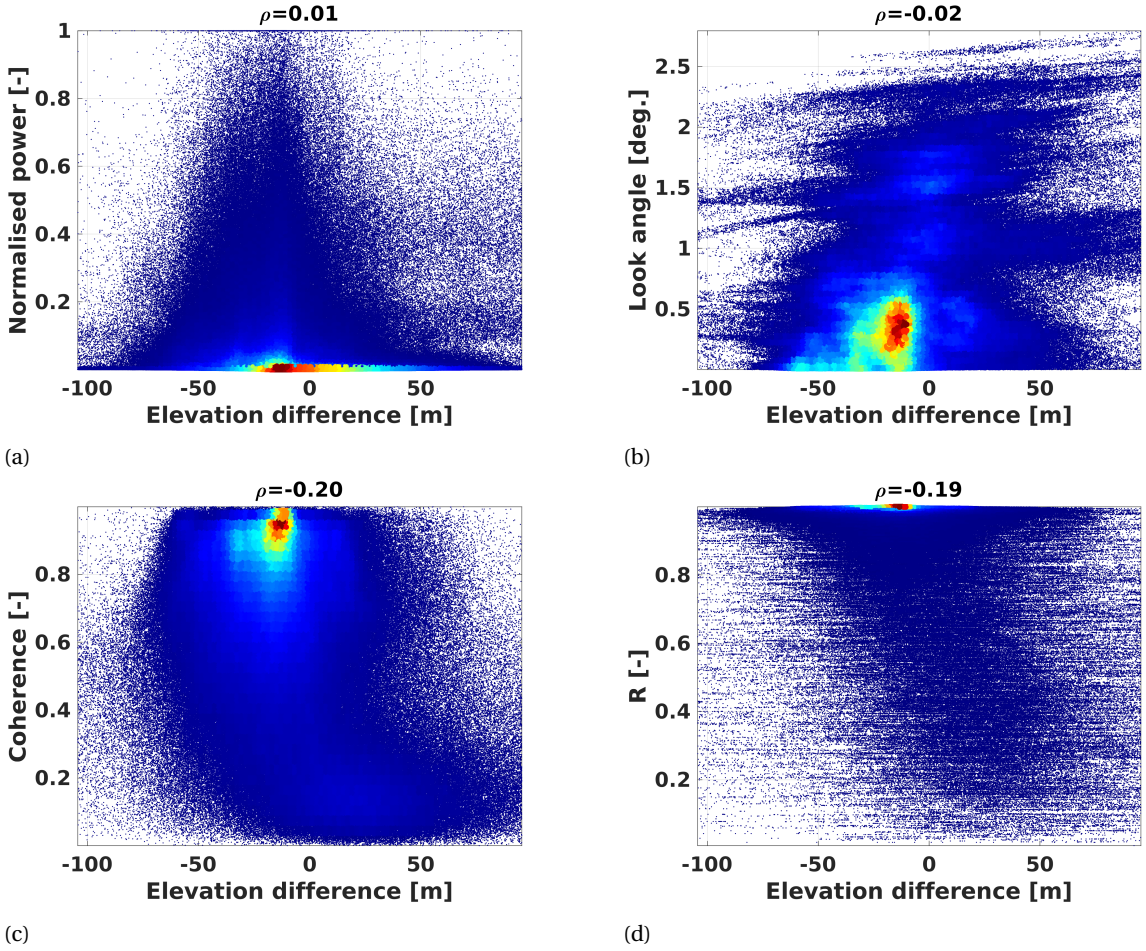

Figure 2.15: Scatter plot of (a) normalised power, (b) look angle, (c) coherence and (d) phase difference dispersion as a function of elevation error. Each sub figure contains the same number of points. The colour indicates relative point density (dark blue: low, dark red: high). PD dispersion refers to phase difference dispersion, the metric proposed by Weissgerber and Gourmelen [2017]. The correlation was calculated using the absolute elevation difference.

Figure 2.15a shows that increasing normalised power shows elevation estimates with less severe outliers. However, when discarding elevation estimates below 0.1 normalised power would immediately discard the majority (66%) of the elevation estimates. In case of drainage basin 1-2, 1-4, 4-2, 4-3 and 8-2, similar percentages arise, i.e. 80%, 80%, 75%, 61%, and 74%, respectively. Therefore, a threshold is not applied to normalised power as it drastically reduces the number of observations with a small elevation difference with the DEM.
In figure 2.15b the majority of estimates (72% of points) are concentrated below 1° look angle. This is similar for the other drainage basins: 1-2 (86%), 1-4 (92%), 4-2 (90%), 4-3 (80%) and 8-2 (88%). Furthermore, large deviations are visible for higher look angles. Therefore, it is decided that a threshold for look angle is investigated.
Figure 2.15c shows that a large part (39%) of estimates has a coherence >0.8. This is also the case for the other drainage basins: 1-2 (44%), 1-4 (51%), 4-2 (50%), 4-3 (51%) and 8-2 (44%). Furthermore, lower coherence shows an increasing elevation bias. Based on that, different coherence thresholds are attempted.
In figure 2.15d, 72% of the elevation estimates are concentrated at >0.9 PD dispersion. The other drainage basis show similar percentages: 1-2 (77), 1-4 (76%), 4-2 (75%), 4-3 (74%) and 8-2 (72%). Moreover, the remainder (<0.9) shows an increasing bias. The PD dispersion threshold is thus also varied.

PD dispersion is considered as a replacement for coherence. Therefore, look angle is varied against coherence first (figure 2.16), then look angle is varied against phase difference dispersion (figure 2.17). The same figures but for other drainage basins can be found in the appendix (A.10.3).

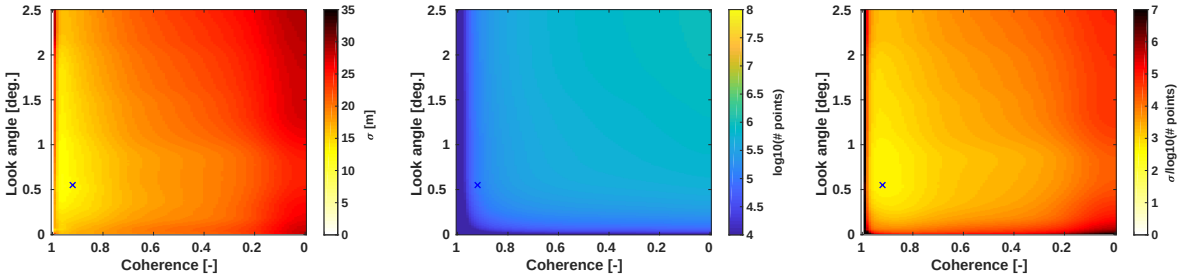

(a) Standard deviation of the elevation errors.

(b) Number of retracked points.

(c) Optimisation criterion.

Figure 2.16: Variation of coherence and look angle thresholds without a normalised power constraint.

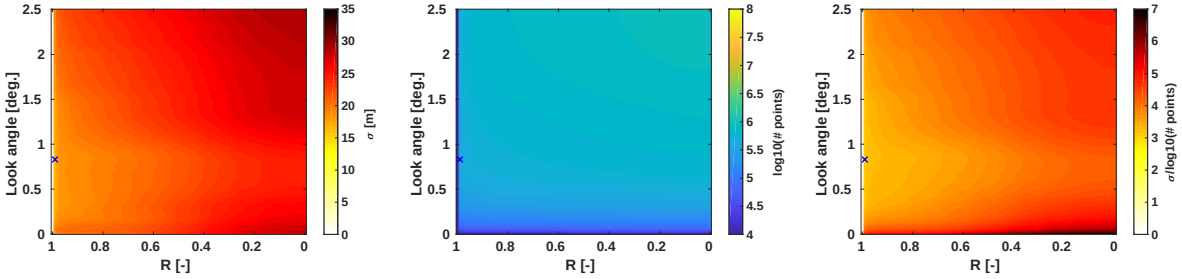

(a) Waveform sample PD dispersion versus look angle.

(b) Number of retracked points.

(c) Optimisation criterion.

Figure 2.17: Variation of phase difference (PD) dispersion and look angle thresholds without a normalised power constraint.

Two optima are found using $min(\frac{\sigma}{log_{10}N})$ for each of the drainage basins. One is based on the choice for coherence and one on phase difference dispersion. The look angle, coherence and PD dispersion are varied in steps of 0.01°, 0.01 and 0.01, respectively. The results are summarised in table 2.4 below.

Table 2.4: For each drainage basin, the minimum of $\frac{\sigma}{\log_{10}N}$ was found by varying coherence and look angle (γ) as well as PD dispersion (R) and look angle. σ is the standard deviation of the DEM elevation difference and N is the number of elevation estimates. σ-reduction indicates the reduction in standard deviation of elevation estimates when introducing the corresponding optimal thresholds.

Drainage basin	$\frac{\sigma}{\log_{10}N}$ [m]	σ [m]	$\log_{10}N$ [#]	**R** [-]	**Coherence** [-]	γ [°]	σ**-reduction** [%]
1.2	2.087	14.323	6.862	0.99	-	0.98	34
	2.111	14.493	6.865	-	0.76	0.98	33
1.4	1.103	7.228	6.553	0.99	-	0.99	67
	0.992	6.376	6.425	-	0.86	0.96	71
4.2	2.065	13.406	6.491	0.99	-	0.97	43
	2.096	13.721	6.546	-	0.67	1.00	41
4.3	3.339	21.164	6.339	0.97	-	1.04	29
	3.359	21.291	6.339	-	0.58	1.05	29
7.1	3.061	16.855	5.507	0.99	-	0.83	42
	2.618	13.090	5.000	-	0.92	0.55	55
8.2	2.731	17.926	6.563	0.99	-	0.93	38
	2.770	17.912	6.467	-	0.84	0.92	38

Based on table 2.4 and figure 2.16 and 2.17 it can be concluded that:

- Higher coherence and higher R reduce the number of points. However, based on the scatter plots, this takes place more gradually for coherence thresholds than for PD dispersion thresholds.
- Higher coherence does not necessarily provide more precise elevation estimates. This is in contrast to a higher R. This is better visible in section A.13 for other basins.
- Coherence and R perform similarly, because the optimisation value $\frac{\sigma}{\log_{10}N}$ differs marginally, except for the Jakobshavn drainage basin. In that case, the optimal threshold on coherence performs better.

The variation of optimal coherence threshold explains the choice for different coherence thresholds among the published studies in which CryoSat-2 data is exploited [Gourmelen et al., 2017, Gray et al., 2013, 2015, Hawley et al., 2009, Helm et al., 2014]. Furthermore, it also reveals that maintaining one coherence threshold for large surfaces, at least larger than drainage basins, leads to sub-optimal results. This is naturally also the case for one PD dispersion threshold, but to a far lesser extent. The coherence thresholds range from 0.58 up to 0.92, whereas PD dispersion thresholds vary from 0.97 to 0.99 on the same scale ([0,1]). The variation of optimum coherence shows that coherence also depends on factors that do not affect measurement quality. Its variation among different drainage basin suggests that topography is one. Based on that, a threshold on PD dispersion is advised for large observation areas, because this approach is far less sensitive to changing observation area. To that end, 0.99 is taken as threshold, giving preference to the number of points over quality of the elevation estimate.

DEM slope

The scatter plot (figure 2.18) below shows the distribution of slopes in terms of elevation differences.

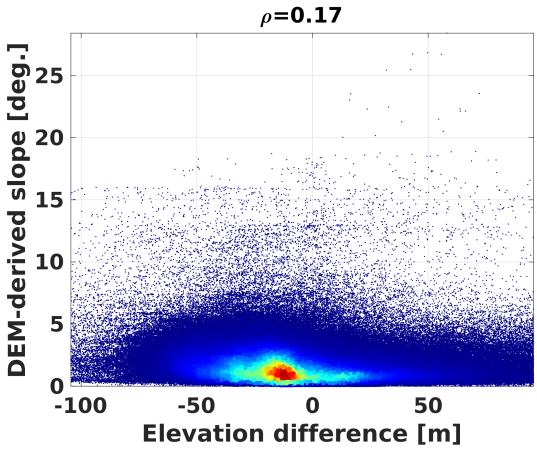

Figure 2.18: Scatter plot of DEM-derived slopes as a function of DEM elevation difference.

Figure 2.18 shows that most points (98%) are located on <5° slope. For the other drainage basins very high percentages were also obtained: 1-2 (99%), 1-4 (99%), 4-2 (99%), 4-3 (95%) and 8-2 (90%). Furthermore, it can be seen that the elevation difference does not particularly reduce for steeper slopes (see figure A.9). Therefore, at the risk of introducing a bias with only marginal improvement of the elevation estimates in terms of standard deviation, no threshold is applied to the DEM-derived slope.

Chosen retracking settings

The optimal parameters were chosen based on the optimisation criterion in all 6 drainage basins. The choices are summarised below in table 2.5.

Table 2.5: Chosen thresholds for retracking CryoSat-2 L1B data based on 6 drainage basins.

Parameter	Symbol [unit]	Value
Look angle	γ [°]	$\lvert\gamma\rvert \leq 0.96$
PD dispersion	R [-]	≥ 0.99
Normalised power	p [-]	> 0
Coherence	ψ [-]	$0 < \psi < 1$
Normalised waveform energy	E [-]	$35 < E < 135$
DEM slope	$\angle DEM$ [°]	≥ 0
DEM difference	ε_{elev} [m]	$\lvert\varepsilon_{elev}\rvert < 100$

A threshold to normalised power (>0) and coherence (<1) is, strictly spoken, applied. The thresholds in table 2.5 were applied and compared against OIB elevation estimates for April 2014 (see figure 2.9).

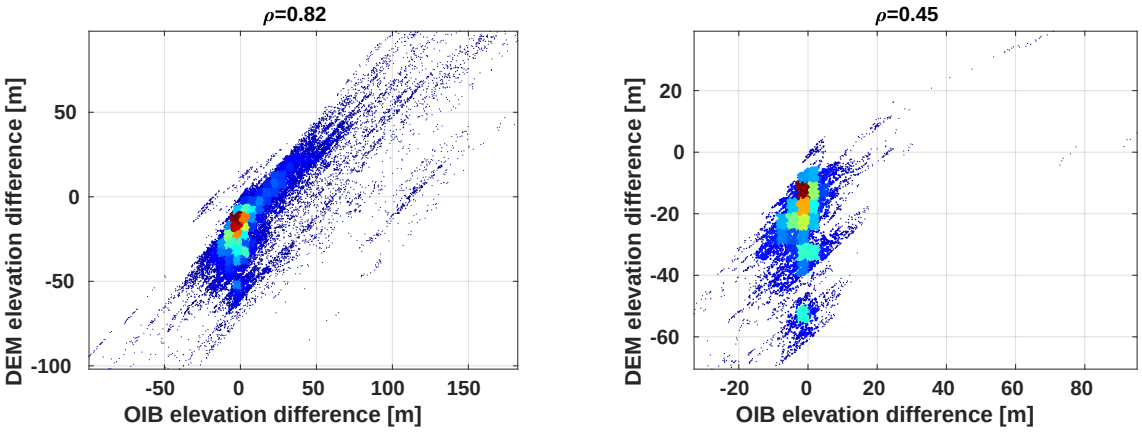

(a) Before applying thresholds.

(b) After applying thresholds.

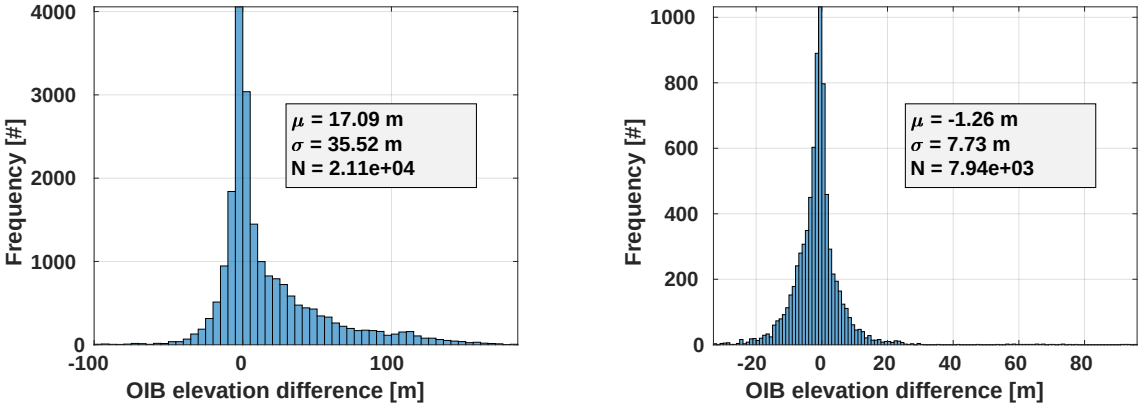

(c) Before applying thresholds.

(d) After applying thresholds.

Figure 2.19: Improvement of elevation statistics by comparison of the observations with OIB. The thresholds can be found in table 2.5. The application of chosen thresholds reduced the standard deviation by more than 25 m. Note that the figures have different scales. Figure 2.19a and 2.19c are the same as figure 2.9a and 2.9b, respectively.

Before the application of the thresholds from table 2.5, the mean and standard deviation of elevation differences in the Jakobshavn drainage basin are 17.09 m and 35.52 m, respectively. After the application of the thresholds from table 2.5, the mean and standard deviation of elevation differences in the Jakobshavn drainage basin are -1.26 m and 7.73 m, respectively. In both cases, before and after a comparison between

DEM elevation difference and OIB elevation difference could be made for about 3% of the total number of elevation estimates. The total number of elevation estimates dropped from 957459 to 393485, retaining about 41% of the elevation estimates. 98% (w.r.t. 62% before threshold application) of the points are within 15 metres OIB elevation difference.

On average, the airborne elevations are lying above the CryoSat-2 elevations. The mean value of -1.26 m in figure 2.19c is slightly biased (by +0.25 m) towards a higher mean due to outliers above 50 m OIB elevation difference. The overall negative offset is likely caused by radar penetration into the snow pack [Gourmelen et al., 2017]. The bias is assumed to be of minor impact for multi-year trend analysis, because the bias signal is of seasonal nature. Moreover, WLSE includes seasonal components.
The outliers above 50 m OIB elevation difference originate from near the (SIN-LRM) mode boundary. During processing, anomalous outliers were found near the mode boundary. Therefore, measures were taken to discard these. Some of these outliers however, still remain. The poor quality CryoSat-2 recordings near the SIN-LRM mode boundary and limited observations in the LRM zone within the same area are not well documented. It was also found that the SIN-LRM mode boundary was shifted about 3 km towards the coast from October 2012 until July 2014 after which it is placed in its old position again. Maps showing the locations of the elevation differences (between our computed elevation and the OIB elevation) that were used to compute the histograms (figure 2.19) are provided in figure 2.20.

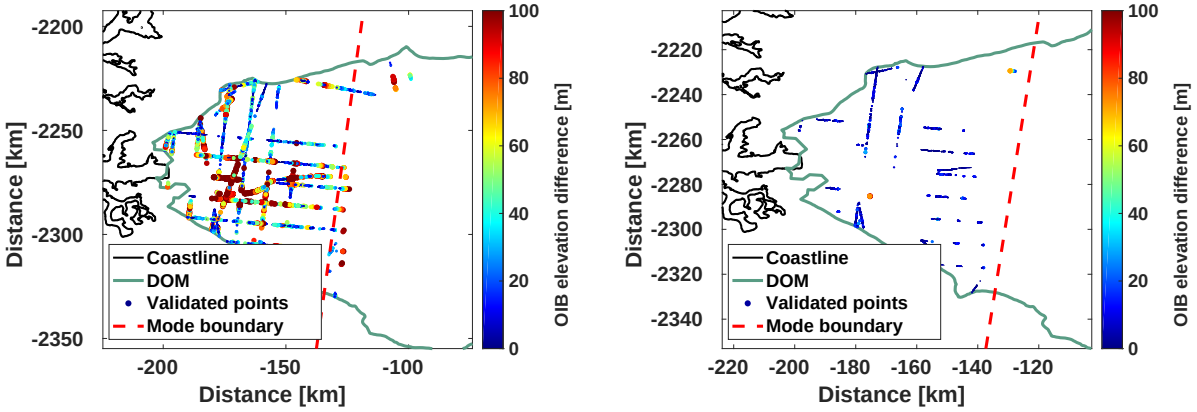

(a) No specific settings applied.

(b) Optimised settings applied.

Figure 2.20: Locations of points validated with OIB. Note the large errors near the terminus and near the mode boundary. Note that this figure does not indicate the actual coverage. Only about 3% of the elevation estimates made in April 2014 could be compared with OIB data. *DOM* refers to domain, i.e. the Jakobshavn drainage basin.

Notice that the elevation estimates near the terminus are often poorly resolved and are discarded using the set of thresholds displayed in table 2.5. The retained estimates demarcate the calving front, which is better visible in figure 2.21 in the next section.

2.4.2. Swath processing results

The spatial coverage of elevation estimates and elevation change estimates are illustrated in figure 2.21. As discussed in section 2.3.3, an elevation change estimate is attempted for every elevation estimate. Naturally, there are less elevation change estimates than elevation estimates per grid cell, due to the introduced conditions when attempting a WLSE.

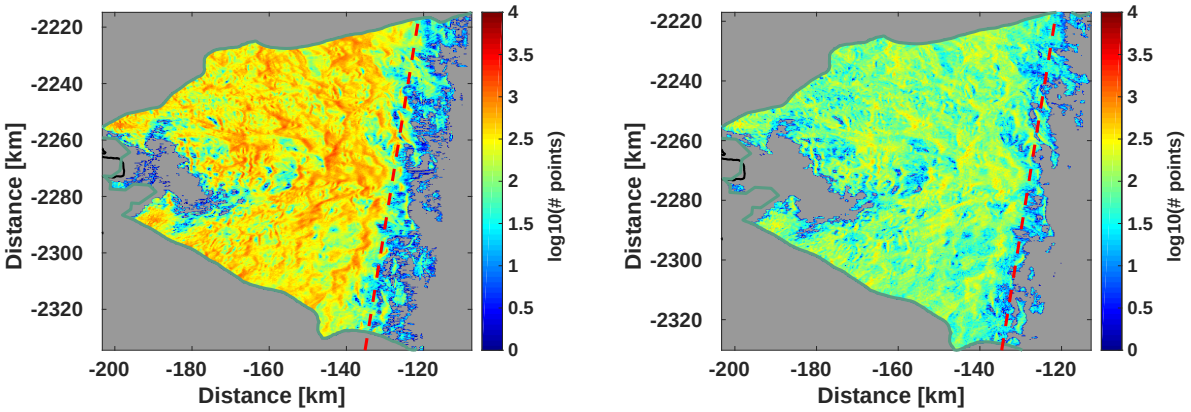

(a) Elevation estimates per grid cell.

(b) Elevation change estimates per grid cell.

Figure 2.21: Number of data points per grid cell of 250 × 250 m^2 (November 2010 until March 2016).

Figure 2.21a shows roughly on average $10^{2.20}$ (160) elevation estimates per grid cell. In case of POCA processing this number will thus be, on average, 160 times lower. Therefore, it can be concluded that elevation changes estimates with this grid cell size is not feasible using POCA processing. Figure 2.21 shows an average of $10^{1.85}$ (71) elevation change estimates per grid cell. The average was taken over the entire ensemble of elevation estimates within the Jakobshavn drainage basin, i.e. also just outside the SIN mode zone (in the LRM zone). Only estimates with at least 1 elevation (change) estimate are included to calculate the average. Part of the area is not covered by valid elevation (change) estimates at all. These estimates originate from before the calving front (see figure 1.2 with calving front demarcations) and are not desired.

2.4.3. Elevation change estimate

The elevation change estimates in figure 2.21b are averaged to obtain one estimate per grid cell (see figure 2.22 below) in the lower elevated region of the Jakobshavn drainage basin. The glacial isostatic adjustment (GIA) is not subtracted from the elevation estimates as models show that this lies around approximately 0 mm/yr in the Jakobshavn drainage basin [Wake et al., 2016]. A basin-wide error of 1 mm/yr leads to a 0.09 Gt/yr bias in the mass change estimate of the Jakobshavn drainage basin when assuming the density of ice.

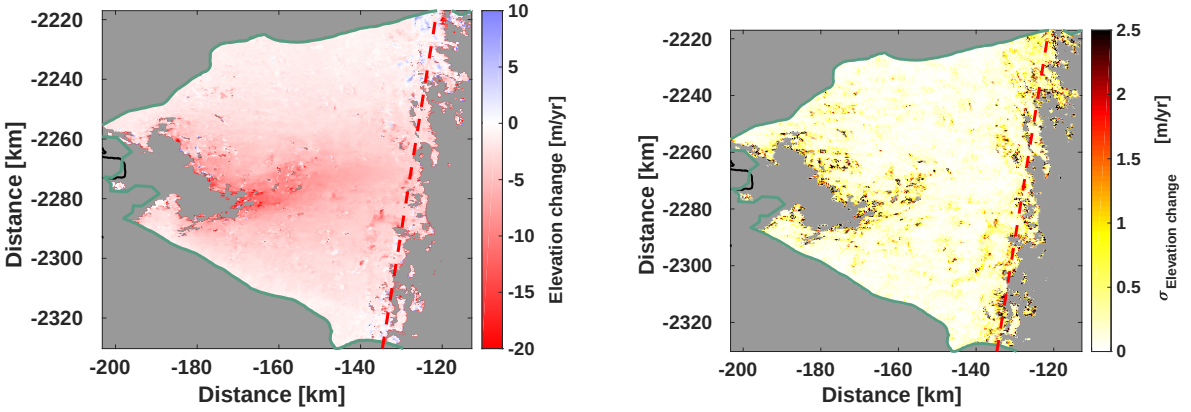

(a) Elevation change in m/yr.

(b) Elevation change standard deviation in m/yr.

Figure 2.22: Elevation change and elevation change standard deviation in m/yr. Estimation period is November 2010 until March 2016. The elevation change estimates are limited to the area of the Jakobshavn drainage basin that is observed in SIN mode.

Figure 2.22 shows an overall signal of thinning, with increasing thinning rates towards the glacier terminus. The particular locations where rapid thinning takes place correspond well with the channels where rapid ice velocities are observed (see figure A.19 in the appendix). Furthermore, the standard deviation of the rates are high 1) near the LRM-SIN boundary and 2) near the calving front. These regions correspond well with the

areas with low numbers of elevation change estimates (figure 2.21b).

The largest part of the drainage basin, more inland, is near balance, as visualised in figure 2.23. The region in the east of the basin area experiences thickening in the order of cm/yr, in contrast to thinning rates near the terminus which reach thinning rates over 15 m/yr.

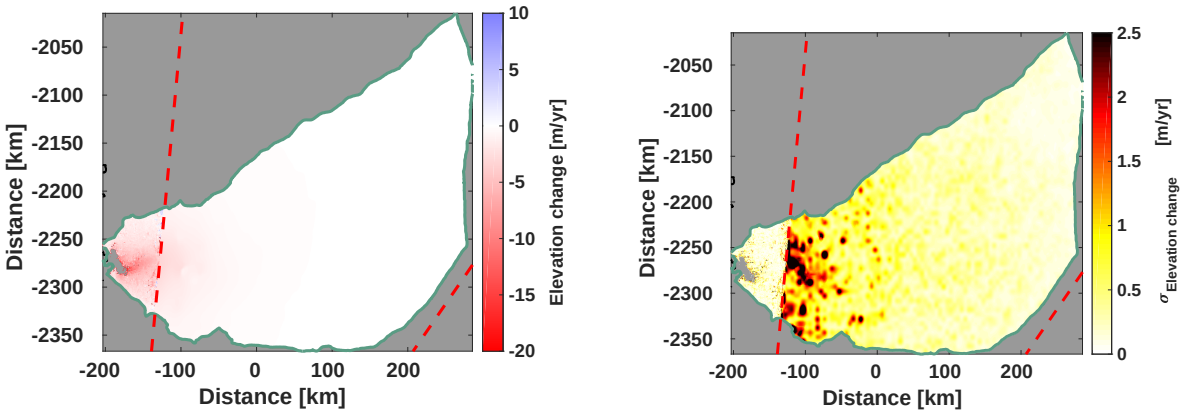

(a) Elevation change in m/yr.

(b) Elevation change standard deviation in m/yr.

Figure 2.23: a) Elevation change in m/yr. b) Elevation change standard deviation in m/yr. Estimation period is November 2010 until March 2016. The SIN mode elevation change rates are the same as in figure 2.22. The LRM elevation changes and corresponding errors were taken from Gourmelen et al. [2017].

The large standard deviations in figure 2.23b in the added data near the mode boundary is due to very limited coverage (i.e. few observations). This has a seemingly large effect on LRM data, because no swath processing is possible here. However, it is expected that the spatial variety of elevation changes is small (little ice dynamics). The LRM area (89703 km^2) is nearly 16 times larger than the SIN mode area (5677 km^2). The total area is 95380 km^2.

2.4.4. Volume change estimate

Data selection takes place before attempting hypsometric averaging. Elevation change estimates with a standard deviation larger than 0.5 m/yr (or no elevation change estimate at all) are discarded and not used for fitting. This step discards about 20% elevation change estimates, nearly all (>95%) of which originate from the LRM zone (see figure 2.23b). These mostly originate from around 1700 m elevation (figure 2.24). About 0.5% of all grid cells has no elevation change estimate, these are interpolated using hypsometric averaging.

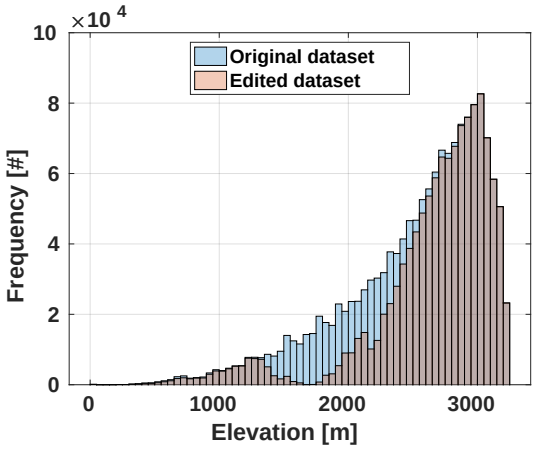

Figure 2.24: Histogram of the input and data edited elevation change estimates. About 20% of the estimates exceed a standard deviation of 0.5 m/yr and are discarded.

Importantly, there are virtually no estimates available below 500 m elevation. Following Moholdt et al. [2010], 2^{nd}, 3^{rd}, 4^{th} order polynomial, mean and median fits are made.

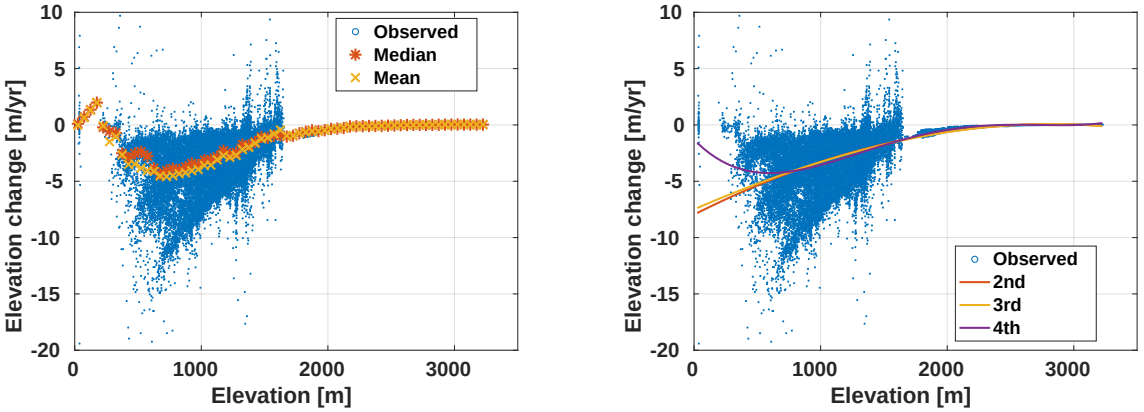

(a) Median and mean approach for hypsometric averaging. These estimates are likely biased towards lower volume estimates.

(b) Polynomial approach for hypsometric averaging. These estimates are likely biased towards higher volume estimates.

Figure 2.25: Hypsometric averaging using different hypsometric fits.

All fits follow the trend above 1800 m elevation fairly well. In figure 2.25a, mean and median fits are particularly susceptible to the relatively limited number of points around 1700 m elevation. This effect is most clearly visible for the mean fit (figure 2.25a). For elevations between 700 to 1700 m, the median fit shows higher elevation estimates than the mean fit. The median fit is biased towards the elevation change rates of which there are most observations.
The polynomial fits (figure 2.25b) are naturally smoother and show a significantly different behaviour below 700 m elevation. The 2^{nd} and 3^{rd} order polynomials better represent the expected global behaviour, whereas the 4^{th} order is more similar to the mean and median fits. However, the 2^{nd} and 3^{rd} order polynomial fits may be biased towards higher volume losses, as it assumes high thinning rates for regions farther from the outlet at common elevations.
To conclude, the 2^{nd} and 3^{rd} order polynomial fits are biased towards higher volume losses and the mean and median fits towards lower volume losses. The 4^{th} order polynomial fit is expected to lie somewhere in between. The volume change and error estimates corresponding to the aforementioned approaches can be found in table 2.6. From figure 2.24 and figure 2.25 the following can be concluded:

- The most elevated (>1800 m) areas are very smooth and show little to no elevation change. All this data originates from CryoTop [Gourmelen et al., 2017].
- The lower elevated LRM field, 1600-1900 m elevation, is poorly sampled due to limited, precise LRM data in this region. Also there are outliers present within this region after data selection.
- The lower elevated SIN field reveals 2 regimes: one rapidly subsiding regime deviating from the global trend (500-700 m) and one slightly stabilising.

To resolve the choice between two possible thinning regimes in the SIN field, two hypsometric curves can be introduced. One for the rapidly discharging region close to the outlet and one for the less dynamic regions.

Table 2.6: Hypsometric averaging results for different fits.

Method	$\frac{dV}{dt}$ **[km^3/yr]**	E_V **[km^3/yr]**
Mean	-26.74	2.94
Median	-24.89	3.66
2^{nd} order polynomial	-34.06	3.65
3^{rd} order polynomial	-34.34	3.68
4^{th} order polynomial	-30.59	3.30

Deciding on which region is highly dynamic and which region is not, is not trivial. Ice velocity maps provide an outcome here, such as the one created by Nagler et al. [2015] (see figure A.19), which is also used in the second density model. This ice velocity map has been derived from Sentinel-1 SAR data over the period 01-10-2015 to 31-10-2016. A small part (0.2%) of the Jakobshavn drainage basin has however, no valid velocity. All grid cells without a valid velocity originate from the area where the floating tongue used to be, i.e. in front of the calving front. Therefore, the elevation change is set to 0.

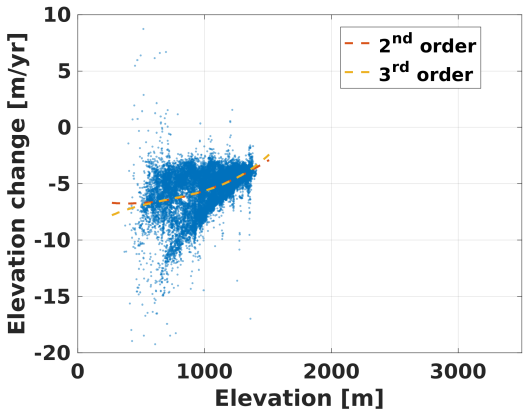

(a) 2^{nd} and 3^{rd} order polynomial fit to all flow velocities equal to or above 500 m/yr.

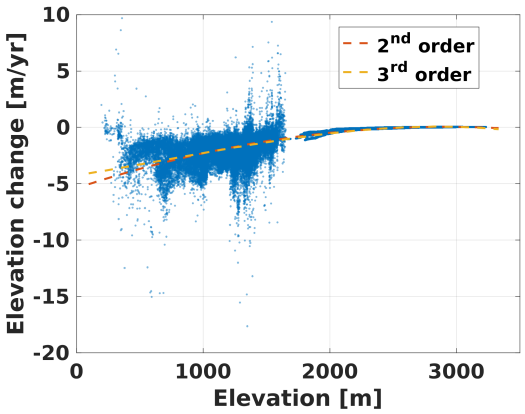

(b) 2^{nd} and 3^{rd} order polynomial fit to all flow velocities below 500 m/yr.

Figure 2.26: Separation of thinning regimes based on flow velocity.

The 2^{nd} and 3^{rd} order polynomial are considered as adequate volume change fit for both velocity regimes, because it resembles the expected physical behaviour. The results of the two hypsometric fits are summarised in table 2.7 below.

Table 2.7: Volume change derived from two hypsometric curves.

Method	$\frac{dV}{dt}$ [km^3/yr]	Area [km^2]	E_V [km^3/yr]
2^{rd} order polynomial (<500 m/yr)	-19.99	93460	2.11
2^{rd} order polynomial (≥500 m/yr)	-9.55	1727	1.18
No velocity available	0	193	-
Total	-29.42	95380	3.11
3^{rd} order polynomial (<500 m/yr)	-20.87	93460	2.19
3^{rd} order polynomial (≥500 m/yr)	-9.60	1727	1.19
No velocity available	0	193	-
Total	-30.47	95380	3.20

Remarkable is that less than 2% of the total drainage basin is responsible for nearly one third of the total mass loss. The result is most sensitive to fits in the high flow velocity (>=500m/yr) region. In contrast to the 3^{rd} order polynomial, the 2^{nd} order polynomial indicates smaller elevation changes as the elevation drops (figure 2.26a). The 3^{rd} order polynomial estimates for figure 2.26a and 2.26b show 0.88 and 0.05 km^3/yr stronger volume loss, respectively. Nevertheless, the results are similar and within error bar. Furthermore, direct integration of all volume changes using hypsometric averaging only for the missing cells instead leads to estimates that are similar (difference in the order of 0.1 km^3/yr).
The estimated volume changes corresponds well with the integrated CryoTop [Gourmelen et al., 2017] maps, i.e. -28.9 km/yr. The 1-σ error bound from the derived estimate alone overlaps this estimate.

2.4.5. Mass change estimate

Direct conversion of the volume changes obtained with a 2^{nd} and 3^{rd} order polynomial to mass changes using the density of ice results in a mass change of -27.0±2.9 Gt/yr and 27.9±2.9 Gt/yr, respectively. Table 2.8

shows the mass change results when accounting for mixed medium in the volume changes using a linear density model and flow velocity based density model. An example of each one of the used linear and flow velocity based density models are shown below.

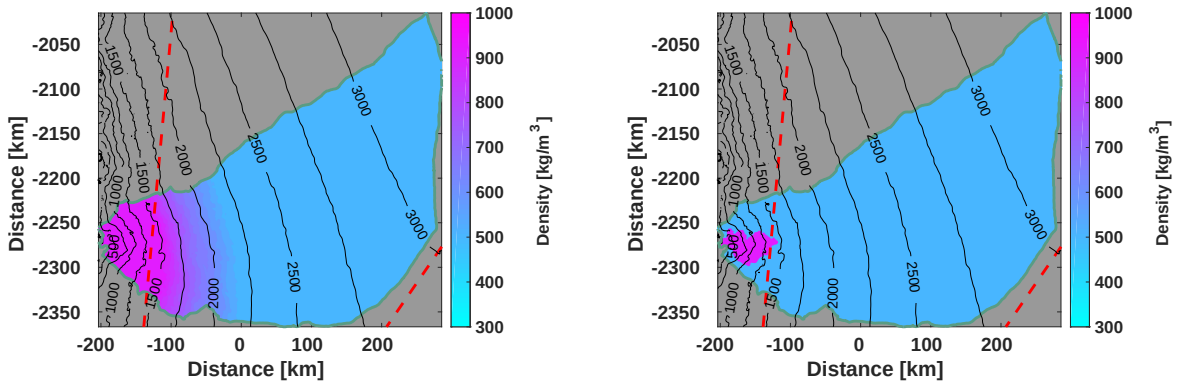

(a) Linear density models with ρ_{firn} = 500 kg/m^3 and ELA is at 1500 m elevation.

(b) Flow velocity based density models with ρ_{firn} = 500 kg/m^3 and flow boundary at 500 m/yr.

Figure 2.27: Example of density models used for volume to mass conversion. The contour lines indicate elevation in metres. The dashed red line indicates the mode boundary.

The FDM (see section A.10.3.5) shows a basin wide negative linear trend, which gives confidence that the effective densities do not exceed the density of ice. Table 2.8 shows the results of volume to mass conversion, where E_M is the mass change error. E_M consists of the RSS of σ_{conv} and E_V, assuming the density of ice. Thereby, the latter component can be considered as conservative.

Table 2.8: Mass change based on a linear and flow velocity based density model. Estimate A and B are based on the volume estimate made using a 2^{nd} and 3^{nd} order polynomial, respectively.

Density model	$\frac{dM}{dt}$ **[Gt/yr]**	σ_{conv} **[Gt/yr]**	E_M **[Gt/yr]**
Linear density model (A)	-24.72	0.89	2.99
Flow velocity based density model (A)	-19.98	3.50	4.52
Linear density model (B)	-25.45	0.95	3.32
Flow velocity based density model (B)	-20.56	3.67	4.64

The flow velocity based density model has a relatively high conversion error. This is because no density gradient is considered here (see figure 2.27b). Furthermore, the difference of about 5 Gt/yr and relatively large conversion error is caused by the non-linear flow velocity change when moving away from the terminus. Therefore, linear variation of velocity thresholds likely biased the result towards lower mass changes. The linear density model however, is assumed to be more realistic as it includes a varying transition zone. The change from a dynamic region where ablation is dominant to a region where short term variability is more dominant is after all not abrupt. To conclude, the linear density model (A) also has the smallest standard deviation (among linear density model A and B) and is considered as adequate.

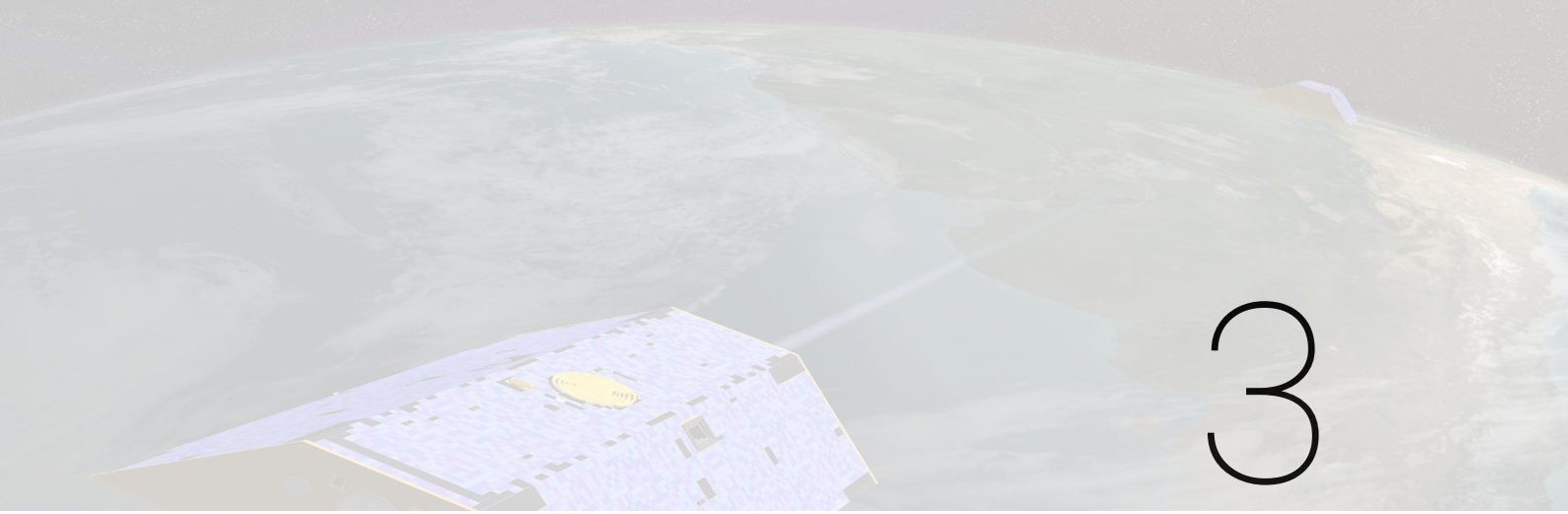

3

Mass change through gravimetry

This chapter presents the reader with a brief introduction on the GRACE twin satellite mission, its measurement principles and theory for conversion of GRACE observations to mass change. This is followed by the applied methodology to infer a mass change estimate from a GRACE L2 data product using a point mass assumption. Finally, the observed mass changes are presented and discussed.

3.1. Introduction: GRACE twin satellites

The GRACE mission is engaged with gravity (field) variations employing two satellites at roughly 220 km distance along the orbital track (near polar orbit) each at an altitude of about 500 km (LEO). Both NASA and DLR funded the mission. The twin satellite mission was in orbit from the 17^{th} of March 2002 until October 2017. We refer to Wouters et al. [2014] for a comprehensive overview of the GRACE mission applications.

3.1.1. Measurement principle

The GRACE satellite mission observes the Earth's gravitational field by monitoring the distance between the two satellites. The measurement principle is as follows: The distance between the two satellites varies in the vicinity of gravity anomalies mainly located near or at the Earth's surface. Positive gravity anomalies such as mountain ranges or ice sheets lightly pull the first twin satellite forwards. Therefore, the distance between the satellites slightly increases. The same event however delayed, takes place for the second twin satellite as it approaches the same positive gravity anomaly. Further on, the first twin satellite is slightly pulled backwards after passing the gravity anomaly. Concretely, these changes in distance can be measured down to the order of 10 micrometers [Tapley and Bettadpur, 2004]. These minuscule changes in distance between the twin satellites are accurately and precisely monitored using K-band (microwave) ranging (KBR) system [Tapley and Bettadpur, 2004]. The distance variation is thus a measure of the encountered mass anomaly. Repeated observations then describe the change of the gravitational field. This enables users to separate (near) static anomalies such as the mountain ranges from time-varying anomalies such as ice losses in polar areas.

3.1.2. GRACE in context of study area

The maximum spherical harmonic degree gives an indication of the spatial resolution of GRACE monthly solutions (approximately 150 km at 70° N for maximum degree 90). Multiple small-scale mass redistributions within an area of 150 by 150 km are impossible to differentiate with GRACE monthly solutions. Therefore, it is essential to assess Jakobshavn's surroundings in terms of mass change.
The Jakobshavn drainage basin is roughly 500 km and 350 km in its East-West and North-South direction, respectively. In chapter 2, the strongest mass loss signal was identified near the coast. According to figure 3.1a, the signal is dominant even in a wide area around the Jakobshavn drainage basin. Figure 3.1a is created taken CryoTop (from CryoSat data) maps [Foresta et al., 2018]. A signal of of thinning originating from another glacier can be found in the vicinity of the Jakobshavn glacier at roughly 90 km distance (-2200 km;-200 km EPSG3413). That signal coincides with the Sermeq Kujatdleq glacier. The Sermeq Kujatdleq glacier is wider than the Jakobshavn glacier and also discharges at relatively high rates (>1 km/yr) [Moon et al., 2014, Nagler et al., 2015, Rignot and Mouginot, 2012]. This can also be found in figure 3.1b [Nagler et al., 2015]. In order to adequately isolate the signal from the Jakobshavn glacier, it is desired that the contribution of the Ser-

meq Kujatdleq glacier in terms of mass variations is accounted for. Based on figure 3.1a it is expected that the contribution of the Sermeq Kujatdleq glacier is much smaller than the contribution of the Jakobshavn glacier.

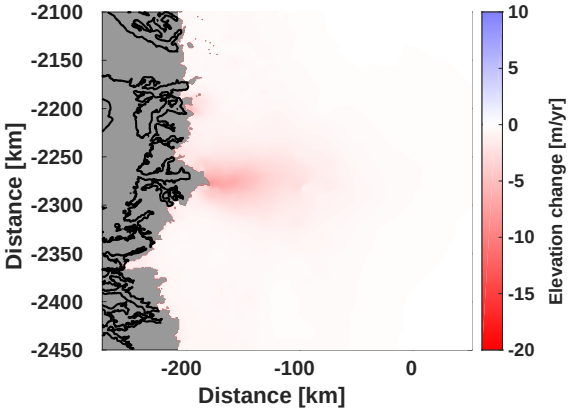

(a) Elevation change (1 km resolution). *Data from CryoTop (CryoSat-2 mission) [Gourmelen et al., 2017].*

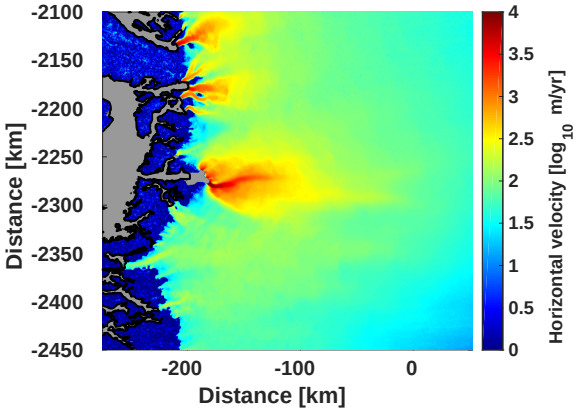

(b) Annual horizontal flow velocity map (0.5 km resolution). *ESA Greenland Ice Sheet product based on Sentinel-1 data (01-10-2015 to 31-10-2016) [version 1.2], [Nagler et al., 2015].*

Figure 3.1: Rates of mass change or mass change-related processes in the area of the Jakobshavn drainage basin.

3.2. Theory

GRACE level 2 data products are commonly provided in the form of *Stokes' coefficients* on a monthly basis. Each monthly set of Stokes' coefficients (*GRACE monthly solution*) represents the monthly average Earth's gravitational potential. By subtracting the long-term mean per Stokes' coefficients, it is possible to create a time series of the temporal variations of the gravitational potential (equation 3.1, [Heiskanen and Moritz, 1993]):

$$\Delta V(r,\theta,\phi,t) = \frac{GM_E}{a}\sum_{l=0}^{\infty}\left(\frac{a}{r}\right)^{l+1}\sum_{m=-l}^{l}\Delta\bar{C}_{l,m}(t)\bar{P}_{l,m}(\cos\theta)\begin{cases}\cos m\phi & ,\ m\geq 0\\ \sin|m|\phi & ,\ m<0,\end{cases} \tag{3.1}$$

where $\Delta V(r,\theta,\phi,t)$ is the temporal variation of the gravitational potential as a function of spherical coordinates (radial distance, co-latitude and longitude, respectively), G the universal gravitational constant, M_E the mass of the Earth, a the semi-major axis of the reference ellipsoid (section A.8), l the degree, m the order, $\Delta\bar{C}_{l,m}(t)$ the temporal variations of the Stokes' coefficients with zero mean and $\bar{P}_{l,m}(\cos\theta)$ the *4π-normalised associated Legendre function* as a function of the cosine of the co-latitude. Equation 3.1 represents an example of *spherical harmonic synthesis*, i.e. the computation of a function from the Stokes' coefficients. The synthesis in equation 3.1 is in practice not completed and becomes an approximation, because the summation is bounded by a maximum spherical harmonic degree (L_{max}) and not by infinity. For the GRACE data products the Stokes' coefficients commonly have a maximum spherical harmonic degree of around 60, 90 or 120. Truncation of the series affects the spatial resolution of $\Delta V(r,\theta,\phi,t)$. To illustrate: synthesis up to spherical harmonic degree 60, 90 and 120 result in a spatial resolution of approximately 670, 450 and 330 km near the equator, respectively. For Jakobshavn, this is approximately 230, 150 and 110 km, respectively.
Equation 3.1 can be rewritten to:

$$\Delta V(r,\theta,\phi,t) = \frac{GM_E}{a}\sum_{l=0}^{L_{max}}\left(\frac{a}{r}\right)^{l+1}\sum_{m=-l}^{l}\Delta\bar{C}_{l,m}(t)\bar{Y}_{l,m}(\theta,\phi), \tag{3.2}$$

where $\bar{Y}_{l,m}(\theta,\phi)$ combines the associated Legendre function and its order-dependent factor as in [Ditmar, 2018b]:

$$\bar{Y}_{l,m}(\theta,\phi) = \bar{P}_{l,|m|}(\cos\theta)\begin{cases}\cos m\phi & ,\ m\geq 0\\ \sin|m|\phi & ,\ m<0.\end{cases} \tag{3.3}$$

$\bar{Y}_{l,m}$ are called *4π-normalised surface spherical harmonics*. The normalised associated Legendre function are computed using a recursive scheme from Holmes and Featherstone [2002]. For more information on spherical harmonic synthesis please refer to section A.9, Heiskanen and Moritz [1993], and Ditmar [2018a].

3.2.1. Degree-1 and $C_{2,0}$ coefficients

The zeroth spherical harmonic degree and order Stokes' coefficient $\delta\bar{C}_{0,0}$, represents the total mass variation of the Earth, which is zero. $\delta\bar{C}_{1,m}$ (degree-1) and $\delta\bar{C}_{2,0}$ represent the geocentre displacement [Ray, 1999] and variations of the dynamic oblateness of the Earth [Sun et al., 2016], respectively. Absent degree 1 Stokes' coefficients can directly introduce a bias to mass variation estimates at the scale of half the Earth. Wu et al. [2012] found that 1 mm offset in the z-component of the geocentre equals an 11 Gt bias over Greenland. To that end, the degree-1 and $C_{2,0}$ Stokes' coefficients from Sun et al. [2016] were taken, which were more accurately estimated than those present in the GRACE monthly solutions. The more accurate degree-1 and $C_{2,0}$ Stokes' coefficients are inferred from a combination of GRACE observations as well as GIA and an ocean bottom pressure model [Sun et al., 2016]. These are used to include the degree-1 and replace the regular GRACE $C_{2,0}$ Stokes' coefficients.

3.2.2. Conversion of temporal variations of gravitational potential

Mass variations at the Earth's surface are obtained in the spectral domain by applying a scaling factor to the Stokes' coefficients. The $\frac{GM}{a}$ and $\left(\frac{a}{r}\right)^{l+1}$ terms from equation 3.1 are adjusted to 1) convert gravitational potential to surface density variations and 2) fit to the dimensions of the Earth more adequately via:

$$\bar{C}^{(\delta s)}_{l,m} = \frac{M_E}{4\pi a^2}\frac{(2l+1)}{(1+k'_l)}\Big(\frac{a}{\tilde{R}(\theta)}\Big)^{l+2}\Delta\bar{C}_{l,m}, \tag{3.4}$$

where $\bar{C}^{(\delta s)}_{l,m}$ are Fourier coefficients for surface density variations (δs) and k'_l the load Love number for spherical harmonic degree l. The load Love numbers account for deformation of the solid Earth due to loading [Wahr et al., 1998]. $\tilde{R}(\theta)$ is a geocentric, co-latitude (section A.8) dependent, geocentric radius assuming the dimensions of the reference ellipsoid [Ditmar, 2018b]:

$$\tilde{R}(\theta) = \frac{a(1-f)}{\sqrt{1-e^2\sin^2\theta}}, \tag{3.5}$$

where f is the ellipsoid flattening and e its eccentricity. Ditmar [2018b] found that adjusting the term for the Earth's radius using $\tilde{R}$ is more (up to 15% or more) accurate than assuming a sphere of radius a; especially 1) at high latitudes, 2) in case of large mass variations at small spatial scales and 3) when considering long time intervals. Regarding these three points, this implementation is especially relevant for the Jakobshavn drainage basin.

The final equation relating time-varying Stokes' coefficients from the GRACE data product to surface density variations is therefore:

$$\delta s(\theta,\phi,t) = \frac{M_E}{4\pi a^2}\sum_{l=1}^{L_{max}}\frac{(2l+1)}{(1+k'_l)}\Big(\frac{\sqrt{1-e^2\sin^2\theta}}{1-f}\Big)^{l+2}\sum_{m=-l}^{l}\Delta\bar{C}_{l,m}(t)\bar{Y}_{l,m}(\theta,\phi). \tag{3.6}$$

3.3. Data processing methodology

Due to relatively limited resolution, direct integration of each grid cell does not provide accurate mass change estimates in our case. This is because the dimensions of observation area are of the same order as a GRACE resolution cell (for maximum spherical harmonic degree 90 or 96). The observation points are correlated spatially and are thus not point measurements [Wouters et al., 2014]. Therefore, an alternative approach is chosen to obtain mass change estimates within the Jakobshavn drainage basin. In essence, mass change is simulated using one or more point masses. These are converted to Stokes' coefficients and surface density variations. Then the known modelled surface density variation is said to be an unknown number of times the observed surface density variation.

To that end, modelling of a point mass and converting it to Stokes' coefficients and surface density variation is demonstrated in section 3.3.1. Choice of number of point masses and point mass location is discussed in section 3.3.1.1. The grid set-up at which scaling of the point mass to the observations takes place is discussed in section 3.3.1.2. Estimation of the unknown scaling factor to scale the point mass to observations is discussed in section 3.3.2.

3.3.1. Introducing a point mass

Combining equations 3.4 and 3.6 leads to [Ditmar, 2018a]:

$$\delta s(\theta,\phi,t) = \sum_{l=1}^{L_{max}} \sum_{l=-m}^{m} \bar{C}_{l,m}^{(\delta s)}(t)\, \bar{Y}_{l,m}(\theta,\phi). \tag{3.7}$$

Division of the surface density variations by the density of water (10^3 kg/m^3) results in equivalent water height (EWH) variations in metres. The Fourier coefficients for surface density variation can be computed by integrating the surface density variation times the normalised surface spherical harmonics over surface area S:

$$\bar{C}_{l,m}^{(\delta s)}(t) = \frac{1}{4\pi \tilde{R}^2(\theta)} \iint_S \delta s(\theta,\phi,t)\, \bar{Y}_{l,m}(\theta,\phi)\, \tilde{R}^2(\theta)\, dS, \tag{3.8}$$

where $\tilde{R}^2(\theta)$ scales the surface element of a unit sphere to that of to the Earth's reference ellipsoid. Additionally, $\frac{1}{4\pi\tilde{R}^2(\theta)}$ is used to maintain 4π-normalisation. By assuming a point mass (at (θ_0,ϕ_0)) in the region responsible for the entire signal in the region, equation 3.8 reduces to:

$$\begin{aligned} \bar{C}_{l,m}^{(\delta s)} &= \frac{1}{4\pi \tilde{R}^2(\theta)} \iint_S \delta(\theta-\theta_0,\phi-\phi_0) M_I \bar{Y}_{l,m}(\theta,\phi)\, dS \\ &= \frac{M_I}{4\pi \tilde{R}^2(\theta)}\, \bar{Y}_{l,m}(\theta_0,\phi_0), \end{aligned} \tag{3.9}$$

where $\delta(\theta-\theta_0,\phi-\phi_0)$ is the *Dirac delta function*, which is infinite at (θ_0,ϕ_0) and 0 elsewhere and M_I is 10^{12} kg (equals 1 Gt). As a consequence, the Fourier coefficients now represent a point surface density variation. Substituting equation 3.9 into 3.7 leads to:

$$\delta s_{pm}(\theta_c,\phi) = \frac{M_I}{4\pi \tilde{R}^2(\theta_c)} \sum_{l=1}^{L_{max}} \sum_{l=-m}^{m} \bar{Y}_{l,m}(\theta_c,\phi)\, \bar{Y}_{l,m}(\theta_0,\phi_0). \tag{3.10}$$

Notice that $\delta s_{pm}(\theta_c,\phi)$ is time-independent. A 1-D Fourier transform of a delta-function results in a sinc-function when the summation truncated (spectrally limited). Analogous to a 1-D Fourier transform, equation 3.10 results in a 2D sinc-function on a sphere. In short, equation 3.10 maps a point mass of magnitude M_I at (θ_0,ϕ_0) on sphere with radius $\tilde{R}^2(\theta_c)$ onto grid points (θ_c,ϕ). δs_{pm} is not zero when it does not coincide with (θ_0,ϕ_0) due to the fact that the summation is truncated.

Position of the point mass(es)

The surface density variation is computed in the region of the Jakobshavn drainage basin at 5 km resolution in figure 3.2. The Jakobshavn mass loss is well visible in figure 3.2. On the other hand, a relatively weak signal of mass accumulation is observed in the eastern area of the drainage basin. This may be a Gibbs phenomenon caused by the strong and local mass change signal nearby (of the Jakobshavn glacier).

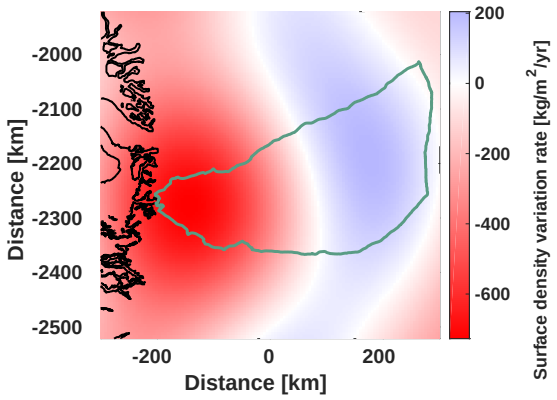

Figure 3.2: Surface density variation rate (5 km resolution). Notice that the coverage is different than in the other three figures. The green outline demarcates the Jakobshavn drainage basin [Zwally et al., 2012]. *Based on ITSG-2018 L2 maximum spherical harmonic degree 96 GRACE monthly solutions from TU Graz [Mayer-Gürr et al., 2018]. The observation period is from November 2010 until March 2016. Missing months are denoted in section 3.3.2.*

The mass loss near the terminus is confirmed by thinning maps (figure 3.1a and 2.23a) and the flow velocity map (figure 3.1b). The relatively strong mass accumulation in the Eastern part of the drainage basin however, is not visible in figure 2.23a. Furthermore, elevation change rates are near equilibrium with deviations in the order of centimetres. The maximum surface density variation rate in the East is up to a quarter of the minimum surface density variation rate near the terminus. It can be shown in figure 3.3 that this apparent mass accumulation is caused by the truncation to maximum spherical harmonic degree 96 (Gibbs phenomenon). Figure 3.3 shows a point mass simulation at the location of the strongest mass loss (figure 3.2).

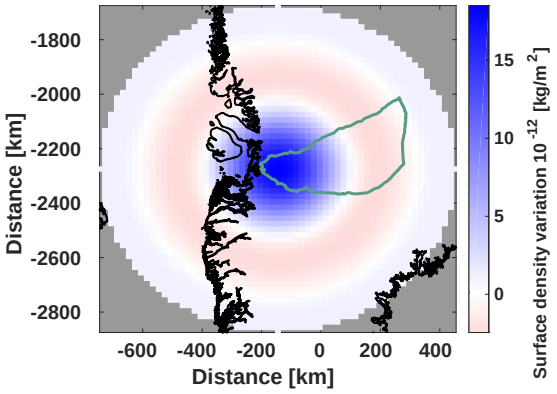

Figure 3.3: Simulation of the surface density variation using a point mass located at (-145.00;-2274.99). The 100 km wide ring of positive surface density variations at 250 km distance from the centre is a consequence of truncation within spherical harmonic synthesis.

In case of local mass loss near the terminus, an apparent mass gain is observed starting at 250 km distance from the centre of mass loss. Therefore, the mass accumulation signal in the East of the Jakobshavn drainage basin (in figure 3.2) is considered non-physical. Therefore, it should not be treated as another point mass signal as it is already part of point mass 1 (see table 3.1).
There is a possibility that the Sermeq Kujatdleq glacier contributes to the mass loss visible in figure 3.2. An attempt will be made to co-estimate the contribution of the neighbouring glacier. The locations of the two point masses are summarised in table 3.1 below.

Table 3.1: Coordinates of point mass locations.

№	Point mass	ϕ_0 [°]	θ_0 [°]	X [km]	Y [km]
1	Jakobshavn $\frac{\delta s}{dt}$ minimum	-48.65	69.18	-145.00	-2274.99
2	Sermeq Kujatdleq	-50.19	69.80	-200.00	-2201.00

The impact of co-estimation of point mass 2 on the scaling factor of point mass 1 is assessed by including and excluding it in the functional model.

Grid set-up

The point mass 1 should be adequately covered as it is the signals of interest. The point mass location should be within the grid of observations, otherwise the scaling factor is biased. Therefore, the grid is centered and circular around point mass 1. However, it is unknown which coverage is adequate. Therefore, the circular grid has varying grid point spacing and radius. The grid point spacing is varied from 10 up to 80 and the grid radius radius is varied from 25 km up to 300 km. The number of grid points for 10 km grid point spacing for one circular grid is displayed in table 3.2 below.

Table 3.2: Grid radius and corresponding number of points for a 10 km grid point spacing.

Grid radius [km]	25	50	75	100	125	150	175	200	225	250	275	300
Number of points [#]	21	81	177	317	489	706	973	1257	1597	1954	2377	2821

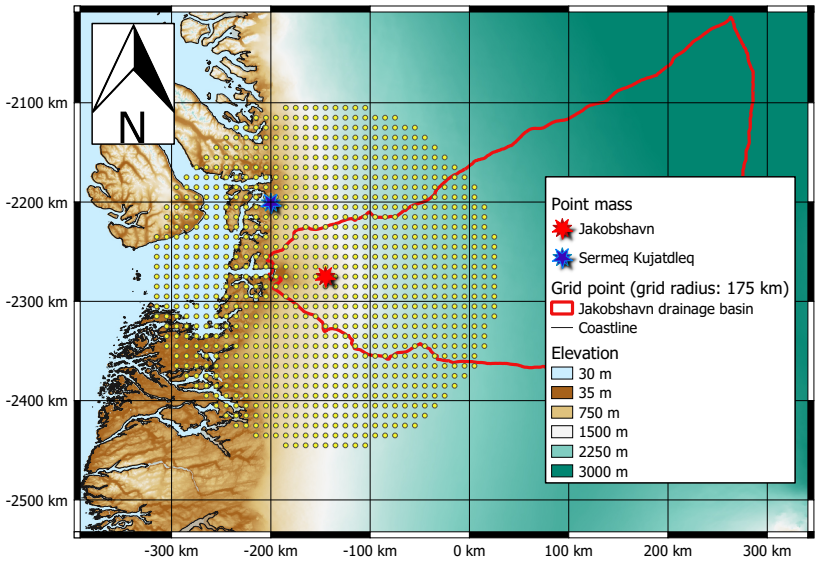

Figure 3.4: Example grid with 175 km radius. Grid is centered around the $\frac{\delta s}{dt}$ minimum (point mass 1, red star on in the West). The blue star marks the location of Sermeq Kujatdleq.

The distance from point mass 1 to point mass 2 is approximately 92 km.

3.3.2. Observed mass variations

Mass variations are inferred from GRACE observations on a grid around point mass 1. The GRACE L2 data product with maximum spherical harmonic degree 96 (ITSG-2018) was produced at TU Graz by Mayer-Gürr et al. [2018]). This and other exploited data products are summarised in table 3.3.

Table 3.3: Data used in this chapter. The normal-matrices for the GRACE monthly solutions of Mayer-Gürr et al. [2018] were not available at the moment of processing. Therefore, an earlier version of GRACE monthly solutions was used for the statistically optimal approach.

Dataset	**Degrees**	**Reference**
GRACE monthly solutions	$L_{max} = 96$	Mayer-Gürr et al. [2018]
GRACE monthly solutions	$L_{max} = 90$	Mayer-Gürr et al. [2016]
Monthly normal matrices	$L_{max} = 90$	Mayer-Gürr et al. [2016]
GIA	$L_{max} = 100$	A et al. [2013]
$C_{1,0}, C_{1,1}, C_{1,-1}, C_{2,0}$	-	Sun et al. [2016]

In the study period of November 2010 until March 2016 there are GRACE monthly solutions available for 51 out of 65 months. Missing months are January and June in 2011, May and October in 2012, March, August and September in 2013, February, July and December in 2014 and May, June, October and November in 2015.

First $C_{1,0}$, $C_{1,1}$, $C_{1,-1}$ and $C_{2,0}$ are replaced by more accurate Stokes' coefficients for each of the 51 GRACE monthly solutions by coefficients from Sun et al. [2016]. Subsequently, the *glacial isostatic adjustment* (GIA) is removed from the GRACE monthly solutions. Thirdly, the mean of every Stokes' coefficient in the study period is removed.

The adjusted Stokes' coefficients are converted into surface mass density variations using equation 3.6. This results in a surface mass density variation at each grid point. The functional model for estimating the mass of a point mass at a grid point for a single month is:

$$d(\theta_c, \phi) = k_1 \delta s_1(\theta_c, \phi) + k_2 \delta s_2(\theta_c, \phi) + k_3, \tag{3.11}$$

where $d(\theta_c, \phi)$ is the observed surface density variation at (θ_c, ϕ), k_1 and k_2 scaling factors of simulated point mass δs_1 and δs_2, respectively and k_3 estimates the underlying surface density variation offset or bias. Physically, the bias is included to account for possible errors in low-degree coefficients. k_1 validly represents a

mass estimate with the chosen grid set-up for a sufficient grid radius and grid point spacing. This leads to a linear system of equations for each GRACE monthly solution:

$$A\mathbf{x} = \mathbf{y}, \tag{3.12}$$

where observation vector $\mathbf{y}$ contains v surface mass density variations in kg/m^2 with v as the number of grid points and design matrix A, which contains a column for each simulated point mass in Gt/m^2 and a unit column. Equation 3.12 is solved using a LSE for each GRACE monthly solution. Formal error propagation is performed using:

$$Q_{\hat{x}\hat{x}} = \hat{\sigma}_y^2 (A^T A)^{-1}, \tag{3.13}$$

where $Q_{\hat{x}\hat{x}}$ is the noise covariance matrix of the estimated parameters and $\sigma_{\hat{y}}$ the standard deviation of data noise. The standard deviation of data noise is calculated via:

$$\hat{\sigma}_y = \sqrt{\frac{\mathbf{r}^T\mathbf{r}}{v-p}}, \tag{3.14}$$

where $\mathbf{r}$ are the residuals, v the number of observations and p the number of parameters estimated. The diagonal elements of $Q_{\hat{x}\hat{x}}$ are the variances of the estimated parameters assuming the noise in the observations is uncorrelated. Data noise is in this case however, severely correlated [Wouters et al., 2014]. Therefore, this estimate of standard deviation of data noise is based on an idealised assumption.

Statistically optimal observed mass variations

Decorrelation of observations can be realised through data weighting. To that end, the normal matrix (N) for each GRACE monthly solution [Mayer-Gürr et al., 2016] is used. The normal matrix is equal to the inverse noise covariance matrix ($Q_{yy,s} = N^{-1}$) of the Stokes' coefficients. Noise variances and covariances can be propagated directly from the spectral domain to the spatial domain via:

$$Q_{yy,d} = Y N^{-1} Y^T, \tag{3.15}$$

where $Q_{yy,d}$ (from now on simply referred to as Q_{yy}) is a $v \times v$ noise covariance matrix with v grid points, Y a $v \times w$ matrix that maps w Stokes' coefficients to v surface densities (see equation 3.6) and N an $w \times w$ normal matrix of the GRACE monthly solution.

Because the degree-1 and C_{20} coefficients were replaced, noise variances and covariances of those coefficients need to be derived separately as they are not provided. The covariances of the degree-1 and C_{20} are assumed to be zero and the variances were computed from time series of those coefficients using Variance Component Estimation (VCE) as described by Ditmar et al. [2018].

The calculation of Q_{yy} requires the inversion of N. In order to avoid direct inversion of N for robustness, the method described by Ran [2017] is followed. This method applies Cholesky decomposition and Singular Value Decomposition (SVD) to derive the eigenvalues (Λ) and eigenvectors (Q) of Q_{yy}. The covariance matrix Q_{yy} is then included in the LSE as follows:

$$\hat{\mathbf{x}} = (A^T Q_{yy}^{-1} A)^{-1} A^T Q_{yy}^{-1} \mathbf{y}. \tag{3.16}$$

Direct inversion of Q_{yy} is not possible, because Q_{yy} is ill-conditioned. Conveniently, truncation of the eigenvalue spectrum regularises Q_{yy}. The number of eigenvalues that need to be retained for a well-conditioned covariance matrix is unknown. Therefore, the truncation number is set by the magnitude of eigenvalues themselves. All eigenvalues up to X times smaller than the largest eigenvalue are used, the rest is set to zero. X is varied to investigate the sensitivity of the inferred mass to the truncation number. As mentioned by Ran et al. [2018], this data inversion scheme does not fully minimise dispersion because of the truncation. Finally, inversion of Q_{yy} is then simply performed by inverting each eigenvalue individually:

$$\tilde{Q}_{yy}^{-1} = Q_t \Lambda_t^{-1} Q_t^T, \tag{3.17}$$

where $\tilde{Q}_{yy}$ is the regularised full covariance matrix, Q_t is the truncated eigenvector matrix and Λ_t^{-1} is the truncated inverse diagonal eigenvalue matrix. With the inclusion of a full covariance matrix equation 3.13 changes therefore to:

$$\tilde{Q}_{\hat{x}\hat{x}} = (A^T \tilde{Q}_{yy}^{-1} A)^{-1}. \tag{3.18}$$

3.3.3. Mass change estimate

In the previous section, a mass estimate was made for the point masses included in the functional model for each monthly solution. A linear trend is estimated from the time series of point mass 1 using the following functional model:

$$d(t) = a_0 + a_1 \Delta t + a_2 \cos(2\pi\Delta t) + a_3 \sin(2\pi\Delta t) + a_3 \cos(4\pi\Delta t) + a_4 \sin(4\pi\Delta t), \tag{3.19}$$

where $d(t)$ is the mass at time t, Δt equals $(t - t_0)$, i.e. the time passed the with respect to an arbitrary reference time t_0, a_0 the mass change offset, a_1 the mass change, a_2 and a_3 are annual amplitude terms and a_4 and a_5 are semi-annual amplitude terms. The variance of $d(t)$ comes from the first diagonal entry of $\tilde{Q}_{\hat{x}\hat{x}}$ (equation 3.13 or 3.18 for ordinary and statistically optimal, respectively) and is used to weigh the observations according to equation 3.16. The weight matrix is in this case diagonal and does not require regularisation. The standard deviation of estimated mass change can be calculated by with equation 3.13 and 3.14 assuming white noise among the different monthly mass estimates. Therefore, the idealised error estimates of each of the mass estimates in the unweighted case have minor impact on the final mass change estimate. This is because the actual magnitude of each estimate within the time series is irrelevant. Only the respective (to other mass estimates in the time series) error magnitude is relevant. Therefore, the assumption is expected to be of minor impact.

The asymmetry in ablation and accumulation times and magnitude is accommodated by including semi-annual terms [Ditmar, 2018a]. Concretely, melt often takes place at a much quicker rate than snowfall in terms of mass change. Furthermore, the duration of melt and the duration of accumulation of snowfall are also rarely of equal duration.

3.4. Results & Discussion

In the first part of the result section, the results obtained by applying unweighted LSE to equation 3.12 are presented. In the second part, the results obtained by applying weighted LSE to equation 3.12 are presented. Set-ups 1 to 7 are concerned with the unweighted LSE and set-ups 8 to 14 are concerned with the statistically optimal (weighted) LSE. Set-up 1 is taken as the nominal set-up for comparison.

Table 3.4: Variation of set-ups in this section. Each set-up is one line in the indicated figure. Eigenvalue truncation factor is only used for the statistically optimal approach.
* Degree-1 and $C_{2,0}$ are removed before estimating mass and mass change.

Set-up №	Point mass	Grid radii	Eigenvalue truncation factor	Bias co-estimation	Grid point spacing [km]	Figure
1	1	all	-	yes	10	3.5, 3.6 and 3.7
2	1,2	all	-	yes	10	3.5
3	1	all	-	no	10	3.6
4	1	all	-	yes*	10	3.6
5	1	all	-	yes	20	3.7
6	1	all	-	yes	40	3.7
7	1	all	-	yes	80	3.7
8	1	all	10^8	yes	10	3.9
9	1	all	10^9	yes	10	3.9
10	1	all	10^{10}	yes	10	3.9
11	1	all	10^{11}	yes	10	3.9
12	1	all	10^{12}	yes	10	3.9
13	1	all	10^{13}	yes	10	3.9
14	1	all	10^{14}	yes	10	3.9

3.4.1. Mass change estimated with ordinary least squares estimation

In figure 3.5, the impact of co-estimation of point mass 2 is shown. The figure shows the scaling factor assigned to point mass 1 only (see equation 3.11).

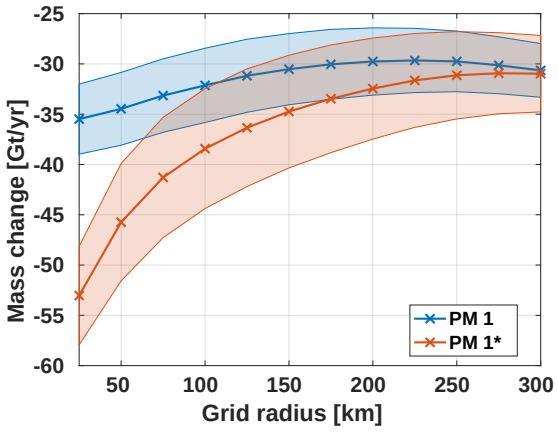

Figure 3.5: Impact of co-estimation of point mass 2 on mass change estimate as a function of grid radius. PM refers to point mass. PM* refers to the value of k_1 when point mass 2 is co-estimated. See table 3.1 for the point mass index. The error bar is 1-σ.

The introduction point mass 2 shows stronger negative mass change. It was expected that the co-estimation of point mass 2 would have a positive impact on the mass change of point mass 1, because the LSE assigns a part of the regional mass loss to the Sermeq Kujatdleq glacier instead of the Jakobshavn glacier. With growing radius, point mass 1 and 2 become relatively more similar for grid points far away. As a consequence, their mass change contribution converges to an equal division. Hence, co-estimation of point mass 2 shows gradual decrease in mass change.

Because the result of co-estimation of point mass 2 non-physical, the impact of neighbouring glaciers is minimised by minimising the grid radius only.

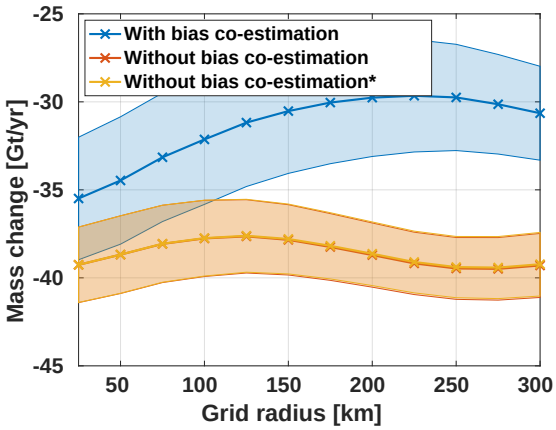

Figure 3.6: Impact of co-estimation of a bias on mass change estimate as a function of grid radius. The estimate without bias co-estimation with and without a * are almost the same. This indicates that the offset is not primarily caused by the degree-1 and $C_{2,0}$ Stokes' coefficients. The error bar is 1-σ.
* Degree-1 and $C_{2,0}$ are removed before estimating mass and mass change.

Figure 3.6 shows a 5 to 10 Gt/yr positive change when co-estimating a bias (k_3 in equation 3.11), which is up to one third of the new mass change estimate. It was postulated that low degree coefficients are responsible for this bias. This is not the case as removal of low degree Stokes' coefficients did not show similar mass changes as with bias co-estimation.

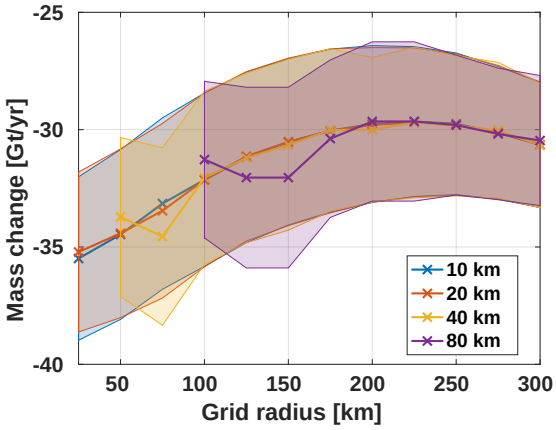

Figure 3.7: Impact of grid point spacing on mass change estimate as a function of grid radius. The error bar is 1-σ.

Figure 3.7 shows the impact of grid point spacing on the mass change estimates. Fluctuations are well visible for the 40 and 80 km solution. At 20 km, the solution shows minor fluctuations with respect to 10 km grid point spacing. Fluctuations of mass change for growing grid radius are marginal for the 10 km solution. Therefore, 10 km is considered adequate.
When co-estimating a bias only with 10 km grid point spacing, the curve first shows decreasing mass change up to 200 km radius. After approximately 200 km radius, the mass change becomes more negative. This indicates that mass loss observations neighbouring the location of point mass 1 are showing a more gradual decline than the simulated mass loss when moving away from point mass 1. Concretely, the approximate radius of maximum mass loss until equilibrium in figure 3.2 is larger than in figure 3.3. When the mass loss becomes more negative, neighbouring signals of mass loss start to contribute noticeably. Therefore, 200 km is considered adequate. This estimate shows a -29.8±3.3 Gt/yr for the Jakobshavn drainage basin and is based

on one point mass and bias co-estimation for 10 km grid point spacing. The corresponding time series for point mass 1 is shown below in figure 3.8.

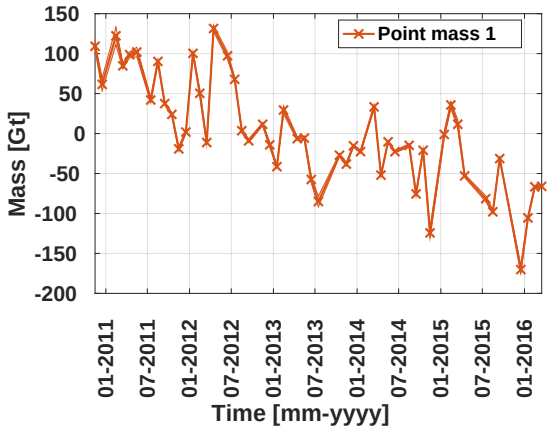

Figure 3.8: Time series based on ordinary LSE with point mass 1 (-29.8±3.3 Gt/yr) used for mass change estimate with 10 km grid point spacing, 200 km grid radius and bias co-estimation. The error bar is 1-σ.

3.4.2. Mass change estimated with statistically optimal least squares estimation

In this section, results of data weighted mass change is shown. Data weighting is applied to Stokes' coefficients using a noise covariance matrix as shown in section 3.3.2.1. Figure 3.9 shows the impact of truncation of the eigenspectrum on the mass change estimates. Important is the fact that the eigenspectrum is gradually decreasing, such that truncation is not straightforward.

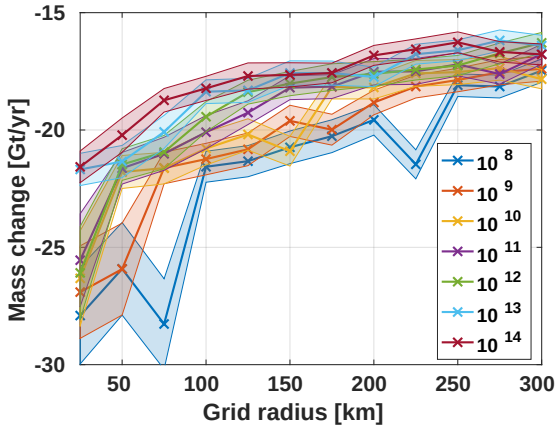

Figure 3.9: Impact of eigenspectrum truncation on mass change estimates. The legend shows the maximum factor that an eigenvalue can be smaller than the largest eigenvalue. Larger factors signify the retention of more eigenvalues. The error bar is 1-σ.

For grid radii of 100 km and larger, the mass change estimate deviates by approximately 10 Gt/yr from the unweighted estimate. To inspect the way the data weighting alters the set-up spatially, in particular the functional model, the spatial impact of weighting is derived by computing the decorrelated design matrix (for this procedure see section A.1 in the appendix). Figure 3.10a and 3.10b show the correlated (unweighted) and decorrelated (weighted) simulation of point mass 1 in the spatial domain, respectively, for truncation factor 10^{12} at 200 km grid radius for April 2014.

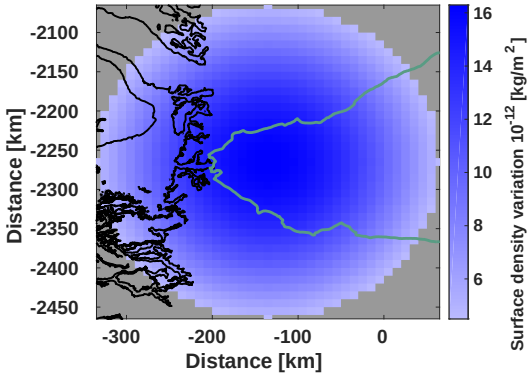

(a) Correlated point mass 1. The simulated point mass is well visible.

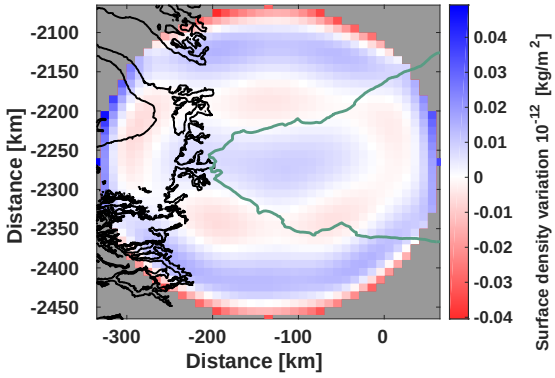

(b) Decorrelated point mass 1. The simulated point mass is not visible. Instead, edge-effects and patterns with unrealistically short wavelength are visible.

Figure 3.10: Insensitivity to simulated point masses in statistically optimal approach. The first column of the design matrix has been plotted in figure a and b. Truncation factor is 10^{12} with a 200 km grid radius and grid point spacing of 10 km for monthly solution of April 2014.

The intended scaling of a point mass using weighted LSE does not reflect the physical signal that is present in the area. Further research showed that grid point spacing, grid shape or truncation factor do not alleviate the insensitivity towards the functional model, i.e. the simulated point mass. A larger grid (>500 km radius) showed improvement, i.e. the unrealistically short wavelength signals (see figure 3.11 below) have largely been removed or have shifted to the edge. However, these grid sizes are unfeasible for this study.

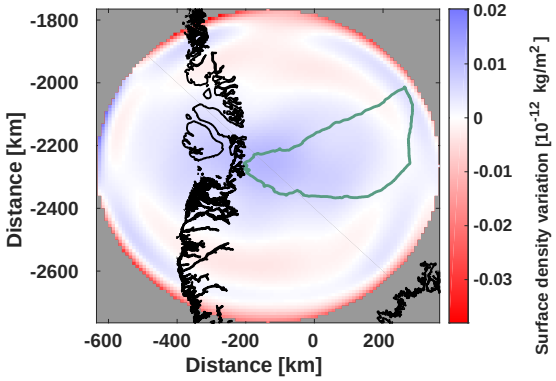

(a) Decorrelated point mass 1 with a 500 km large grid radius. The short wavelength features that were visible in figure 3.10b have mostly disappeared within the Jakobshavn drainage basin. However, edge effects are still present.

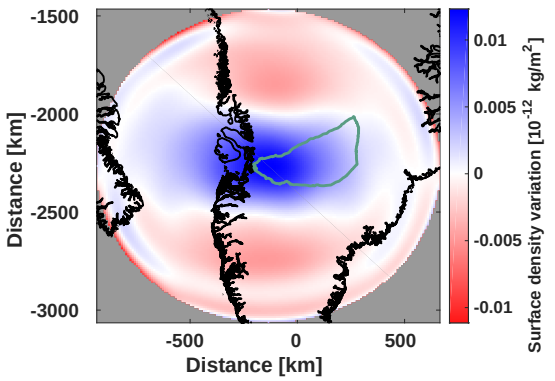

(b) Decorrelated point mass 1 with an 800 km large grid radius. The short wavelength features that were visible in figure 3.10b have mostly disappeared within the Jakobshavn drainage basin. The edge effects that are visible in figure 3.11a have displaced to close to the 800 km radius.

Figure 3.11: Decorrelated point mass 1 for large grid radii. Truncation factor is 10^{12} with a 500 and 800 km grid radius and grid point spacing of 10 km for monthly solution of April 2014. Note that the colour bars do not have the same limits.

The decorrelation filter ($C_d^{-\frac{1}{2}}$) visibly matches the stochastic properties of noise in figure 3.11b. The noise is correlated along track due to orbit geometry along with low frequency noise in the original L1 data time series. Furthermore, the noise is anti-correlated across-track (causing striping [Wouters et al., 2014]).
Based on the seemingly adequate result in figure 3.11b, it is proposed that 1) the point mass is simulated on a grid with a radius that is a few times larger than the desired grid radius and that 2) statistically optimal scaling takes place with a truncated, decorrelated functional model and observations. Truncation here means that all grid points beyond the desired radius are discarded. Figure 3.12 shows the decorrelated point mass from figure 3.11b where the decorrelation filter and the functional model have been truncated before multiplication.

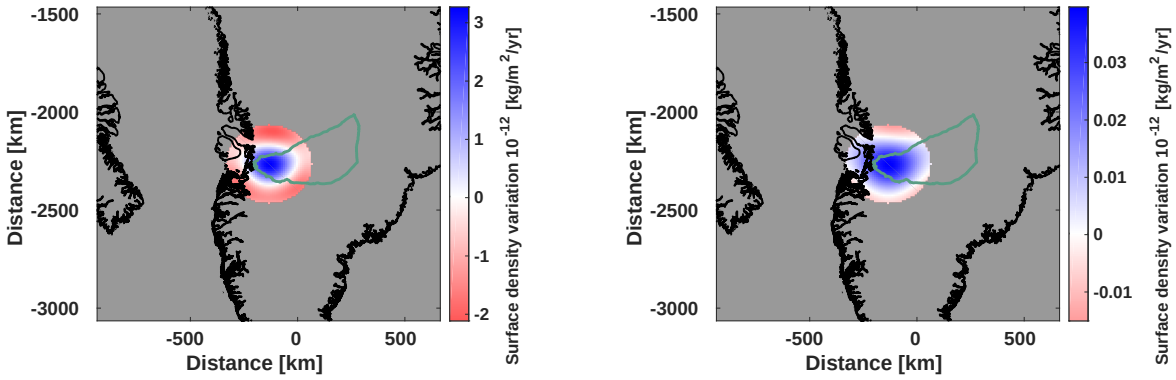

(a) Eigenvalue truncation factor is 10^{12}.

(b) Eigenvalue truncation factor is 10^{6}.

Figure 3.12: Decorrelated point mass 1 with 800 km grid radius truncated to 200 km. Truncation factor (for eigenvalue spectrum) is 10^{12} in a) and 10^{6} in b) with a grid point spacing of 10 km for monthly solution of April 2014.

It can be seen in figure 3.12a that the point mass crosses zero just over 100 km away form the point mass location, which is much more rapidly than in the simulated point mass (i.e. approximately 200 km, figure 3.3). This may indicate that more regularisation is required. To that end, the regularisation factor is decreased to meet the 200 km radius to its first zero crossing. A regularisation factor of 10^{6} shows (figure 3.12b) a point mass signature resembling the unweighted simulated point mass. Thereafter, the corresponding time series is created using an 800 km radius for synthesis, then truncating the functional model, observations and decorrelation filter to 200 km radius, where the decorrelation matrix has been regularised using a truncation factor of 10^{6}.

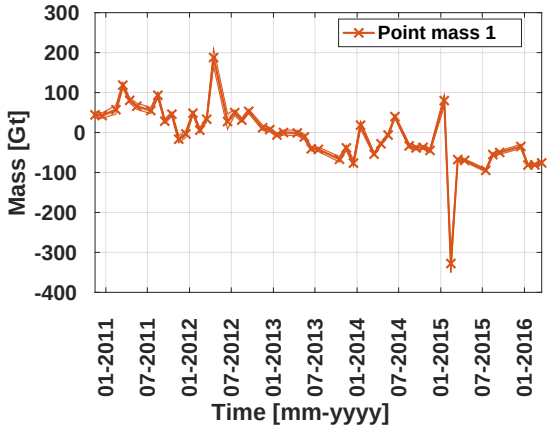

Figure 3.13: Time series based on truncated decorrelated LSE with point mass 1 used for mass change estimate with 10 km grid point spacing, 800 km grid radius (truncated at 200 km) and bias co-estimation. Truncation factor (for eigenvalue spectrum) is 10^{6}. The error bar is 1-σ.

It is expected that the resulting time series is less noisy. Unexpectedly, the time series in figure 3.13 which was constructed using the description above, shows parts with reduced as well as increased noise. At this stage it is realised that this may be due to the inherent implications of the truncation factor of the eigenvalue spectrum. The factor was meant to balance the eigenvalues among different months by magnitude. However, it also implies that months within the time series may have a reduced eigenvalue spectrum with respect to other months. If that is the case, then outliers in figure 3.13 should contain relatively few eigenvalues after truncation with the truncation factor. Solution of April 2012, January 2015 and February 2015 are easily identified as outliers. The number of retained eigenvalues for each month is shown in figure 3.14 and confirms this observation.

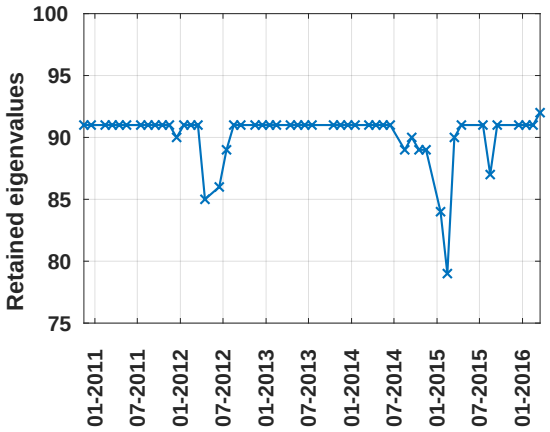

Figure 3.14: Number of largest retained eigenvalues of the noise covariance matrix after regularisation for each month. The outliers in figure 3.13 correspond well with less than average retained eigenvalues. In other words, the outliers have a smaller eigenspectrum.

The final step is to see if the outliers can be adjusted by retaining the largest 91 eigenvalues (instead of using a truncation factor) of the noise covariance matrix for all months. The corresponding time series is shown in figure 3.15.

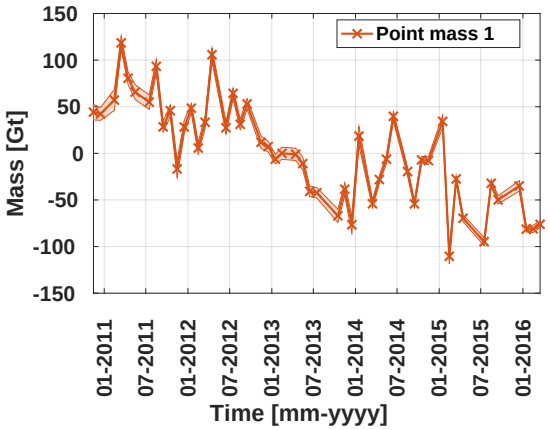

Figure 3.15: Time series based on truncated decorrelated LSE with point mass 1 used for mass change estimate with 10 km grid point spacing, 800 km grid radius (truncated at 200 km) and bias co-estimation. The eigenvalue spectrum of the noise covariance matrix of each monthly estimate was truncated to the largest 91 eigenvalues. The error bar is 1-σ.

Figure 3.15 shows that the identified outliers indeed originated from a more reduced eigenspectrum. Furthermore, noise appears only marginally reduced with respect to the unweighted time series (figure 3.8). The mass balance corresponding to his new time series is -26.6±2.9 Gt/yr. The new time series still shows differences within the time series regarding to noisy months. For instance, the years 2014 and 2015 appear relatively noisy compared to 2013. This suggest that more subtle adjustments of the number of eigenvalues that need to be retained are required, because the decay of the eigenvalue spectrum is different for each month.

4

Removal of the Surface Mass Balance

This chapter provides a brief intro to RACMO; the source from which we derived the SMB. After that, the SMB is further elaborated upon, continuing on the explanations given in paragraph 1.1. Then the RACMO dataset, provided by IMAU at Utrecht University, is visualised and further analysed in the context of the study area. Subsequently, the derivation of the ice discharge using the results from chapter 2 and 3 in combination with the estimated SMB from this chapter is shown.

4.1. Introduction: A regional climate model

RACMO is a RCM to simulate the SMB tailored to the Arctic and Antarctic. In early 1990, the KNMI and the Danish meteorological institute (DMI) developed RACMO for research purposes [IMAU]. The current version of RACMO, RACMO 2.3p2, is based on a numerical weather prediction (NWP) model, i.e. the High Resolution Limited Area Model (HIRLAM), and a physics model from the European Centre for Medium-Range Weather Forecasts Integrated Forecast System (ECMWF-IFS) [Noël et al., 2018]. Figure 4.1 illustrates the components involved in an IFS model.

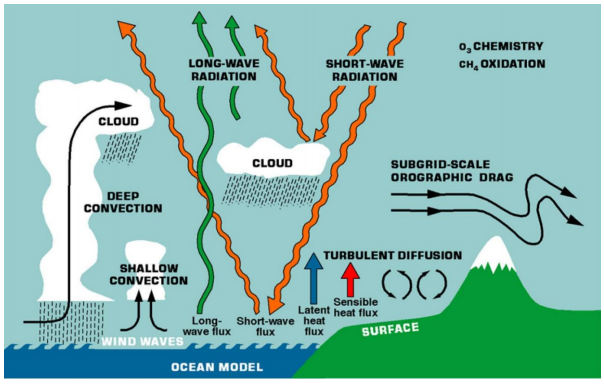

Figure 4.1: IFS model with the included components, which is used in RACMO2. *Taken from ECMRWF [2008]*

The accuracy of RACMO model was partially derived by Noël et al. [2018] through comparison with observations, from e.g. automatic weather station records. Noël et al. [2018] found that run-off was poorly resolved in narrow glaciers due to the relatively large resolution of 11 km length and width (statistically downscaled to 1 km). Therefore, this RACMO version models the SMB at 5.5 km scale, which has been statistically downscaled to 1 km.

4.1.1. SMB and Ice discharge

In the previous two chapters, estimates of the MB were made. Figure 4.2 shows the SMB in kg/m^2/yr or equivalently in mm/w.e./yr. Relatively strong negative rates are found near the coast and slightly positive inland within the Jakobshavn drainage basin. These findings correspond well with the long term rates derived by Ettema et al. [2009] using an earlier version of RACMO 2.

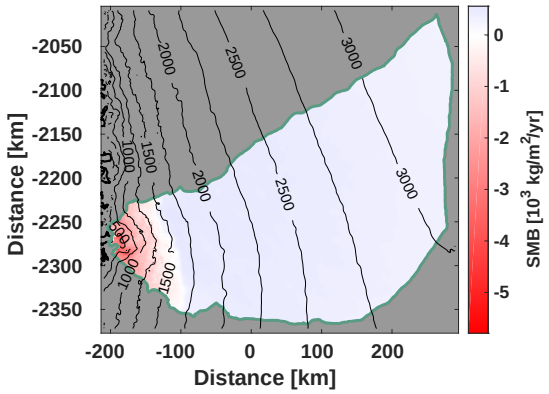

Figure 4.2: Annual SMB per square kilometre (estimation period: November 2010 until March 2016). The contour lines (derived from the DEM [Howat et al., 2017], which was also used in chapter 2) indicate elevation in metres.

SMB equilibrium is attained between roughly 1300 m up to 1700 m elevation. With negative elevation rates (section 2.4.5), this means that the ELA is likely above 1300m. The ELA was used in section 2.4.5 as a boundary within the linear density model. The density of ice was assumed for the volume change estimates below the ELA. A higher ELA indicates a larger contribution of ice loss with respect to firn/snow. This leads to stronger mass change estimates. The ELA was varied to account for ELA uncertainty.

4.2. Theory & Methodology

The goal is to obtain the SMB from the RACMO 2.3p2 model in the Jakobshavn drainage basin over the period November 2010 - March 2016. To that end, the surface mass anomaly (SMA) is integrated over the basin per month after which the basin wide linear trend is estimated using the following functional model:

$$SMA(t) = a_0 + a_1\Delta t + a_2\cos(2\pi\Delta t) + a_3\sin(2\pi\Delta t) + a_4\cos(4\pi\Delta t) + a_5\sin(4\pi\Delta t), \tag{4.1}$$

where Δt is equal to $(t - t_0)$, i.e. the time passed the with respect to an arbitrary reference time t_0, a_0 the SMA offset (intercept), a_1 the SMB, a_2 and a_3 as well as a_4 and a_5 are amplitude terms of the annual and semi-annual components (e.g. $Amplitude = \sqrt{a_2^2 + a_3^2}$), respectively. Semi-annual terms are added, because the ablation and accumulation period do not last equally long (see section 3.3.3). The standard deviation of data noise ($\hat{\sigma}_y$) is calculated with:

$$\hat{\sigma}_y = \sqrt{\frac{\mathbf{r}^T\mathbf{r}}{n-p}}, \tag{4.2}$$

where $\mathbf{r}$ the residual vector, n the number of observations and p the number of estimated parameters. The covariance matrix of the estimated parameters ($Q_{\hat{x}\hat{x}}$) is then computed via:

$$Q_{\hat{x}\hat{x}} = \hat{\sigma}_y^2(A^TA)^{-1}, \tag{4.3}$$

where A is the functional model from equation 4.1. The values of $Q_{\hat{x}\hat{x}}$ are valid under the assumption that the data noise is uncorrelated. The error estimate of the inferred SMB is the RSS of the standard deviation of the estimator ($\hat{\sigma}_x$) and a model error of 20% [van den Broeke et al., 2016]:

$$E_{SMB} = \sqrt{\hat{\sigma}_x^2 + \left(0.2 \cdot SMB\right)^2}. \tag{4.4}$$

Subtraction of the CryoSat-2 inferred mass balance MB_{CS2} from the SMB, directly results in an estimate of the ice discharge ID_{CS2}, as indicated in equation 4.5. The error of ID_{CS2} is computed with the RSS of the errors of each component in:

$$ID_{CS2} = SMB - MB_{CS2}. \tag{4.5}$$

Likewise for the GRACE estimate:

$$ID_{GRACE} = SMB - MB_{GRACE}. \tag{4.6}$$

A more adequate approach however, would be to convert the SMA to the spectral domain through synthesis. Then the SMA can be spectrally limited to a maximum spherical harmonic degree to ensure spectral consistency. Unfortunately, when using this approach, the point mass assumption is violated and an estimate of the scaling factor becomes arbitrary. This approach was therefore unsuccessful.

4.3. Results & Discussion

Figure 4.3 shows the SMA within the study area. The annual variability is clearly visible, with a decrease in SMA in summer, and increase throughout the rest of the year (roughly September until May). Concretely, this indicates more snowfall and refreezing than melt and sublimation in terms of mass. Furthermore, the summer of 2013 reveals a relatively weak mass loss signal, whereas the summer of 2012 shows a relatively strong mass loss signal. This time is was reported as the 2012 melt event [McMillan et al., 2016, Nilsson et al., 2015]. The strong summer melt in 2012 was a consequence of an increased North Atlantic Oscillation index [Wouters et al., 2014]. This index is associated to large scale pressure patterns, controlling westerly winds across the North Atlantic. The 2012 melt event led to strong biases (56±26 cm) in the CryoSat elevation estimates across Greenland due to changing scattering properties of the surface [Nilsson et al., 2015]. It should be noted that the 2012 melt event mostly took place North of 70° N [Nilsson et al., 2015], i.e. North of the study area.

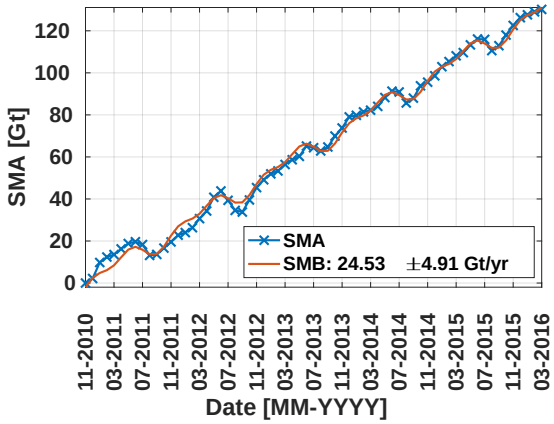

Figure 4.3: SMA in the Jakobshavn drainage basin in blue with the model fit in red. The standard deviation consist of the RSS of the model fit error (0.2 Gt/yr) and the SMB model error (4.9 Gt/yr).

The linear rate was estimated at 24.5± 4.9 Gt/yr, with the total error as the RSS of the formal standard deviation of the estimated parameter and a model error. The amplitude of the annual and semi-annual signal was estimated at 3.6±0.6 Gt and 2.5±0.6 Gt, respectively.
The ice discharge derived from CryoSat-2 data, unweighted GRACE monthly solutions and weighted GRACE monthly solutions in combination with RACMO are then calculated via equation 4.7, 4.8 and 4.9, respectively:

$$ID_{CS2} = 24.5 + 24.7 = 49.3\,Gt/yr, \tag{4.7}$$

with an error of 5.7 Gt/yr. For GRACE this results in

$$ID_{GRACE} = 24.5 + 29.8 = 54.3\,Gt/yr, \tag{4.8}$$

with an error of 5.9 Gt/yr for the unweighted solution and

$$ID_{GRACE} = 24.5 + 26.6 = 51.1\,Gt/yr, \tag{4.9}$$

with an error of 5.7 Gt/yr for the weighted solution.

5

Discussion, Conclusion & Recommendations

The goal of this study was to derive the ice discharge and its corresponding error budget from swath processed CryoSat-2 volume data and GRACE monthly solutions in combination with RACMO modelling results over the Jakobshavn drainage basin in Greenland in the period of November 2010 until March 2016.
The MB derived from CryoSat-2 data yields -24.7±3.0 Gt/yr. The MB derived from GRACE monthly solutions was estimated at -29.8±3.5 Gt/yr and -26.6±2.9 Gt/yr for the unweighted and weighted solution, respectively. The MB's combined with the SMB estimate of 24.5±4.9 Gt/yr this yields an ID of 49.3±5.7 Gt/yr for the CryoSat-2 based estimate. For the GRACE-based estimate this results in an ID of 54.3±5.9 Gt/yr and 51.1±5.7 Gt/yr for the unweighted and weighted solution, respectively. The estimates are obtained over the observation period of November 2010 until March 2016 within the Jakobshavn drainage basin.

King et al. [2018] (in review) studied the ice discharge time series of entire Greenland. Time series were created by integrating the ice flow velocities over the flux gates assuming the density of ice. The time series shows an average ice discharge of 50.8±2.2 Gt/yr for the Jakobshavn glacier, which is within error of our estimates. Before the ice flow acceleration in 2011 [Lemos et al., 2018], the ice discharge was estimated at approximately 30 Gt/yr [Howat et al., 2011]. Furthermore, our two semi-independent estimates, i.e. altimetry-derived and gravimetry-derived are also in reasonable agreement with each other. Considering that, as well as the aforementioned acceleration event and the agreement with King et al. [2018] (in review), provides confidence in the presented ice discharge estimates. Nevertheless, context of the estimates is provided by briefly addressing significant intermediate assumptions and choices.

The selection of valid waveform samples was performed by selecting samples that have a low phase difference dispersion. Samples are considered valid in the sense that they correspond with actual surface scatterers. Selection of samples by phase difference dispersion essentially selects the samples which are within smooth parts of the phase difference recordings. It was found that using this method for valid waveform sample selection is overall more reliable than when taking coherence as a threshold criterion. This is because the optimal threshold among 6 drainage basins in Greenland varies marginally for the phase difference dispersion (variation: [0.97,0.99]) with respect to the coherence (variation: [0.58,0.92]) (both quantities range from 0 to 1). Optimal was defined through a measure that minimises the standard deviation of elevation differences (w.r.t. a DEM) and maximises the number of elevation estimates.
Hypsometric averaging was improved by considering two fits for a dynamic and non-dynamic region based on flow velocities. The difference between volume changes when using direct summation (integration) of individual volume changes and when using hypsometric averaging is minor (<1 km^3/yr), similar to what was found by Wouters et al. [2015] upon comparing the difference between direct integration and adequate hypsometric averaging.
The preferred density model (linear model) has an average effective density of 840 kg/m^3. Huss [2013] showed that effective densities are generally within 850±60 kg/m^3 for a glacier under certain conditions that are likely met in this study. The mass change estimates from different density models (flow velocity and linear density) in this study are within 1-σ of each other. The linear density model includes a varying transition zone,

whereas the flow velocity based density model does not. Furthermore, the flow velocity threshold which separates ice and snow/firn was varied linearly. It was found that the flow velocity profile away from the terminus is not linear such that the mass change estimate and its corresponding uncertainty are inadequately varied. As a consequence, the flow velocity model likely underestimates mass loss.
With GRACE data, the data noise was assumed white for the ordinary least squares estimation of monthly mass estimates. By literature, e.g. [Jekeli, 2007, Wouters et al., 2014], it is known that data noise is not white. This idealised noise estimate is used as weights for each of the data points when assessing the linear mass change of the mass time series through WLSE. As this assumption is too idealistic, caution is required when investigating individual data points. However, when inferring the linear mass change from the time series, only the respective (to other mass estimates in the time series) error magnitude is relevant. Therefore, the assumption is expected to be of minor impact.
Subtraction of the GIA is done in the spectral domain, i.e. from the Stokes' coefficients to maintain spectral consistency. The derived product becomes an approximation with the (in)ability to project signals only up to a minimum wavelength upon truncation of the Stokes' coefficients to a maximum the degree. To illustrate, the GIA has been corrected for in terms of Stokes' coefficients, whereas the SMB could not be subtracted in the spectral domain. The magnitude of the SMB is too large, i.e. of the same order as the MB. As a consequence, the scaling of the point masses would result in invalid mass change estimates. Therefore, the spectrally unlimited (in the spatial domain) SMB was subtracted and a spectral inconsistency was introduced. The SMB is fairly smooth in the region of the Jakobshavn drainage basin (see figure 4.2), such that it is expected that the spectrally consistent ice discharge estimate would not differ significantly.
It was shown that GRACE can be used to infer ice discharge if a local and sufficiently strong mass change signal with respect to its wide vicinity is present. Uncertainty to which extend this condition needs to be met may be accommodated by including (multiple) point masses. However, care must be taken of the physical meaning of observed mass change signals, because a strong change is paired with radially alternating mass change signals (side lobes of sinc-function) due to truncation.
Furthermore, it was shown that data weighting directly on a local field of observations has an adverse effect on the simulated observations. In our case, this meant that the simulated point mass signature was destroyed. This was found when considering the noise covariance matrix in the spatial domain as a decorrelation filter. This decorrelation filter was then applied to the simulated point mass. It was also shown that the adverse effects of weighting can be mitigated on a local scale upon increasing the observational area. Afterwards, the desired observations can be extracted from the decorrelation filter, design matrix and observation vector for LSE. Furthermore, it was shown that the number of eigenvalues of the noise covariance matrix retained (for regularisation) for each month may need individual evaluation.

5.1. Conclusion

The research questions as stated in chapter 1 are shown below. A concise explanation is given to each research question which, altogether provide suitable and workable context for the research objective.

Q. 1 *What are the key parameters in the implementation of the CryoSat-2 swath processing scheme for elevation change estimation?*

In chapter 2 the coherence, look angle, normalised waveform energy, phase difference dispersion, power and slope were investigated. A DEM was used to remove the most severe outliers.
Parameter optimisation was performed using an optimisation parameter that penalises a high standard deviation and rewards a large number of points.
The coherence and phase difference dispersion are key parameters in the swath processing scheme, because of their ability to reduce the standard deviation significantly. Optimisation of these two parameters was performed simultaneously with the look angle and showed a reduction of the standard deviation of elevation differences ranging from at least 29% up to 67% (optimised phase difference dispersion and look angle threshold) and at least 29% up to 71% (optimised coherence and look angle threshold) for 6 different drainage basins. When varying thresholds these thresholds, the strongest gradient occurs for the phase difference dispersion and coherence, such that it can be concluded that these are more effective when reducing the standard deviations of elevation estimates than the look angle. The optimal coherence threshold performs slightly better than the optimal phase difference dispersion threshold however, the optimal coherence threshold changes substantially from basin to basin, whereas the phase difference dispersion changes marginally. As a consequence, a higher coherence

does not always improve the optimisation parameter. In case of missing control data it is thus always advised to use the phase difference dispersion.
Optimisation of the maximum and minimum normalised waveform energy threshold reduces the standard deviations of elevation estimates by 1% to 9% for the 6 different drainage basins.
It was found that power and slope are not suitable for sample selection, because of the poor distribution of points. Applying a threshold on these parameters would mean a substantial loss of good quality (<15 m elevation difference with DEM) elevation estimates.

Q. 2 *How can the GRACE mass anomalies, the CryoSat-2 elevation estimates obtained through swath processing and the RACMO modelled SMB be combined consistently to reveal the ice discharge in Jakobshavn in Greenland?*

By subtraction of the MB from the SMB, the ice discharge is retrieved. It was shown that CryoSat-2 data can provide elevation change consistent with OIB elevation estimates using swath processing. Elevation change was derived using WLSE with a search radius where weighting was based on distance to the estimation point. Hypsometric averaging and a density model were used to infer volume and mass changes within the basin. It was shown that hypsometric averaging can be improved by separating fits based on flow velocity. The computed volume loss is in good agreement (<1-σ) with CryoTop volume change estimate. Furthermore, two different density models show reasonable results and are within error bar of each other. Mass change error consist of a hypsometric misfit, basin outline uncertainty and volume-to-mass conversion uncertainty.
GRACE monthly solutions were used to estimate monthly mass anomalies using an improved scheme that incorporates the radius of the reference ellipsoid instead of a spherical Earth. GIA was subtracted and degree-1 and $C_{2,0}$ Stokes' coefficients were replaced. The limited resolution of the GRACE data does not allow for direct integration of each observation point, in contrast to CryoSat-2 elevation change estimates. To that end, consistency between observation areas of CryoSat-2 and GRACE based mass change is (largely) maintained by making a point mass assumption. It was shown that scaling of a simulated point mass to that of the observations yielded mass change estimates that are in agreement (<1-σ) with the CryoSat-2 mass change estimates. Sensitivity of the chosen set-up was studied by varying grid radius, grid point spacing, bias co-estimation and point masses. It was shown that grid radius and grid point spacing affects mass change estimates marginally when the radius is sufficiently large. Bias co-estimation yields a significant deviation of roughly 33% when omitting it. Furthermore, an additional point mass located at a glacier in the vicinity of the Jakobshavn glacier resulted in non-physical behaviour, increased mass change error and thus did not improve the final estimate. The statistically optimal estimate of the mass change required an increased grid radius to keep the simulated point mass intact. Selection of observations in the enlarged grid can be done after computing the decorrelation filter. Individual regularisation of the noise covariance matrix for each month was omitted in this study, but would increase confidence in the statistically optimal time series.
SMB estimate were made based on cumulative monthly RACMO 2.3p2 SMA output. Subtraction of the CryoSat-2 and GRACE-based MB from the SMB was done in the spatial domain. Regarding the subtraction of the GRACE-based MB from the SMB, a spectral inconsistency had to be introduced. This is because the point mass assumption is violated when subtracting the SMB in the spectral domain. However, it is expected that the bias introduced by spectral inconsistency is much smaller than the bias introduced by direct integration of the Jakobshavn basin GRACE observation points.

Q. 3 *What limitations emerge from the RACMO data inclusion, the GRACE and CryoSat-2 data acquisition and chosen processing methods and how do these jointly affect the ice discharge estimates?*

In this research, no time series of mass estimates was created per grid cell with CryoSat-2 data, because the goal was the long term linear trend of the ice discharge. However, such time series do provide excellent insight in the evolution of mass estimates. In contrast, time series were made from GRACE and SMA data. A time series can, in practice, be constructed from the CryoSat-2 data. In hindsight, with the number of available elevation estimates it may have been possible to do so for the part of the Jakobshavn drainage basin that is observed by CryoSat-2 in SIN mode. Larger grid cells are however, needed to accommodate time series within the LRM area.
Furthermore, care needs to be taken of an adequate DEM for global phase unwrapping, regardless of the optimal choice of parameters. If the DEM is not sufficiently up-to-date, CryoSat-2 swath processing

fails. Additionally, the elevation error estimate is made on the basis of the difference with a DEM. It can be shown that errors over 50 m can actually be relatively accurate (<5 m difference with OIB elevations), due to the missing temporal component in the DEM. Since validation of elevation estimates with OIB is limited (3% of obtained data within a given month), a full picture of elevation estimate quality cannot be obtained. This however, does not affect the optimisation of thresholds.
CryoSat-2 based mass change estimates are always prone to volume to mass conversion errors, unlike GRACE based mass change estimates.
As for the GRACE based mass change estimate, the potential mass loss signal of the Sermeq Kujatdleq glacier could not be separated due to limited magnitude and resolution. It is therefore also not known if and how much it contributes to the observed GRACE mass change.
The inclusion of the noise covariance matrix for GRACE based mass estimates alters the design matrix in such a way that the location of the point mass becomes largely irrelevant on a drainage basin scale. Data weighting has therefore not been able to improve the mass estimates without data weighting. Unfortunately, this also affects confidence in the error estimate of the GRACE based mass change estimates as they are based on white data noise.
Finally, the SMB model error of 20% is a rough estimate as the actual SMB error is not accurately known.

5.2. Recommendations for future research

For future studies, the following recommendations may prove beneficial:

Chapter 2: Mass change through altimetry

- The functional model (equation 2.13) presented in section 2.3.3 estimates coefficients related to spatial and temporal components of the elevation. Throughout chapter 2 the primary goals was to assess the temporal aspect. However, a DEM can be constructed from the coefficients related to the spatial components. In section A.6 in the appendix, the elevation offset between the DEM by Howat et al. [2017] and a CryoSat-2 based DEM at time t_0 (see section 2.3.3) is given. The CryoSat-2 based DEM can in turn be used for more reliable global phase unwrapping when t_0 is set to e.g. halfway the observation period or can be calculated at each moment in time explicitly. This however, requires estimating the elevations twice and an initial DEM that is not too inaccurate (likely in the order of 10's of metres).

- In late 2003, the Jakobshavn glacier had lost the glacier tongue [Muresan et al., 2016]. This lead to increasing seasonal variation Howat et al. [2011]. Alternating magnitude is not included in the current functional model (equation 2.13) for elevation change estimates. The functional model can be expanded with $a_n \Delta t \cos(2\pi\Delta t)$ and $a_{n+1} \Delta t \sin(2\pi\Delta t)$ as well as $a_{n+2} \Delta t \cos(4\pi\Delta t)$ and $a_{n+3} \Delta t \sin(4\pi\Delta t)$ to infer a linear increase in amplitude. Non-zero outcome of a_n up to a_{n+3} when applying (W)LSE then indicate increasing or decreasing amplitude. However, over long periods this linear estimate may likely not capture short term increase or decrease. Additionally, functional model adaptations can be statistically tested for significance.

- In chapter 2 hypsometric averaging was performed. The polynomial fits that were used to interpolate data gaps and integrate the elevation change rates were introduced as a function of elevation. It was found that elevation changes does not primarily depend on elevation, but also on ice flow velocity. To that end, two polynomials were introduced to accommodate elevation changes in fast flowing and slow flowing regions. A next step would be to include velocity in the polynomial fit $p(h_i, v_i)$ of the form:

$$p(h_i, v_i) = \sum_{n=0}^{N} c_n h_i^n + \sum_{m=0}^{M} d_m v_i^m, \tag{5.1}$$

  where h_i is the elevation at location i, v_i the flow velocity at location i, N the maximum degree of the polynomial that accounts for elevation with unknown coefficient c_n and M is the maximum degree of the polynomial that accounts for flow velocity with unknown coefficient d_m. In this way, only one hypsometric fit is required instead of two.

- Choices for a suitable polynomial fit when applying hypsometric averaging can be supported by applying F-testing [Foresta et al., 2018]. With it, the change or improvement of higher order polynomials can be evaluated by statistical significance.

- The method for deriving elevation change uses an Eulerian (fixed) reference frame. Moholdt et al. [2014] showed that instead of an Eulerian (fixed) reference frame, it can be beneficial to use a Lagrangian (moving) reference frame. This excludes advection of ice thickness gradients from the elevation observations between different epochs. Concretely, this means that velocity information is required to compute the underlying topography at each measurement epoch. The topographic difference between two measurement epochs can be attributed to two components, i.e. to (advection) due to a non-zero velocity field and accumulation/ablation. As CryoSat-2 SIN mode is especially useful in rough terrains, advection may be playing a more significant role than it was the case in this study. Moholdt et al. [2014] showed that changing the reference frame from Eulerian to Lagrangian reduced the variability of elevation change by 50% for the Ross and Filchner-Ronne ice shelves in Antarctica.

- The volume change was converted to mass change using two different density models. The density within the models depended on certain set-up parameters (i.e. ELA, firn density and ice flow velocity to separate the dynamic and non-dynamic region). These parameters were varied linearly within likely bounds to assess the sensitivity of the density model to those parameters. It was found that the variation of the ice flow velocity threshold should be chosen carefully. This is because a cross-section of the ice flow velocity away from the terminus is non-linear. Linear variation of this parameter as was done in this study therefore likely biases the mass change estimate and volume-to-mass conversion error estimate.

- Elevation and elevation change estimates based on observations from ascending tracks deviates from elevation and elevation change estimates based on observations from descending tracks. This was concluded after performing the WLSE in chapter two when using only observations from ascending orbits or descending orbits (see section A.5 in the appendix). Concretely, 24% of the elevation change estimates differences were over 1 m/yr. It was found that elevation change estimates based on observations in ascending track are on average more positive between the terminus and mode boundary. The exact source and adequate treatment of this bias requires further research.

- The procedure to obtain CryoSat-2 based mass change estimates also applies to other drainage basins in Greenland. When choosing PD dispersion instead of coherence, the parameters do not need to be adjusted considerably as it was shown that optimal PD dispersion thresholds vary only marginally among different basins. However, the hypsometric fit as used in this study may likely not be suitable for other drainage basins. Other parameters, such as flow velocity (suggested above) and latitude may need to be included. Furthermore, the ELA differs per drainage basin. In fact, it likely differs within a drainage basin. This may increase the relative contribution of the volume-to-mass conversion error to the total mass change error estimate and thus needs to be considered carefully.

Chapter 3: Mass change through gravimetry

- The statistically optimal approach for the scaling of a point mass to observations to infer mass was only partially successful. The size of the observation area appears to play a vital role in the outcome of such estimates. It is however, not investigated *how* this aspect dominates the point mass signature. Correlated and decorrelated simulations of point masses and more natural mass distributions may shed more light on the destructive behaviour of data weighting for small observational areas. Second point of interest is then on how to adequately tackle this issue if possible. As shown in the last section of chapter 3, spatial truncation of the decorrelated simulated point mass *after* calculation in a wide area improved the point mass signature. Overall scaling resulted in a time series that contains parts that are comparably noisy to the correlated (unweighted) time series, which is unexpected when introducing the noise covariance matrix to the mass estimate. It is thought that this can be improved by treating the regularisation of the noise covariance matrix for each month (i.e. each data point of the time series) individually, because it was shown that outliers can be created when truncating inadequately.

Bibliography

G. A, J. Wahr, and S. Zhong. Computations of the viscoelastic response of a 3-d compressible Earth to surface loading: an application to glacial isostatic adjustment in Antarctica and Canada. *Geophysical Journal International*, 192(2):557–572, 2013. doi: 10.1093/gji/ggs030.

I. Amidror. Scattered data interpolation methods for electronic imaging systems: a survey. *Journal of Electronic Imaging*, 11(2):157–176, April 2002. doi: 10.1117/1.1455013.

H. Bader. Sorge's law of densification of snow on high polar glaciers. *Journal of Glaciology*, 2:319–323, 1954. doi: 10.1017/S0022143000025144.

J. L. Bamber. Ice sheet altimeter processing scheme. *International Journal Of Remote Sensing*, 15(4):925–938, 1994. doi: 10.1080/01431169408954125.

C. Bouzinac. Cryosat product handbook. Technical report, ESA, 2012.

A. C. Brenner, R. A. Blndschadler, R. H. Thomas, and H. J. Zwally. Slope-induced errors in radar altimetry over continental ice sheets. *Journal of Geophysical Research*, 88(C3):1617–1623, February 1983. doi: 10.1029/JC088iC03p01617.

B. Csatho, T. Schenk, C. Van Der Veen, and W. B. Krabill. Intermittent thinning of Jakobshavn isbræ, West Greenland, since the little ice age. *Journal of Glaciology*, 54(184):131—-144, 2008. doi: 10.3189/002214308784409035.

C. H. Davis. Surface and volume scattering retracking algorithm for ice sheet satellite altimetry. *Transactions on Geoscience and Remote Sensing*, 31:811–818, 1993. doi: 10.1109/36.239903.

C. H. Davis. A robust threshold retracking algorithm for measuring ice-sheet surface elevation change from satellite radar altimeters. *Transactions on Geoscience and Remote Sensing*, 35:974–979, 1997. doi: 10.1109/36.602540.

X. Deng and W. E. Featherstone. A coastal retracking system for satellite radar altimeter waveforms: Application to ers-2 around australia. *Journal of Geophysical Research*, 111(C06012), 2006. doi: 10.1029/2005JC003039.

S. DeWitt and H. Zell. Nasa's successful ice cloud and land elevation mission comes to an end, 2010. URL `https://www.nasa.gov/mission_pages/icesat/icesat-end.html`. [Last updated: 3rd of September, 2010].

S. L. Dingman. *Physical Hydrology*. Waveland Press, Inc., 3rd edition, 2015. ISBN 978-1-4786-1118-9.

P. Ditmar. AE4-E10: Inverse Problems - Lecture notes, February 2011.

P. Ditmar. CIE4610: Mass Transport in the Earth system - Lecture notes, June 2018a.

P. Ditmar. Conversion of time-varying stokes coefficients into mass anomalies at the Earth's surface considering the Earth's oblateness. *Journal of Geodesy*, Feb 2018b. ISSN 1432-1394. doi: 10.1007/s00190-018-1128-0.

P. Ditmar, N. Tangdamrongsub, J. Ran, and R. Klees. Estimation and reduction of random noise in mass anomaly time-series from satellite gravity data by minimization of month-to-month year-to-year double differences. *Journal of Geodynamics*, 119:9–22, 2018. doi: 10.1016/j.jog.2018.05.003.

ECMRWF. IFS Documentation - Cy33r1: Part IV: Physical Processes. Technical report, ECMRWF, June 2008.

ESA. Esa's living Earth programme, 2017. URL `http://www.esa.int/Our_Activities/Observing_the_Earth/The_Living_Planet_Programme/ESA_s_Living_Planet_Programme`.

ESA. Geographical mode mask, 2017. URL https://earth.esa.int/web/guest/missions/esa-operational-eo-missions/cryosat/content/-/asset_publisher/VeF6/content/geographical-mode-mask-7107.

J. Ettema, M. R. van den Broeke, E. van Meijgaard, W. J. van de Berg, J. L. Bamber, J. E. Box, and B. R. C. Higher surface mass balance of the Greenland ice sheet revealed by high-resolution climate modeling. *Geophysical Research Letters*, 36(12), June 2009. doi: 10.1029/2009GL038110.

L. Foresta, N. Gourmelen, P. F., P. Nienow, H. Björnsson, and A. Shepherd. Surface elevation change and mass balance of icelandic ice caps derived from swath mode CryoSat-2 altimetry. *Geophysical Research Letters*, 43(12):12138—12145, 2016. doi: 10.1002/2016GL071485.

L. Foresta, N. Gourmelen, F. Weissgerber, P. Nienow, J. J. Williams, A. Shepherd, M. R. Drinkwater, and S. Plummer. Heterogeneous and rapid ice loss over the patagonian ice fields revealed by CryoSat-2 swath radar altimetry. *Remote Sensing Environment*, 211:441–455, 2018. doi: https://doi.org/10.1016/j.rse.2018.03.041.

N. Galin, D. J. Wingham, R. Cullen, M. Fornari, W. H. F. Smith, and S. Abdalla. Calibration of the CryoSat-2 interferometer and measurement of across-track ocean slope. *IEEE Transactions on Geoscience and Remote Sensing*, 51(1):57–72, January 2012. doi: 10.1109/TGRS.2012.2200298.

K. A. Giles, S. W. Laxon, D. J. Wingham, D. W. Wallis, W. B. Krabill, C. J. Leuschen, D. McAdoo, S. S. Manizade, and R. K. Raney. Combined airborne laser and radar altimeter measurements over the fram strait in may 2002. *Remote Sensing of Environment*, 111(2-3):182–194, 2007. doi: 10.1016/j.rse.2007.02.037.

N. Gourmelen, M. J. Escorihuela, A. Shepherd, L. Foresta, A. Muir, A. Garcia-Mondejar, M. Roca, S. Baker, and M. R. Drinkwater. CryoSat-2 swath interferometric altimetry for mapping ice elevation and elevation change. *Adv. Space Res.*, November 2017. doi: https://doi.org/10.1016/j.asr.2017.11.014.

L. Gray, D. Burgess, L. Copland, R. Cullen, N. Galin, R. Hawley, and V. Helm. Interferometric swath processing of Cryosat data for glacial ice topography. *The Cryosphere*, 7:1857—1867, December 2013. doi: 10.5194/tc-7-1857-2013.

L. Gray, D. Burgess, L. Copland, M. N. Demuth, T. Dunse, K. Langley, and T. V. Schuler. CryoSat-2 delivers monthly and inter-annual surface elevation change for arctic ice caps. *The Cryosphere*, 9:1895—1913, 2015. doi: 10.5194/tc-9-1895-2015.

F. Göttle, D. Dettmering, F. L. Müller, and C. Schwatke. Lake level estimation based on CryoSat-2 SAR altimetry and multi-looked waveform classification. *Remote Sensing*, 8, 2016. doi: 10.3390/rs8110885.

R. L. Hawley, A. Shepher, R. Cullen, V. Helm, and D. J. Wingham. Ice-sheet elevations from across-track processing of airborne interferometric radar altimetry. *Geophysical Research Letters*, 36, 2009. doi: 10.1029/2009GL040416.

W. A. Heiskanen and H. Moritz. *Physical Geodesy*. W.H. Freeman and Company San Francisco, 1967 [reprint], 1993.

V. Helm, A. Humber, and H. Miller. Elevation and elevation change of Greenland and Antarctica derived from CryoSat-2. *The Cryosphere*, 8:1539–1559, 2014. doi: 10.5194/tc-8-1539-2014.

S. Holmes and W. Featherstone. A unified approach to the clenshaw summation and the recursive computation of very high degree and order normalised associated legendre functions. *Journal of Geodesy*, 76: 279–299, 2002. doi: 10.1007/s00190-002-0216-2.

I. Howat. MEaSUREs Greenland Ice Mapping Project (GIMP) Land Ice and Ocean Classification Mask (NSIDC-0714, Version 1), 2017.

I. Howat, A. Negrete, and B. Smith. MEaSUREs Greenland Ice Mapping Project (GIMP) Digital Elevation Model from GeoEye and WorldView Imagery (NSIDC-0715, version 1), 2017.

I. M. Howat, Y. Ahn, I. Joughin, M. R. van den Broeke, J. T. M. Lenaerts, and B. Smith. Mass balance of Greenland's three largest outlet glaciers, 2000–2010. *Geophysical Research Letters*, 38, 2011. doi: 10.1029/2011GL047565.

I. Howat, I. Joughin, and T. Scambos. Rapid changes in ice discharge from Greenland outlet glaciers. *Science*, 315:1559–1561, March 2007. doi: 10.1126/science.1138478.

R. T. W. L. Hurkmans, B. J. L. Bamber, L. S. Sørensen, I. R. Joughin, C. H. Davis, and W. B. Krabill. Spatiotemporal interpolation of elevation changes derived from satellite altimetry for Jakobshavn isbræ, Greenland. *Journal of Geophysical Research*, 117, 2012. doi: 10.1029/2011JF002072.

M. Huss. Density assumptions for converting geodetic glacier volume change to mass change. *The Cryosphere*, 7(3):877–887, 2013. doi: 10.5194/tc-7-877-2013.

IMAU. Regional climate model. URL `https://www.projects.science.uu.nl/iceclimate/models/racmo.php`.

C. Jekeli. *Treatise on Geophysics: Geodesy: Potential Theory and Static Gravity Field of the Earth*. Elsevier, 2007.

J. R. Jensen. Angle measurement with a phase monopulse radar altimeter. *IEEE Transactions on Antenna and Propagation*, 47(4):715–724, April 1999.

I. Joughin, W. Abdalati, and M. Fahnestock. Large fluctuations in speed on Greenland's Jakobshavn isbræ glacier. *Nature*, 432:608—610, 2004. doi: 10.1038/nature03130.

I. Joughin, B. E. Smith, I. M. Howat, D. Floricioiu, and R. B. Alley. Seasonal to decadal scale variations in the surface velocity of Jakobshavn isbrae, Greenland: Observation and model-based analysis. *Journal of Geophysical Research*, 117, 2012. doi: 10.1029/2011JF002110.

I. Joughin, B. E. Smith, I. M. Howat, T. Scambos, and T. Moon. Greenland flow variability from ice sheet-wide velocity mapping. *Journal of Glaciology*, 56(197):415–430, August 2010. doi: 10.3189/002214310792447734.

M. D. King, I. M. Howat, S. Jeong, M. J. Noh, B. Wouters, B. Nöel, and M. R. van den Broeke. Seasonal to decadal variability in ice discharge from the Greenland ice sheet (in review). *The Cryosphere Discussions*, 2018:1–28, 2018. doi: 10.5194/tc-2018-177.

K. W. Knowles. A mapping and gridding primer: Points, pixels, grids, and cells. unpublished report to the national snow and ice data center. Technical report, Boulder, 1993. URL `https://nsidc.org/ease/clone-ease-grid-projection-gt`.

P. Lacroix, M. Dechambre, B. Legrésy, F. Blarel, and F. Rémy. On the use of the dual-frequency ENVISAT altimeter to determine snowpack properties of the Antarctic ice sheet. *Remote Sensing of Environment*, 112: 1712–1729, 2008. doi: 10.1016/j.rse.2007.08.022.

A. Lemos, A. Shepherd, M. McMillan, A. E. Hogg, E. Hatton, and I. Joughin. Ice velocity of Jakobshavn isbræ, Petermann glacier, Nioghalvfjerdsfjorden, and Zachariæ isstrøm, 2015–2017, from Sentinel 1-a/b SAR imagery. *The Cryosphere*, 12:2087—-2097, November 2018. doi: https://doi.org/10.5194/tc-12-2087-2018.

H. Lentz, H.-M. Braun, M. Younis, C. Fischer, W. Wiesbeck, and C. Mavrocordatos. Concept and realization of an airborne SAR/interferometric radar altimeter system (ASIRAS). *Geoscience and Remote Sensing Symposium*, 6:399–401, November 2002.

E. Makhoul-Varona, F. Martin, M. Naeije, and P. Cotton. SCOOP: SAR altimetry coastal and open ocean performance [algorithm theoretical basis document (ATBD)]. Technical Report 1.5, ESA, September 2017. URL `http://www.satoc.eu/projects/SCOOP/docs/SCOOP_D1.3_ATBD_v15.pdf`.

C. F. Martin, W. B. Krabill, S. S. Manizade, R. L. Russell, J. G. Sonntag, R. N. Swift, and J. K. Yungel. Airborne topographic mapper calibration procedures and accuracy assessment. Technical report, NASA, February 2012. URL `https://ntrs.nasa.gov/archive/nasa/casi.ntrs.nasa.gov/20120008479.pdf`.

T. V. Martin, H. J. Zwally, A. C. Brenner, and R. A. Bindschadler. Analysis and retracking of continental ice sheet radar altimeter waveforms. *Journal of Geophysical Research*, 88(3):1608–1616, February 1983. doi: 10.1029/JC088iC03p01608.

T. Mayer-Gürr, S. Behzadpour, M. Ellmer, A. Kvas, B. Klinger, and N. Zehentner. ITSG-Grace2016 - Monthly and Daily Gravity Field Solutions from GRACE, 2016.

T. Mayer-Gürr, S. Behzadpour, M. Ellmer, A. Kvas, B. Klinger, and N. Zehentner. ITSG-Grace2018 - Monthly and Daily Gravity Field Solutions from GRACE, 2018.

M. McMillan, A. Leeson, A. Shepherd, K. Briggs, T. W. K. Armitage, A. Hogg, P. K. Munneke, M. van den Broeke, B. Noël, W. J. van de Berg, S. Ligtenberg, M. Horwath, A. Groh, A. Muir, and L. Gilbert. A high-resolution record of Greenland mass balance. *Geophysical Research Letters*, 43:7002—-7010, 2016. doi: 10.1002/2016GL069666.

G. Moholdt, C. Nuth, J. O. Hagen, and J. Kohler. Recent elevation changes of Svalbard glaciers derived from ICESat laser altimetry. *Remote Sensing of Environment*, 114(11):2756–2767, November 2010. doi: 10.1016/j.rse.2010.06.008.

G. Moholdt, L. Padman, and H. A. Fricker. Basal mass budget of ross and filchner-ronne ice shelves, Antarctica, derived from Lagrangian analysis of ICESat altimetry. *Journal of Geophysical Research: Earth Surface*, 119(11):2361–2380, November 2014. doi: 10.1002/2014JF003171.

T. Moon, I. Joughin, B. Smith, M. R. Broeke, W. J. Berg, B. Noël, and M. Usher. Distinct patterns of seasonal Greenland glacier velocity. *Geophysical Research Letters*, 41(20):7209–7216, 2014. doi: 10.1002/2014GL061836.

R. J. Motyka, M. Fahnestock, and M. Truffer. Volume change of Jakobshavn isbræ, West Greenland:1985–1997–2007. *Journal of Glaciology*, 56(198):635–646, 2010. doi: 10.3189/002214310793146304.

I. S. Muresan, S. A. Khan, A. Aschwanden, C. Khroulev, T. van Dam, J. Bamber, M. van den Broeke, B. Wouters, P. Kuipers Munneke, and K. H. Kjær. Modelled glacier dynamics over the last quarter of a century at jakobshavn isbræ. *The Cryosphere*, 10:597—-611, 2016. doi: 10.5194/tc-10-597-2016.

T. Nagler, H. Rott, M. Hetzenecker, J. Wuite, and P. Potin. The Sentinel-1 mission: New opportunities for ice sheet observations, 2015.

S. Nanda. Multiple scatterer retracking and interferometric swath processing of CryoSat-2 data for ice sheet elevation changes. Master's thesis, TU Delft, July 2015. URL `https://repository.tudelft.nl/islandora/object/uuid:abb749eb-2bb6-4acf-b7e7-e0526ff83532/?collection=research`.

K. Nielsen, S. A. Khan, G. Spada, J. Wahr, M. Bevis, L. Liu, and T. Dam. Vertical and horizontal surface displacements near Jakobshavn isbræ driven by melt-induced and dynamic ice loss. *Journal of Geophysical Research: Solid Earth*, 118(4):1837–1844, 2013. doi: 10.1002/jgrb.50145.

J. Nilsson. *Cryosphere Monitoring from Satellites and Aircrafts*. PhD thesis, Technical University of Denmark, January 2015.

J. Nilsson, P. Vallelonga, S. B. Simonsen, L. S. Sørensen, R. Forsberg, D. Dahl-Jensen, M. Hirabayashi, K. Goto-Azuma, C. S. Hvidberg, H. A. Kjær, and K. Satow. Greenland 2012 melt event effects on CryoSat-2 radar altimetry. *Geophysical Research Letters*, 42:3919—-3926, 2015. doi: 10.1002/2015GL063296.

J. Nilsson, A. Gardner, L. S. Sørensen, and R. Forsberg. Improved retrieval of land ice topography from CryoSat-2 and its impact for volume-change estimation of the Greenland ice sheet. *The Cryosphere*, 10:2953–2969, 2016. doi: 10.5194/tc-10-2953-2016.

B. Noël, W. J. van de Berg, J. M. van Wessem, E. van Meijgaard, D. van As, J. T. M. Lenaerts, S. Lhermitte, P. Kuipers Munneke, C. J. P. P. Smeets, L. H. van Ulft, R. S. W. van de Wal, and M. R. van den Broeke. Modelling the climate and surface mass balance of polar ice sheets using RACMO2 – part 1: Greenland (1958–2016). *The Cryosphere*, 12:811–831, 2018. doi: https://doi.org/10.5194/tc-12-811-2018.

C. Nuth, G. Moholdt, J. Kohler, J. O. Hagen, and A. Kääb. Svalbard glacier elevation changes and contribution to sea level rise. *Journal of Geophyiscal Research*, 115(F01008), 2010. doi: 10.1029/2008JF001223.

M. S. Pelto, T. J. Hughes, and H. H. Brecher. Equilibrium state of Jakobshavns isbræ, West Greenland. *Annals of Glaciology*, 12, 1989. doi: 10.1017/S0260305500007084.

J. Ran. *Analysis of mass variations in Greenland by a novel variant of the mascon approach*. PhD thesis, TU Delft, 2017.

J. Ran, P. Ditmar, R. Klees, and H. H. Farahani. Statistically optimal estimation of Greenland ice sheet mass variations from GRACE monthly solutions using an improved mascon approach. *Journal of Geodesy*, 92: 299–319, 2018. doi: 10.1007/z00190-017-1063-5.

R. K. Raney. The delay-doppler radar altimeter. *IEEE Transactions on Geoscience and Remote Sensing*, 36(5): 1578–1588, September 1998. doi: 10.1109/36.718861.

R. K. Raney. Cryosat SAR-mode looks revisited. *IEEE Geoscience and Remote Sensing Letters*, 9(3), 2012. doi: 10.1109/LGRS.2011.2170052.

G. Ratier, R. Francis, C. Mavrocordatos, and R. Zobl. The CryoSat system - the satellite and its radar altimeter. *ESA bulletin*, 122:12–20, 2005. URL `https://www.esa.int/About_Us/ESA_Publications/ESA_i_Bulletin_i_122_May_2005`.

J. Ray. IERS analysis campaign to investigate motions of the geocenter, IERS Tech. Note. Technical report, Central Bureau of IERS Observatioire de Paris, 1999.

G. Rees and W. G. Rees. *Physical principles of remote sensing*. Cambridge University Press, 2012.

J. K. Ridley and K. C. Partington. A model of satellite radar altimeter return from ice sheets. *Journal of Remote Sensing*, 9:601–624, 1988. doi: 10.1080/01431168808954881.

E. Rignot and J. Mouginot. Ice flow in Greenland for the international polar year 2008-2009. *Geophysical Research Letters*, 39(L11501), 2012. doi: 10.1029/2012GL051634.

M. Scagliola. Cryosat footprints. Technical report, ESA, June 2013.

M. Scagliola. Known biases in CryoSat level1b products. Technical report, ESA, January 2017. URL `https://wiki.services.eoportal.org/tiki-download_wiki_attachment.php?attId=4327&page=CryoSat%20Technical%20Notes&download=y`.

M. Scagliola. Test dataset of mispointing angles corrected for aberration of light. Technical report, ESA, January 2018. URL `https://earth.esa.int/web/guest/missions/esa-operational-eo-missions/cryosat/news/-/article/updated-cryosat-dataset-with-corrected-mispointing-angle-for-aberration-of-light`.

D. C. Slobbe, P. Ditmar, and R. C. Lindenbergh. Estimating the rates of mass change, ice volume change and snow volume change in Greenland from ICESat and GRACE data. *Geophysical Journal International*, 176 (1):95–106, January 2009. doi: 10.1111/j.1365-246X.8008.03978.x.

J. P. Snyder. Map projections - a working manual. Technical report, 1987.

T. Strozzi, A. Luckman, T. Murray, U. Wegmuller, and C. L. Werner. Glacier motion estimation using SAR offset-tracking procedures. *IEEE Transactions on Geoscience and Remote Sensing*, 40(11):2384–2391, November 2002. doi: 10.1109/TGRS.2002.805079.

Y. Sun, R. Riva, and P. Ditmar. Optimizing estimates of annual variations and trends in geocenter motion and j2 from a combination of GRACE data and geophysical models. *Journal of Geophysical Research*, 121(11): 8352–8370, 2016. doi: 10.1002/2016JB013073.

B. D. Tapley and S. Bettadpur. The gravity recovery and climate experiment: Mission overview and early results. *Geophysical Research Letters*, 31, 2004. doi: 10.1029/2004GL019920.

R. Thomas, E. Frederick, W. Krabill, S. Manizade, and C. Martin. Progressive increase in ice loss from Greenland. *Geophysical Research Letters*, 33(10):L10503, 2006. doi: 10.1029/2006GL026075.

M. R. van den Broeke, E. M. Enderlin, I. M. Howat, P. Kuipers Munneke, B. P. Y. Noël, W. J. van de Berg, E. van Meijgaard, and B. Wouters. On the recent contribution of the Greenland ice sheet to sea level change. *The Cryosphere*, 10:1933—-1946, 2016. doi: 10.5194/tc-10-1933-2016.

T. Vincenty. Direct and inverse solutions of geodesics on the ellipsoid with application of nested equations. *Survey Review*, 23(176):88–93, 1975. doi: 10.1179/sre.1975.23.176.88.

J. Wahr, M. Molenaar, and F. Bryan. Time variability of the Earth's gravity field: Hydrological and oceanic effects and their possible detection using GRACE. *Journal of Geophysical Research*, 103(12):205–229, December 1998. doi: https://doi.org/10.1029/98JB02844.

L. M. Wake, B. S. Lecavalier, and M. Bevis. Glacial Isostatic Adjustment (GIA) in Greenland: a review. *Current Climate Change Reports*, 2(3):101–111, September 2016. doi: 10.1007/s40641-016-0040-z.

X. Wang and D. M. Holland. A method to calculate elevation-change rate of Jakobshavn isbrae using Operation IceBridge Airborne Topographic Mapper data. *IEEE*, PP(99), 2018. doi: 10.1109/LGRS.2018.2828417.

F. Weissgerber. *Traitements cohérents d'images RSO multi-modes multi-resolutions pour la caractérisation du milieu urbain*. PhD thesis, Paris Institute of Technology, November 2017. URL `https://tel.archives-ouvertes.fr/tel-01481528/document`.

F. Weissgerber and N. Gourmelen. Crypotop evolution: utiliser la pseudo-fauchée de CryoSat-2 pour rafiner la résolution des mne et des cartes de taux de changements d'élévation. *Gretsi*, September 2017. URL `https://hal.archives-ouvertes.fr/hal-01647175`.

D. J. Wingham, C. G. Rapley, and H. Griffiths. New techniques in satellite altimeter tracking systems. *Proceedings of IGARSS' 86 Symposium.*, pages 1339–1344, 1986.

D. J. Wingham et al. Cryosat: A mission to determine the fluctuations in Earth's land and marine ice fields. *Adv. Space Res.*, 37:841–871, 2006. doi: 10.1016/j.asr.2005.07.027.

B. Wouters, J. A. Bonin, D. P. Chambers, R. E. M. Riva, I. Sasgen, and J. Wahr. Grace, time-varying gravity, Earth system dynamics and climate change. *Report on Progress in Physics*, 77(11), October 2014. doi: 10.1088/0034-4885/77/11/116801.

B. Wouters, A. Martin-Espanol, V. Helm, T. Flament, J. M. van Wessem, S. R. M. Ligtenberg, M. R. van den Broeke, and J. L. Bamber. Dynamic thinning of glaciers on the Southern Antarctic peninsula. *Science*, 348 (6237):899–903, May 2015. doi: 10.1126/science.aaa5727.

X. Wu, J. Ray, and T. van Dam. Geocenter motion and its geodetic and geophysical implications. *Journal of Geodynamics*, 58:44–61, 2012. doi: 10.1016/j.jog.2012.01.007.

H. Zell. Icebridge - aircraft, instruments, satellites, 2017a. URL `https://www.nasa.gov/mission_pages/icebridge/instruments/index.html`. [Last updated: 31st of August, 2017].

H. Zell. Icebridge mission overview, 2017b. URL `https://www.nasa.gov/mission_pages/icebridge/mission/index.html`. [Last updated: 31st of August, 2017].

H. Zell. Icebridge past campaigns, 2017c. URL `https://www.nasa.gov/mission_pages/icebridge/news/past.html`. [Last updated: 31st of August, 2017].

H. J. Zwally, M. B. Giovinetto, M. A. Beckley, and J. L. Saba. Antarctic and Greenland drainage systems, 2012. URL `http://icesat4.gsfc.nasa.gov/cryo_data/ant_grn_drainage_systems.php`.

A

Appendix

A.1. Least Squares Estimation

Suppose an $m \times 1$ observations in vector $\mathbf{y}$ and $n \times 1$ model parameters in $\mathbf{x}$, related via an $m \times n$ model matrix A according to:

$$\mathbf{y} = A\mathbf{x}, \tag{A.1}$$

where vector $\mathbf{x}$ is unknown. Finding find the model parameters that correspond to our observations best is commonly done in a least squares sense. This can be done by minimising the magnitude of the residuals via:

$$\mathbf{r} = \mathbf{y} - A\hat{\mathbf{x}}, \tag{A.2}$$

where $\mathbf{r}$ is the misfit of the chosen model with estimated model parameters $\hat{\mathbf{x}}$. Minimising a magnitude is analytically achievable by setting the derivative with respect to $\hat{\mathbf{x}}$ of equation A.2 to be zero. Minimisation of the squared form $\mathbf{r}$ is then:

$$\begin{aligned} \frac{\partial \mathbf{r}^T \mathbf{r}}{\partial \hat{\mathbf{x}}} &= \frac{\partial}{\partial \hat{\mathbf{x}}} (\mathbf{y} - A\hat{\mathbf{x}})^T (\mathbf{y} - A\hat{\mathbf{x}}) = 0 \\ 0 &= \frac{\partial}{\partial \hat{\mathbf{x}}} (\mathbf{y}^T \mathbf{y} - \mathbf{y}^T A\hat{\mathbf{x}} - \hat{\mathbf{x}}^T A^T \mathbf{y} + \hat{\mathbf{x}}^T A^T A\hat{\mathbf{x}}), \end{aligned} \tag{A.3}$$

where it can be seen that $\mathbf{y}^T\mathbf{y}$ is not a function of $\hat{\mathbf{x}}$ and that $\hat{\mathbf{x}}^T A^T \mathbf{y} = \mathbf{y}^T A\hat{\mathbf{x}}$, such that equation A.3 simplifies to:

$$\begin{aligned} 0 &= \frac{\partial}{\partial \hat{\mathbf{x}}} (-\mathbf{y}^T A\hat{\mathbf{x}} - (\hat{\mathbf{x}}^T A^T \mathbf{y})^T + \hat{\mathbf{x}}^T A^T A\hat{\mathbf{x}}) \\ &= \frac{\partial}{\partial \hat{\mathbf{x}}} (-2\mathbf{y}^T A\hat{\mathbf{x}} + \hat{\mathbf{x}}^T A^T A\hat{\mathbf{x}}). \end{aligned} \tag{A.4}$$

Writing out the derivative with respect to $\hat{\mathbf{x}}$:

$$\begin{aligned} 0 &= -2(\mathbf{y}^T A)^T + 2A^T A\hat{\mathbf{x}} \\ A^T \mathbf{y} &= A^T A\hat{\mathbf{x}} \\ (A^T A)^{-1} A^T \mathbf{y} &= \hat{\mathbf{x}} \end{aligned} \tag{A.5}$$

which is the *normal equation*. The derivation is analogous for a weighted LSE (WLSE). For a WLSE, $\mathbf{r}^T W \mathbf{r}$ is minimised instead of $\mathbf{r}^T \mathbf{r}$, which leads to:

$$(A^T W A)^{-1} A^T W \mathbf{y} = \hat{\mathbf{x}}, \tag{A.6}$$

where W is a *square weighting matrix* of dimensions $m \times m$. If W is a full matrix containing the inverse co-variances of $\mathbf{y}$, then W is denoted as Q_{yy}^{-1} and the LSE is the *Best Linear Unbiased Estimator* (BLUE, Gauss-Markov Theorem).
The addition of the noise covariance matrix Q_{yy} to the normal equation for data inversion (example: 3.16) can

be considered as an unweighted inversion after decorrelating the design matrix and observation separately, i.e.

$$\begin{cases} \tilde{A} = Q_{yy}^{-\frac{1}{2}} A, \\ \tilde{y} = Q_{yy}^{-\frac{1}{2}} y, \end{cases} \tag{A.7}$$

where $\tilde{A}$ and $\tilde{y}$ are the decorrelated design matrix and the decorrelated observation vector, respectively [Ditmar, 2011].

A.2. Waveform sample selection based on R [Weissgerber and Gourmelen, 2017]

Weissgerber and Gourmelen [2017] and Foresta et al. [2018] showed that reasonable elevation estimates can be obtained using the phase difference only instead of coherence for sample selection. The method essentially selects the samples within smooth parts of the phase difference measurements within each waveform. The phase difference measurements are referred to as $\Delta\phi$. An instructive example for finding suitable samples within one waveform based on the information provided by Weissgerber and Gourmelen [2017] and Foresta et al. [2018] is given below.

1. Divide the waveform in windows of $N = 64$ samples with 32 samples overlap.
2. Restore the full signal with unit amplitude for each window via $s = e^{i\Delta\phi}$, where i equals $\sqrt{-1}$.
3. Estimate slope of the full signal in each window using the FFT ($f = \frac{d\Delta\phi}{dn}$).
4. Create a new set of linear phase differences using the estimated slope for each window.
5. Subtract the new linear phase differences from the observed phase differences in each window.
6. Restore the full signal with unit amplitude using the subtracted phase differences: $s_{new} = e^{i\Delta(\Delta\phi)}$, where $\Delta(\Delta\phi)$ is the subtracted phase.
7. Compute dispersion measure $R = \frac{1}{N}|\sum_{n=1}^{N} s_{new}|$, where R is the phase difference dispersion and n is the sample number.
8. Discard the lowest estimate of R for each overlapping window, such that only one estimate per 32 samples is left. A low R corresponds to high dispersion and vice versa.
9. Select all samples within a window with R>0.95 and discard the rest.

A.3. Leakage and zero-padding

In section 2.3.1.2, the FFT is used to estimate the slopes of the phase difference values. Because this is applied to finite windows, this step is more accurately described by a *sliding discrete Fourier transform* (SDFT). When applying the FFT for slope estimation, it is of great importance to consider zero-padding the input (windowed phase differences). The slope of the input phase differences is assumed equal to the dominant amplitude in the amplitude spectrum of the unit complex signal ($e^{i\Delta\phi}$ with phase difference values ($\Delta\phi$). The amplitude spectrum however, can only display discrete frequencies limited by the signal length. It is highly unlikely that the present slope is among the discrete frequencies. As a consequence, *leakage* of the energy towards neighbouring discrete frequencies takes place. To mitigate the leakage and improve the slope estimate, *zero-padding* can be applied to the FFT input signal. To illustrate, assume that the signal with fixed time is contained in a recording of N samples. The sampling frequency is then $\frac{2\pi}{N}$. In case of zero-padding, the length of the signal is expanded such that the sampling frequency becomes finer.

A.4. On (differential) phase ambiguities

To understand phase measurements and its inherent presence of ambiguity, it is helpful to think of the phase as follows. Let us say a person is looking at a clock with only a minute hand. Every now and then the person is looking at it to check the time. Knowing that once the minute hand reaches 59, it starts again at 0 one minute later. In that case, an hour has to be added to the current time. Now say that this person is going to sleep at a time when the minute hand is at 50. Next, the person wakes up with the minute hand at 39. There is no way

of knowing how many hours have passed during the night's sleep. This is because keeping check of the time in this case only goes well as long as the person does not leave intervals longer than an hour between each check (anecdote inspired by R. Hanssen).
This is analogous to the phase ambiguity of CryoSat-2's double antenna phase difference measurements. A harmonic signal with an ambiguity, not at 60 minutes, but at $-\pi$ and π is measured. In addition, it is in this case impossible to retrieve the previous number cycles (analogous to the number of hours that have passed before). However, it is known that the real answer is within 0 to N times 2π added or subtracted to the actual measurement. In the anecdote, this comes down to 39 minutes past the hour plus 0 to N hours. Following the terminology used in this report; wrapping occurs at $-\pi$ and π (or 0 and 60 minutes if time can go back and forth). Because of the occurrence of wrapping, the measured value phase or minutes is said to be ambiguous.

A.5. Sensitivity to ascending/descending observations

It was found by Gray et al. [2013] that computed elevations show a discrepancy when observed in an ascending with respect to a descending track. Therefore, the sensitivity of elevation change estimates to ascending and descending observations is investigated. The elevation change estimates are made the same way as described in chapter 2. However, two ensembles of elevation change estimates are made, i.e. only using elevations obtained in ascending track and only using elevations obtained in descending track. To avoid an increasing number of empty grid cells, a 500 × 500 m^2 grid cell size is used instead of 250 × 250 m^2. The difference between the two elevation change sets is shown in figure A.1 below.

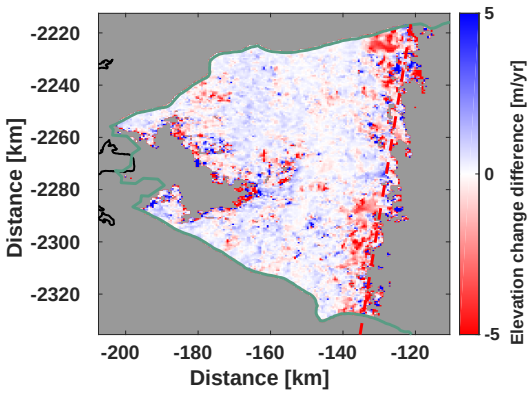

Figure A.1: Elevation change difference between estimates of observations in ascending and descending track. Grid cells are 500 × 500 m^2. Difference is calculated as $\frac{dh_{asc}}{dt} - \frac{dh_{desc}}{dt}$.

Near the mode boundary, elevation changes observed in descending track are predominantly more positive than elevation changes observed in ascending track. In contrast, the elevation changes between the terminus and mode boundary show more positive elevation changes observed in ascending track than elevation changes observed in descending track.

A.6. Elevation estimates from WLSE

In section 2.3.3.1 a WLSE is used to calculate the elevation change. Simultaneously, an estimate is made for the elevation, which is represented by a_0 in equation 2.13. This additional product can be averaged per grid cell of 250 × 250 m^2 to obtain a CryoSat-2 derived DEM (see figure A.2a).

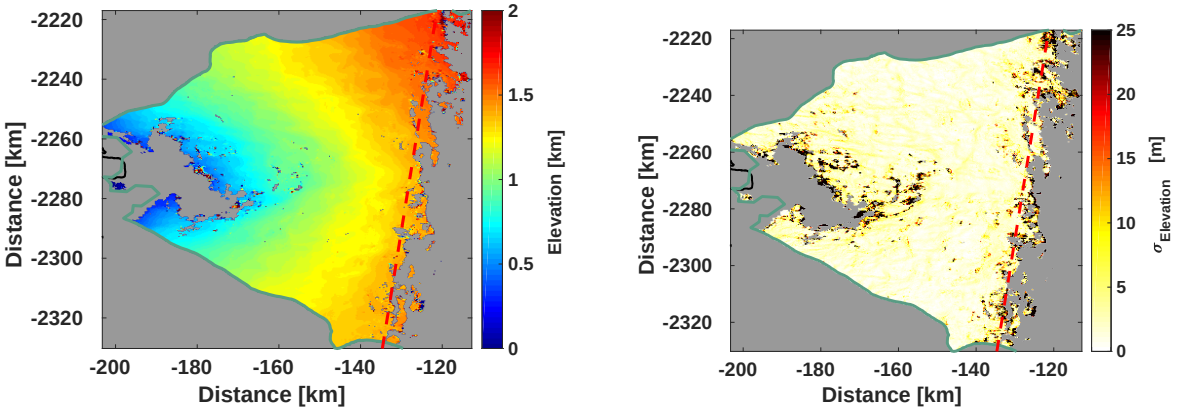

(a) Elevation estimates.

(b) Standard deviation of elevation estimates within each grid cell

Figure A.2: Elevation estimate in the Jakobshavn drainage basin at 250 m resolution. Elevation is given with respect to the WGS84 reference ellipsoid. A more accurate elevation model can be made by including the slope and curvature terms from equation 2.13. For this comparison, only the static elevation term was used.

The elevations in figure A.2a can then be compared to the DEM which was used to resolve the phase ambiguity (Howat [2017]). This DEM (90 × 90 m^2) is interpolated to the grid cell centres using natural neighbour interpolation [Amidror, 2002]. When subtracting the DEM elevations from the CryoSat-2 elevations, it is expected that the overall result is negative. After subtraction, figure A.3 is obtained, which shows regional thinning.

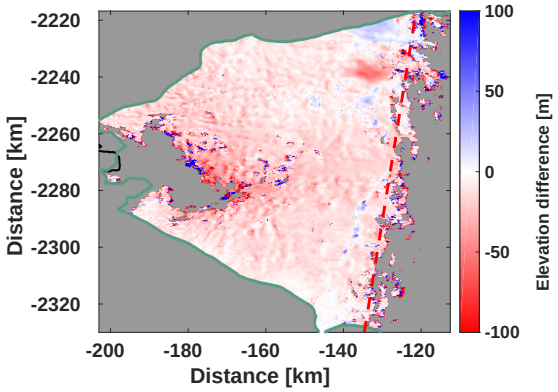

Figure A.3: Elevation difference between the DEM [Howat et al., 2017] and CryoSat-2 elevations. The difference is calculated using $\Delta h = h_{CS-2} - h_{DEM}$. Negative differences indicate ablation and positive differences indicate accumulation. Notice that the differences clipped to the colour bar minimum and maximum correspond to high standard deviations in figure A.2b.

Figure A.3 show that large elevations differences alternate with near 0 m elevation differences. Additionally, two distinct anomalies of opposite sign are visible in the North-East. These patterns may be a consequence of displacing topographic features. The smoothest parts within this field correspond to the highest flow velocities in figure A.19, which are in the order of km/yr. Displacing features causing elevation changes can be resolved using a Lagrangian approach of a flow field instead of Eulerian (see recommendations).

A.7. Effective density of the linear density model

In section 2, it is assumed that the effective density lies between that of snow and ice. The equation is first rewritten via:

$$\begin{aligned}\Delta M &= \Delta V \cdot \rho_{eff} \\ &= \Delta V_{ice} \cdot \rho_{ice} + \Delta V_{snow} \cdot \rho_{snow} \\ &= (\Delta V - \Delta V_{snow}) \cdot \rho_{ice} + \Delta V_{snow} \cdot \rho_{snow} \\ &= \Delta V \cdot \rho_{ice} + \Delta V_{snow} \cdot (\rho_{snow} - \rho_{ice}),\end{aligned} \tag{A.8}$$

where ΔM is the total mass change, ΔV the total volume change, ΔV_{ice} the ice volume change, ΔV_{snow} the snow volume change, ρ_{eff} the effective density, ρ_{ice} the density of ice and ρ_{snow} the density of snow. Combining the right-hand-side of the first and last line shows:

$$\rho_{eff} = \rho_{ice} + \frac{\Delta V_{snow}}{\Delta V} \cdot (\rho_{snow} - \rho_{ice}). \tag{A.9}$$

Which indicates that:

$$\rho_{eff} > \rho_{ice} \quad \text{if} \quad \frac{\Delta V_{snow}}{\Delta V} < 0. \tag{A.10}$$

Which is false when $\Delta V < 0$, $\Delta V_{snow} > 0$ such that $\Delta V_{ice} < -\Delta V_{snow}$. Or, when $\Delta V > 0$, $\Delta V_{snow} < 0$ such that $\Delta V_{ice} > -\Delta V_{snow}$.

A.8. Geodetic, geocentric and local coordinates

Geodetic latitude and longitude (WGS84) and polar stereographic north coordinates (EPSG3413) can be converted into one another with the procedure described below. For Greenland, the true latitude and longitude are set to 70° N and 0°, respectively. Details of the dimensions and properties of the Earth are given in table A.1.

Table A.1: Geodetic parameters of the WGS84 ellipsoid.

Parameter	**Symbol [unit]**	**Value**
Mean radius	R_m [m]	6371008.771415059
Semi-major axis	a [m]	6378137
Semi-minor axis	b [m]	6356752.31424518
Eccentricity	e [-]	$\sqrt{2f - f^2}$
Flattening of the Earth's figure	f [-]	298.257223563^{-1}
Longitude	λ or ϕ [°]	$[0 - 360\rangle$
Geodetic latitude	θ_g [°]	$[-90, 90]$
Geocentric latitude	θ_c [°]	$[-90, 90]$
Earth's average density	ρ_{avg} [kg/m^3]	5514
Earth's mass	M_E [kg]	5.9722×10^{24}

The algorithm below was taken from Snyder [1987]. θ_g is denoted as θ for convenience.

$$\begin{aligned}x &= \chi \cdot \rho \cdot \sin(\phi - \phi_0) \\ y &= -\chi \cdot \rho \cdot \cos(\phi - \phi_0),\end{aligned} \tag{A.11}$$

where x and y are the map coordinates in a plane with true a true latitude of ϕ_0 degrees North.

$$\chi = \begin{cases} -1 & \text{, if } \theta < 0 \\ 1 & \text{, if } \theta \geq 0, \end{cases} \tag{A.12}$$

where χ is an operator changing signs for calculations of coordinates on the northern and southern hemisphere.

$$\rho = \frac{\chi \cdot a \cdot \cos\theta_0}{\sqrt{1 - e^2 \cdot \sin^2\theta_0}} \cdot \frac{t}{t_c}, \tag{A.13}$$

where t and t_c are described as in equation A.14.

$$\begin{aligned} t &= \tan\left(\frac{\pi}{4} - \frac{\chi \cdot \theta}{2}\right) \cdot \left(\frac{1 + e \cdot \sin\theta}{1 - e \cdot \sin\theta}\right)^{\frac{e}{2}} \\ t_c &= \tan\left(\frac{\pi}{4} - \frac{\chi \cdot \theta_0}{2}\right) \cdot \left(\frac{1 + e \cdot \sin\theta_0}{1 - e \cdot \sin\theta_0}\right)^{\frac{e}{2}} \end{aligned} \tag{A.14}$$

The inverse procedure requires iterations or series expansion to solve for θ. Please refer to Snyder [1987] for a more detailed description.

Geocentric latitude
For some calculations the geodetic co-latitude is preferred over the geodetic latitude. These can be calculated as follows:

$$\begin{cases} \theta_{co-g} &= 90 - \theta_g \\ \theta_g &= 90 - \theta_{co-g}. \end{cases} \tag{A.15}$$

The calculation of a geocentric co-latitude (θ_{co-c}) from a geodetic co-latitude (θ_{co-g}) is described in equation A.16 [Ditmar, 2018b]:

$$\theta_{co-c} = \arctan 2\left(\frac{\sin\theta_{co-g}}{(1-f^2)\cos\theta_{co-g}}\right), \tag{A.16}$$

where $\arctan 2(...)$ is the four-quadrant inverse tangent. In the case of co-latitudes on the northern hemisphere, the inverse method is described with:

$$\theta_{co-g} = \arctan\Big((1-f)^2 \tan(\theta_{co-c} + \pi)\Big). \tag{A.17}$$

A.9. On the synthesis of the gravitational potential

The synthesis of the gravitational potential and surface density anomaly is performed using a set of orthogonal basis functions, i.e. the normalised surface spherical harmonics. The meaning of Stokes' coefficients can be uncovered by drawing parallels between this method and other mathematical applications using orthogonal basis functions.
The Stokes' coefficients can be considered as magnitudes within a spectrum, analogous to Fourier analysis on a plane. The spectrum however, is a Legendre spectrum where, in case of equation 3.1, the magnitude of the coefficients refer to the potential at radius $\tilde{R}$ [Jekeli, 2007].
Alternatively, the orthogonal basis functions can be considered as eigenfunctions with Stokes' coefficients as corresponding eigenvalues [Jekeli, 2007].

Higher degree surface spherical harmonics reveal variations at shorter wavelengths (higher frequencies). Equation 3.1 displays *downward continuation* to solve the Laplace equation at a given distance from the observation point outside (above) the gravitational field source (Earth). Accordingly, the standard deviation per degree (degree amplitude) of the functional that is displaced downward experiences a scaling by $\left(\frac{H_{sat}+\tilde{R}}{\tilde{R}}\right)^{l+1}$ [Ditmar, 2018a], where H_{sat} is the satellite altitude. Therefore, high degree coefficients experience higher noise levels for a constant numerator than low degree coefficients.

A.10. Figures

A.10.1. Maps of Greenland

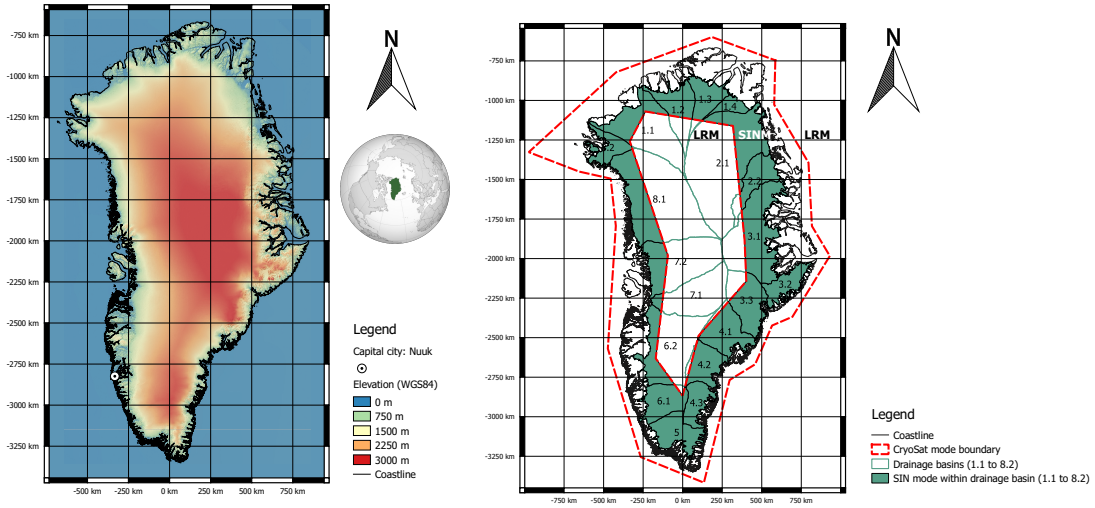

(a) (b)

Figure A.4: Maps of Greenland of the elevation (a) and basin boundaries (b). *Figure a) Elevation data taken from Howat et al. [2017] (90 m resolution). Globe taken from* `https://en.wikipedia.org/wiki/Greenland`. *Figure b) Mode boundaries taken from ESA. Drainage basin division taken from Zwally et al. [2012].*

A.10.2. Distributions of elevation difference for different waveform parameters for 6 drainage basins

Parameter optimisation in section 2.3.2 was performed on observations during April 2014 for 6 drainage basins (see figure A.4b). In the subsections below, the distributions of points of sample power, look angle, coherence, PD dispersion and slope as a function of elevation difference with the DEM is shown.

Sample power

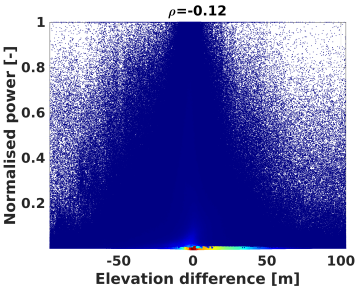

(a) Drainage basin 1.2.

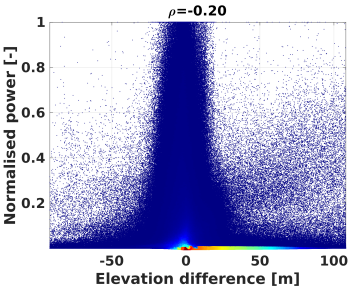

(b) Drainage basin 1.4.

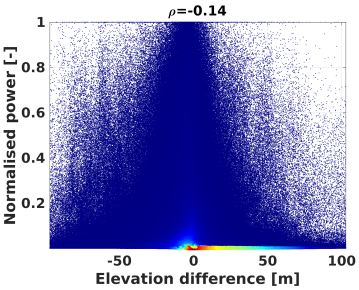

(c) Drainage basin 2.4.

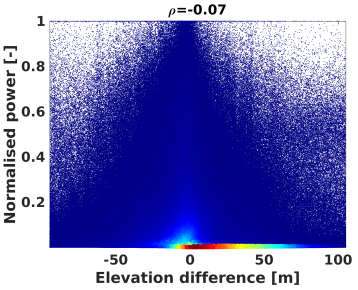

(d) Drainage basin 4.3.

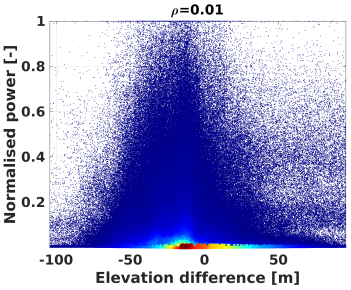

(e) Drainage basin 7.1.

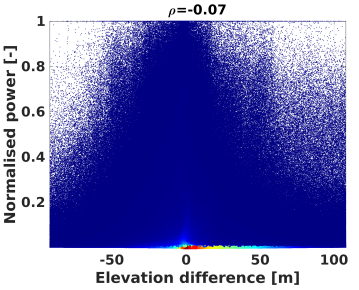

(f) Drainage basin 8.2.

Figure A.5: Scatter plots of the sample power of the dataset described in section 2.3.2, i.e. nearly all observations during April 2014 for different drainage basins.

Look angle

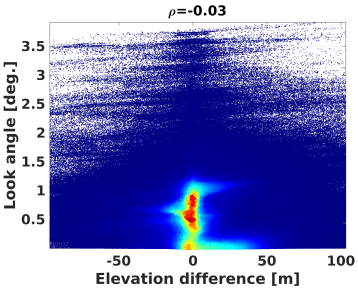

(a) Drainage basin 1.2.

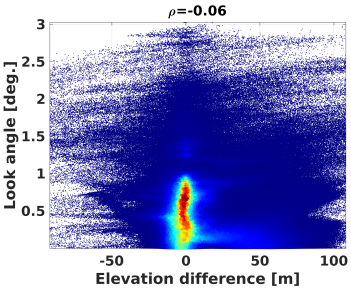

(b) Drainage basin 1.4.

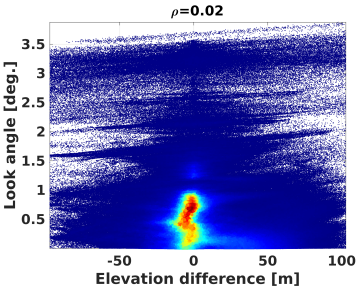

(c) Drainage basin 2.4.

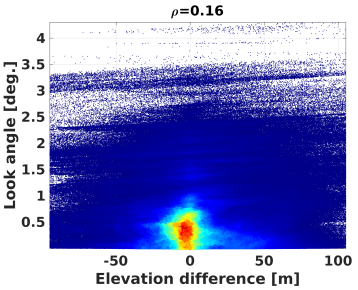

(d) Drainage basin 4.3.

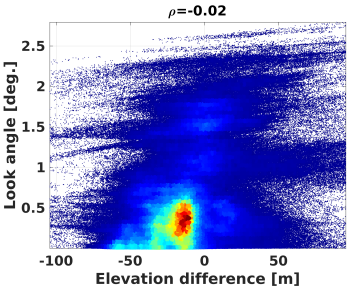

(e) Drainage basin 7.1.

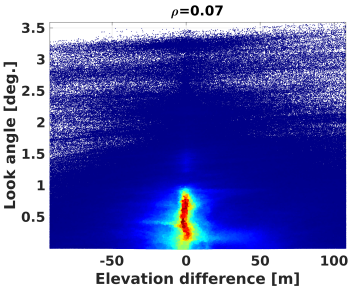

(f) Drainage basin 8.2.

Figure A.6: Scatter plots of the sample look angle of the dataset described in section 2.3.2, i.e. nearly all observations during April 2014 for different drainage basins. The correlation was calculated using the absolute elevation difference.

Coherence

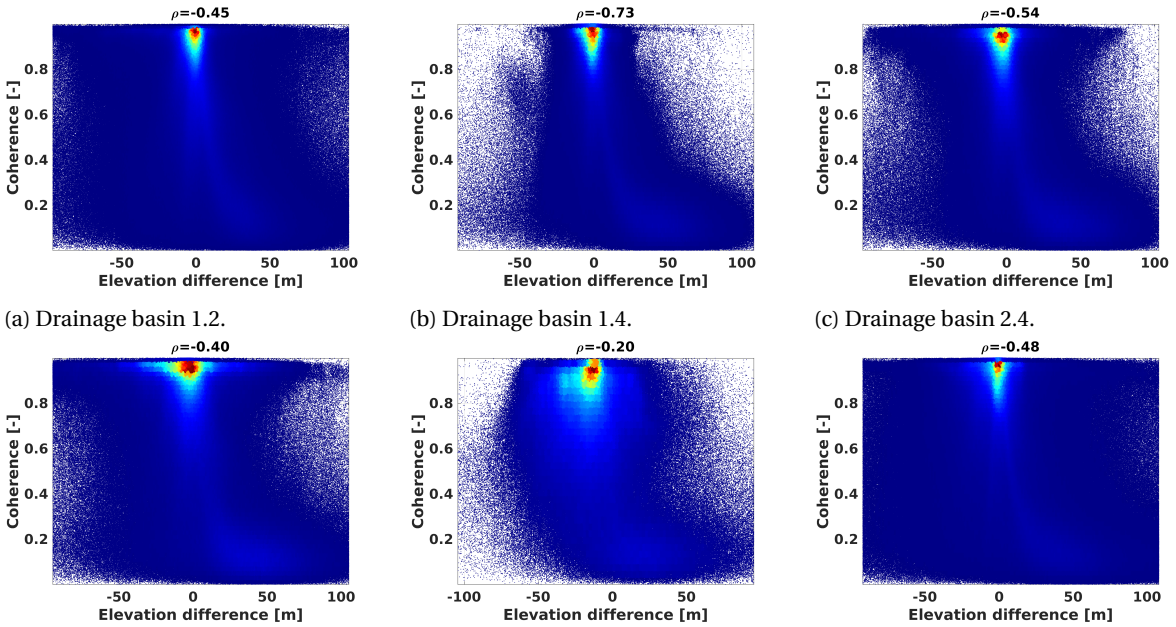

(a) Drainage basin 1.2. (b) Drainage basin 1.4. (c) Drainage basin 2.4.

(d) Drainage basin 4.3. (e) Drainage basin 7.1. (f) Drainage basin 8.2.

Figure A.7: Scatter plots of the sample coherence of the dataset described in section 2.3.2, i.e. nearly all observations during April 2014 for different drainage basins. The correlation was calculated using the absolute elevation difference.

PD dispersion

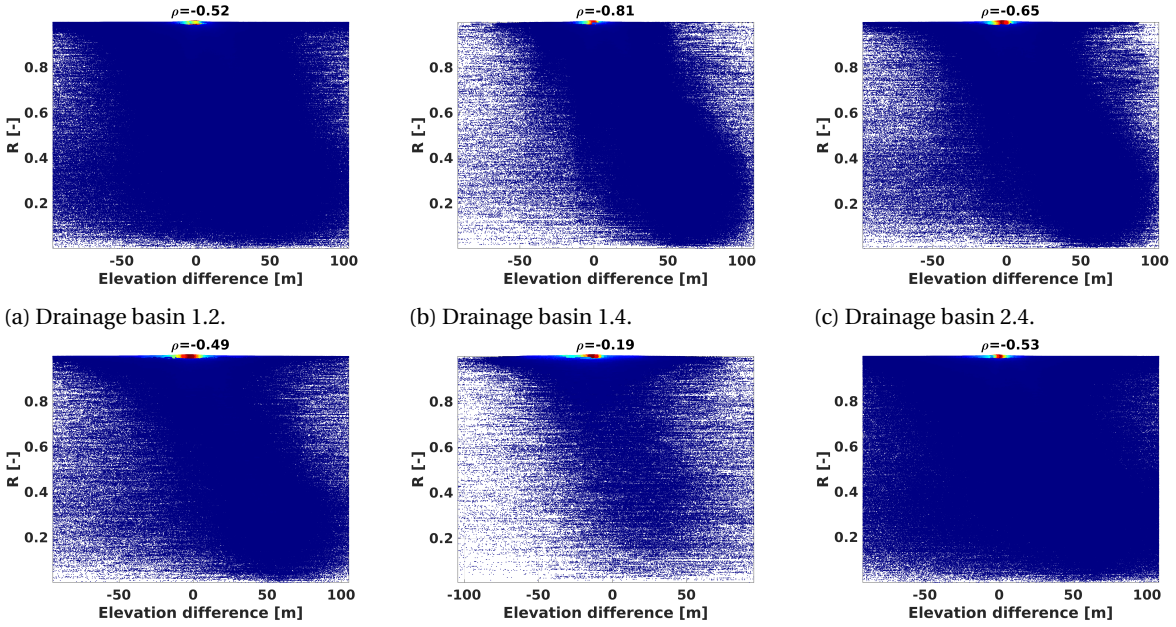

(a) Drainage basin 1.2. (b) Drainage basin 1.4. (c) Drainage basin 2.4.

(d) Drainage basin 4.3. (e) Drainage basin 7.1. (f) Drainage basin 8.2.

Figure A.8: Scatter plots of the sample PD dispersion of the dataset described in section 2.3.2, i.e. nearly all observations during April 2014 for different drainage basins. The correlation was calculated using the absolute elevation difference.

Slope

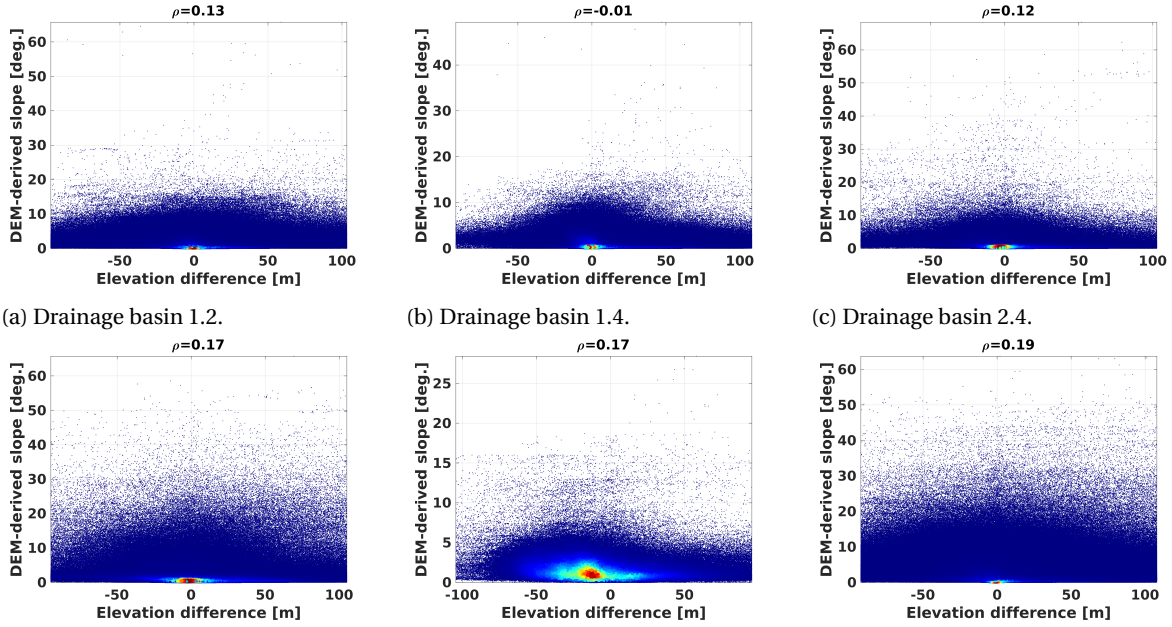

(a) Drainage basin 1.2.

(b) Drainage basin 1.4.

(c) Drainage basin 2.4.

(d) Drainage basin 4.3.

(e) Drainage basin 7.1.

(f) Drainage basin 8.2.

Figure A.9: Scatter plots of the sample slope of the dataset described in section 2.3.2, i.e. nearly all observations during April 2014 for different drainage basins. The correlation was calculated using the absolute elevation difference.

A.10.3. Parameter selection

Parameter optimisation was performed by minimising $min(\frac{\sigma}{log_{10}(N)})$ for the following parameters: normalised waveform energy, look angle and coherence or PD dispersion (R). To that end, σ, $log_{10}(N)$ and $min(\frac{\sigma}{log_{10}(N)})$ are shown below for these (combined) parameters.

Normalised waveform energy

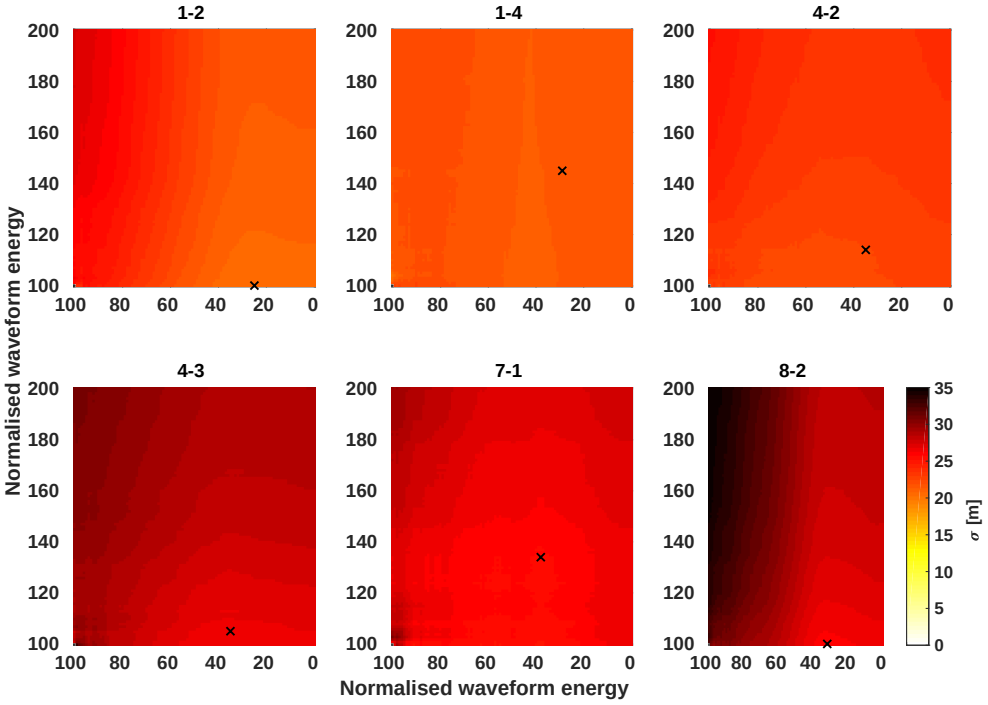

Figure A.10: Impact of variation of a normalised waveform energy threshold on the standard deviation for different drainage basins.

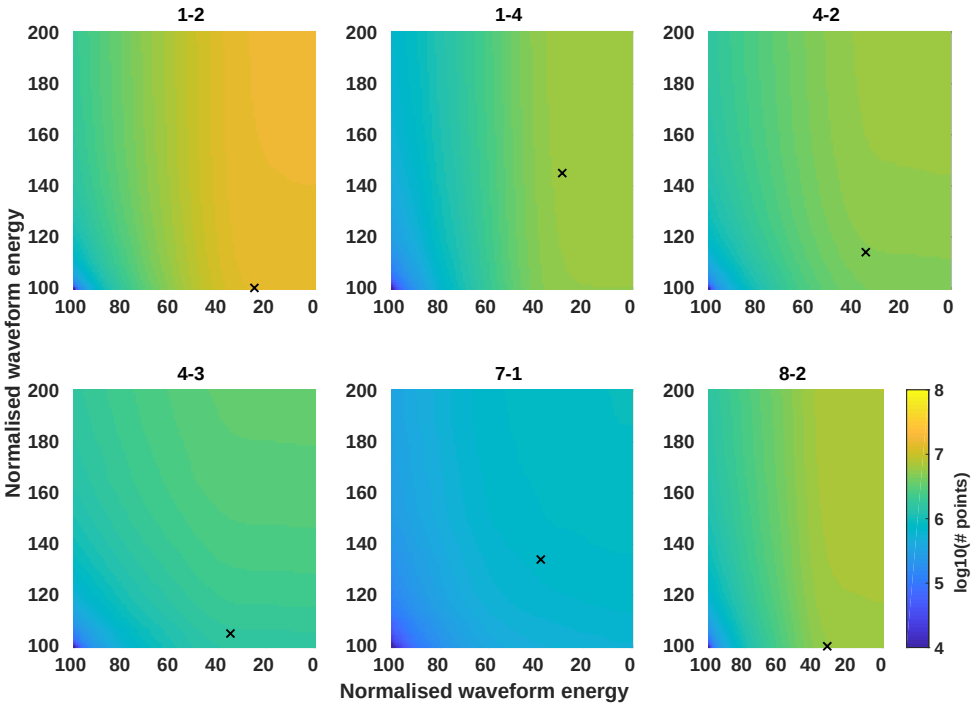

Figure A.11: Impact of variation of a normalised waveform energy threshold on the number of available points for different drainage basins.

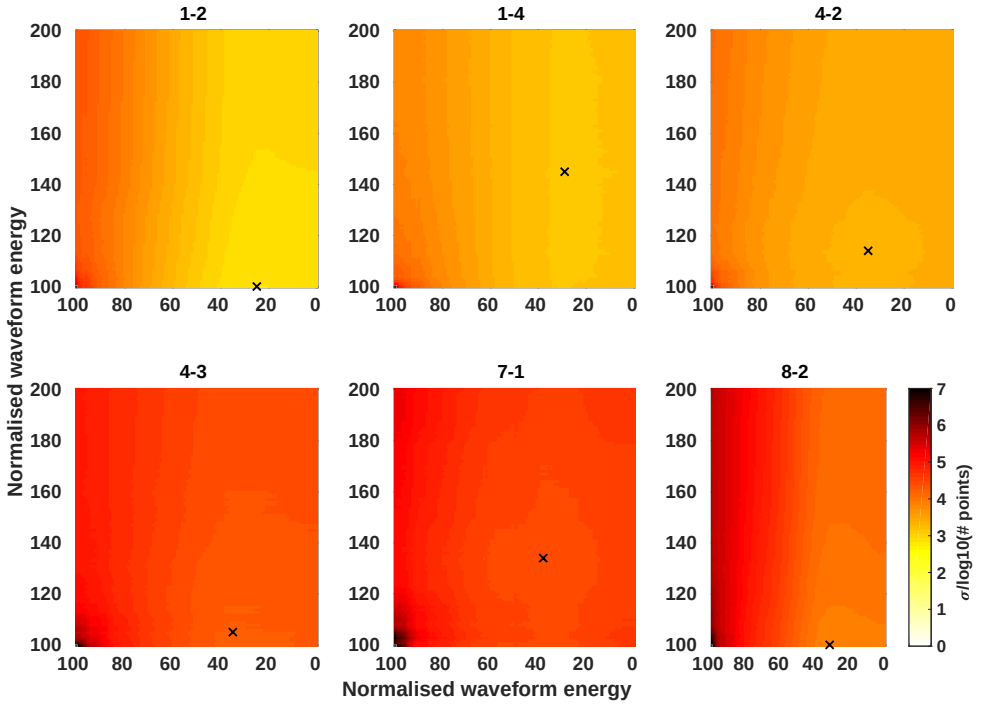

Figure A.12: Impact of variation of a normalised waveform energy threshold on the optimisation criterion for different drainage basins.

Coherence versus look angle

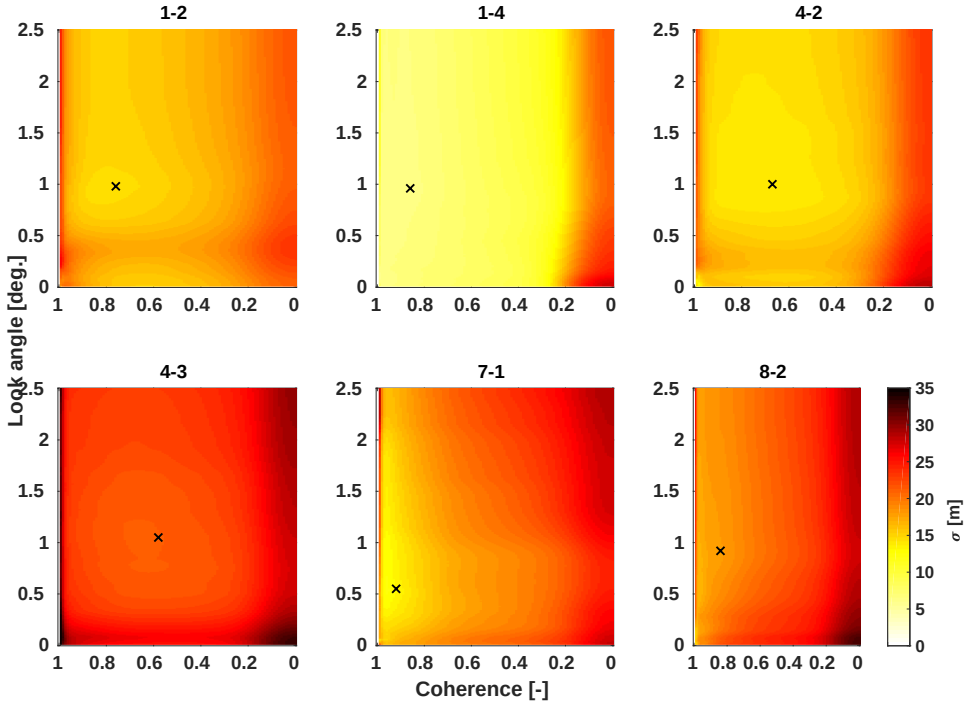

Figure A.13: Impact of variation of a coherence threshold on the standard deviation for different drainage basins.

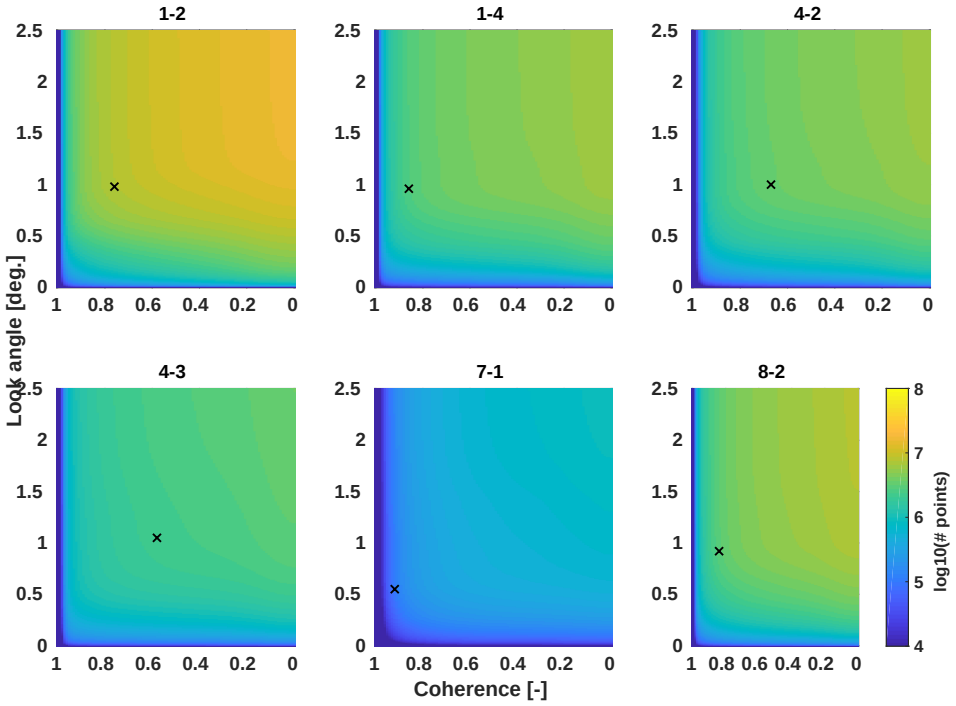

Figure A.14: Impact of variation of a coherence threshold on the number of available points for different drainage basins.

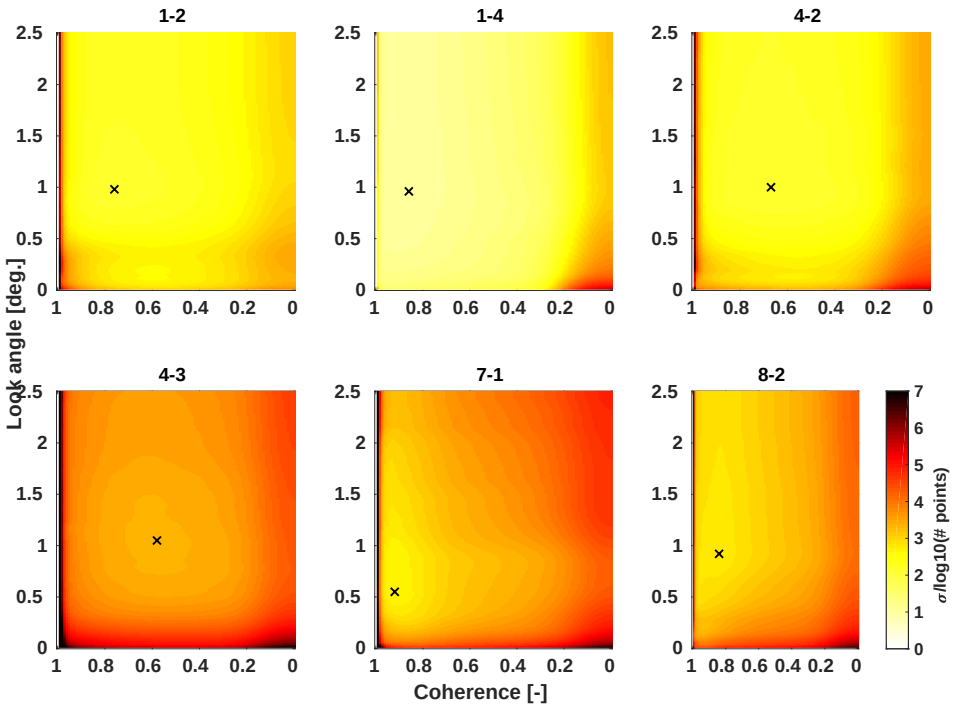

Figure A.15: Impact of variation of a coherence threshold on the optimisation criterion for different drainage basins.

R versus look angle

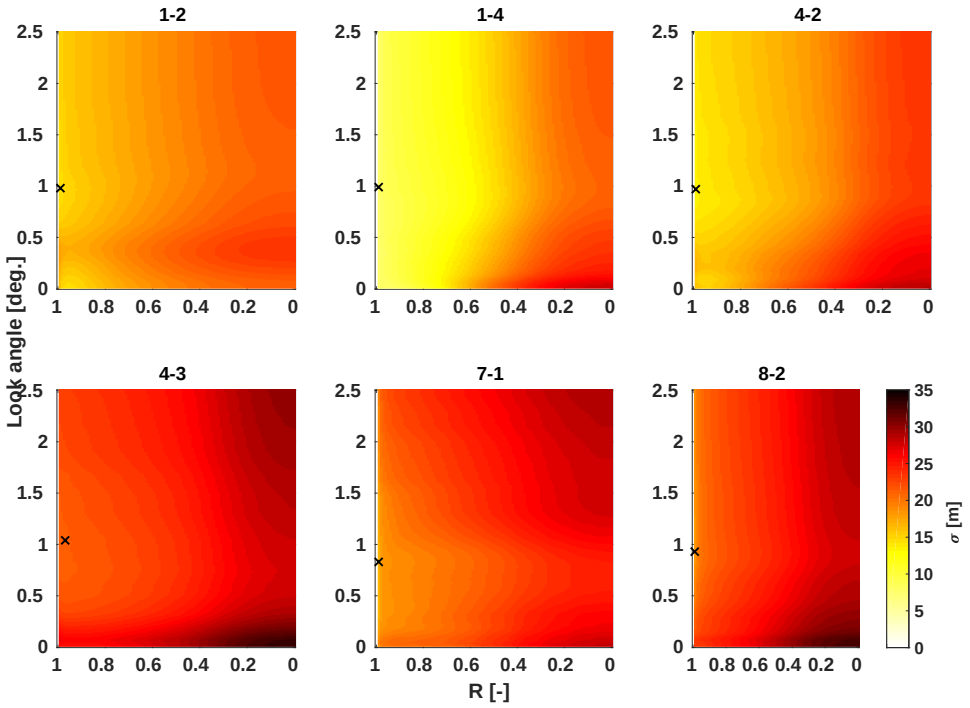

Figure A.16: Impact of variation of a PD dispersion threshold on the standard deviation for different drainage basins.

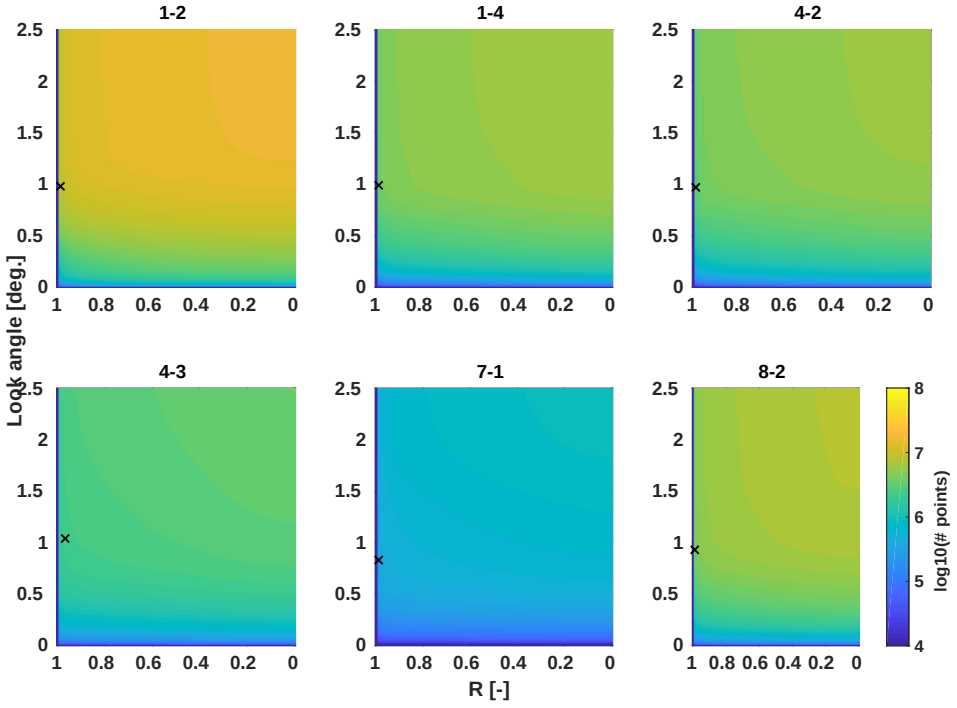

Figure A.17: Impact of variation of a PD dispersion threshold on the number of available points for different drainage basins.

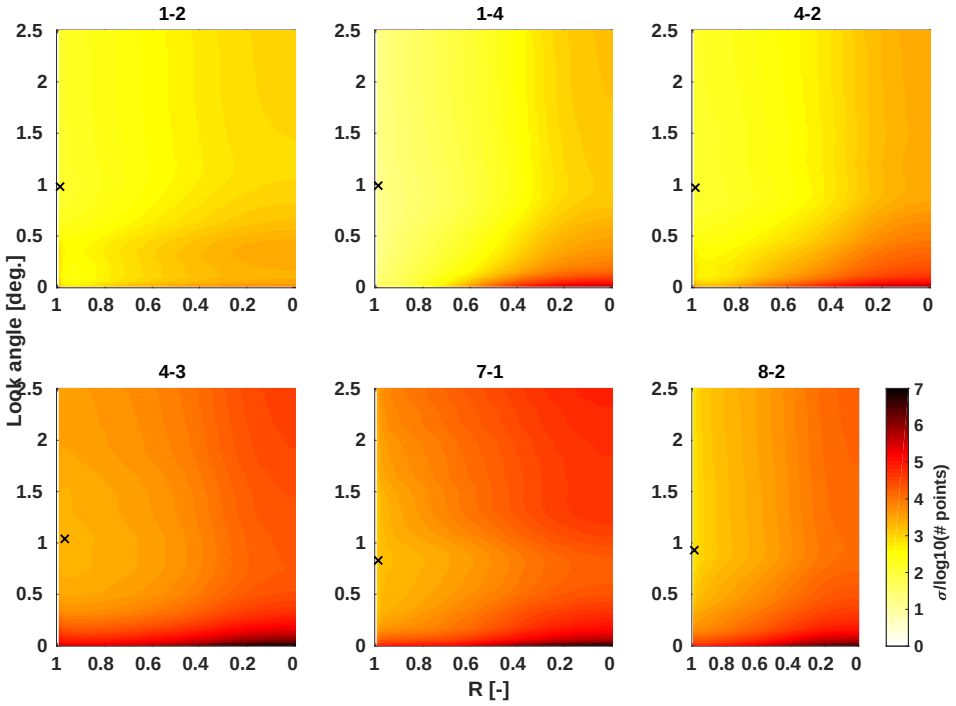

Figure A.18: Impact of variation of a PD dispersion threshold on the optimisation criterion for different drainage basins.

Horizontal flow velocity

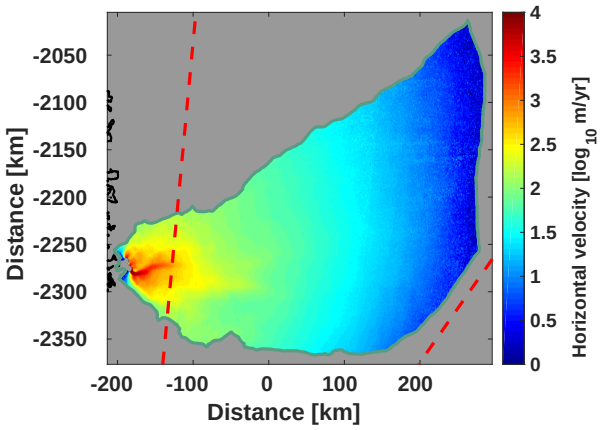

Figure A.19: Horizontal flow velocity in the Jakobshavn drainage basin. Near the terminus flow velocities reach up to several km/yr. *Greenland ice velocity map (500 m resolution) based on Sentinel-1 data (2015-10-01 to 2016-10-31) [version 1.2], [Nagler et al., 2015].*

Firn Densification Model (FDM)

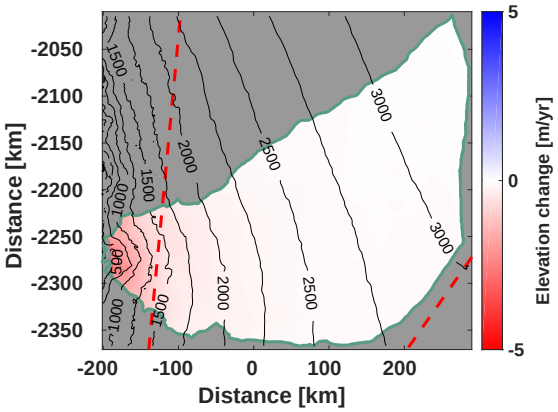

(a) Linear trend of the firn densification model. The linear trend was estimated using the functional model from equation 4.1.

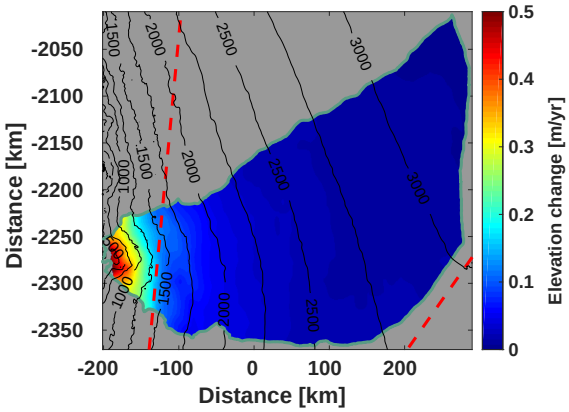

(b) Firn densification model error. The FDM error consists of the RSS of the model fit and 20% modelling error, i.e. 20% of the linear trend.

Figure A.20: FDM models the direct elevation change by precipitation of snow, melt of the snow pack as well as compaction of the snow pack. *Linear trend was derived from FDM_FGRN11 at 11 × 11 km^2 resolution. FDM_FGRN11 was made available by S. Ligtenberg of the University of Utrecht (IMAU).*

Ice mask

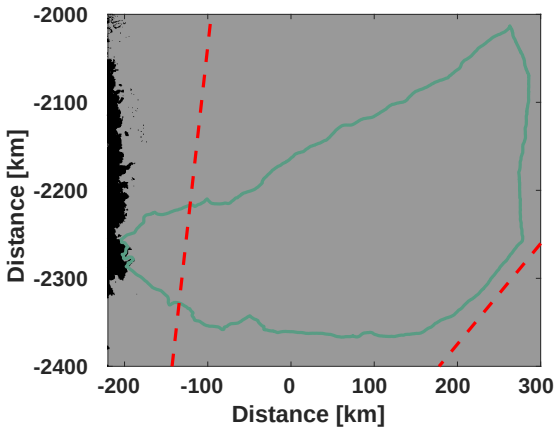

Figure A.21: Ice mask of the Jakobshavn drainage basin (90 m resolution). The black area indicates non-glacier terrain. The mask is based on LandSat and RADARSAT imagery from 1999 until 2001. *Ice mask taken from Howat [2017]. Mode boundaries taken from ESA. Jakobshavn drainage basin boundary taken from Zwally et al. [2012].*